

NERC Scientific Facilities and Technology Ion Microprobe Facility



**University of Edinburgh
NERC Ion Microprobe Facility**

Annual Science Report

Ion Microprobe Facility
School of Geosciences
Kings Buildings
West Mains Road
Edinburgh
EH9 3JW

<http://www.geos.ed.ac.uk/facilities/>

Contents

Ion Microprobe Projects

| No | Authors | Project Title | p. |
|-----------|--|--|-----------|
| 1 | N. Allison, A.A. Finch | Controls on Sr/Ca in scleractinian corals: the effects of Ca-ATPase and transcellular Ca channels on skeletal chemistry | 1 |
| 2 | N. Allison, A.A. Finch | The role of DIC in buffering coral skeletal $\delta^{11}\text{B}$: a high resolution $\delta^{13}\text{C}$ record in a <i>Porites lobata</i> coral | 3 |
| 3 | G.D. Bromiley, G. Pennacchioni and F. Nestola | Accurately determining the temperature of deformation in felsic mylonites: extending the Ti in quartz thermometer | 5 |
| 4 | A.P. Burnham and A.J. Berry | Zircon as a probe of the oxygen fugacity of magmas | 7 |
| 5 | B. Buse, R. S. J. Sparks and J. C. Schumacher | Origin of calcite within kimberlites: Implications for the formation of dark coherent kimberlite | 9 |
| 6 | B. Cesare, G. Cruciani and M. Silvestri | New data on the dehydrogenation of Ti-rich biotite | 11 |
| 7 | M. Edmonds, D. Neave, M. Plail, M. Humphreys, J. Barclay, R. Herd | Volatiles in volcanic systems undergoing mafic recharge | 13 |
| 8 | L. Field and J. Blundy | The magmatic evolution of Dabbahu Volcano, Afar Rift, Ethiopia | 15 |
| 9 | L.C. Foster, R. W. Hinton, D. N. Schmidt, C. Coath, A. Ridgwell | Past records of ocean acidification - the Palaeogene hyperthermals | 17 |
| 10 | N.N. Hanson, C.M. Wurster and C.D. Todd | $\delta^{18}\text{O}$ & $\delta^{13}\text{C}$ profiles of Atlantic salmon otoliths | 19 |
| 11 | S.L. Harley and V. Nandakumar | Timescales of melting in hot orogens: 'inside-out' zircons from the Kerala Khondalite Belt, India | 21 |
| 12 | M.E. Hartley, T. Thordarson and J.G. Fitton | Geochemical variation in the melt source region beneath the Askja volcanic system, North Iceland | 23 |
| 13 | J. Harvey, I.J. Parkinson, M.A. Fehr, R.H. James, P.A. Bland, M.A. Sephton | Geospeedometry of lithium isotopes in chondrites | 25 |
| 14 | A. Kaye and T. Thordarson | U-Pb dating of the felsic footwall succession to the Cosmos nickel-sulfide deposits, Agnew-Wiluna greenstone belt, Yilgarn Craton, Western Australia | 27 |
| 15 | P.J. Lancaster, C.D. Storey and C.J. Hawkesworth | Archaean to Early Proterozoic crust generation in north-west Scotland | 29 |
| 16 | P. Lesne, J. Blundy, F. Witham, S.C. Kohn | Understanding the mechanisms of gas loss at persistently degassing basaltic volcanoes | 31 |

| | | | |
|----|---|--|----|
| 17 | A. Lewis, C. Trueman and E. Hunter | Disentangling environmental and physiological influences on otolith growth: unlocking the potential use of otoliths as natural tags | 33 |
| 18 | J.M. MacDonald, J. Wheeler, S.L. Harley, Q.C. Crowley, K.M. Goodenough and E. Mariani | The effects of metamorphic overprinting on zircon | 35 |
| 19 | N. Matthews, D.M Pyle and C.J.N. Wilson | Origins of large volume ignimbrites from the Taupo Volcanic Zone, New Zealand | 37 |
| 20 | A. Miles, C. Graham, M. Gillespie, C. Hawkesworth and R. Hinton | The preservation of magmatic processes in the isotopic and trace element stratigraphy of zircon and apatite | 39 |
| 21 | R. Mitchell | Oxygen isotope studies of serpentine in kimberlite | 41 |
| 22 | R. Mitchell | Trace element and Li isotope geochemistry of nyerereite and gregoryite phenocrysts from natrocarbonatite lava, Oldoinyo Lengai, Tanzania | 43 |
| 23 | M. Piochi, R. Moretti, G. De Astis and A. Mormone, | In-situ isotope and volatile measurements of melt inclusions hosted in olivines from Phlegraean and Stromboli volcanoes, Southern Italy | 45 |
| 24 | J. Riker, J. Blundy, A. Rust and O. Melnik | The influence of CO ₂ on phase relations and crystallisation kinetics in silicic magmas: a case study at Mount St. Helens | 47 |
| 25 | A. Sadekov, K. Darling, Dick Kroon, R. Ganeshram, U. Fallet, G.-J. Brummer | Towards developing a proxy for ocean seasonality: Step 1. Characterisation of natural variability in geochemical signals of planktonic foraminiferal populations | 49 |
| 26 | C. Sarkar, C. D. Storey and C. J. Hawkesworth | Petrogenesis of kimberlite: mantle sources and shallow level contamination | 51 |
| 27 | I. Sides, M. Edmonds and J. Maclennan | The Role of volatiles during historical eruptions from Kilauea Volcano, Hawai'i: Constraints on source to surface processes using melt inclusions | 53 |
| 28 | S. Skora and J. Blundy | Monazite saturation in silicate melts at high pressure with implications for subduction zone volcanism | 55 |
| 29 | M. Thomas and S.L. Harley | Long-lived deep-crustal metamorphism in the Eastern Ghats Belt, India | 57 |
| 30 | T. Thordarson, M.E. Hartley, C. Hayward and J.G. Fitton | Major, trace and volatile chemistry of the March to May 2010 basaltic flank and benmorite summit eruptions at Eyjafjöll volcano, Iceland | 59 |
| 31 | B. Winpenny and J. Maclennan | Oxygen isotope variation in Icelandic basalts: disentangling mantle and crustal signatures | 61 |

Controls on Sr/Ca in scleractinian corals: the effects of Ca-ATPase and transcellular Ca channels on skeletal chemistry

N. Allison, A.A. Finch

Department of Earth Sciences, University of St. Andrews, St. Andrews KY16 9AL, UK

Introduction

The Sr/Ca of aragonitic coral skeletons is a commonly used palaeothermometer. However skeletal Sr/Ca is typically dominated by weekly-monthly oscillations which do not reflect temperature or seawater composition and the origins of which are currently unknown. The skeleton is considered to precipitate from an extracellular calcifying fluid (ECF) enclosed in a semi-isolated space between the skeleton and the overlying coral tissue. Unmodified seawater is transported directly to the ECF [1] and Ca^{2+} is also transported across the coral tissues by both Ca-ATPase [2] and L-type Ca channels [3]. Sr^{2+} has a similar ionic radius to Ca^{2+} , and Sr^{2+} may be able to substitute for Ca^{2+} in transcellular transport mechanisms [4], although such mechanisms may have a higher affinity for Ca^{2+} than Sr^{2+} [5]. Variations in the relative contributions of each of the transport mechanisms to the ECF and the efficiencies with which each process transports Sr^{2+} and Ca^{2+} could explain the Sr/Ca heterogeneity observed in coral skeletons.

Methods

To test the impact of transcellular Ca^{2+} transport processes on skeletal Sr/Ca, colonies of the branching coral, *Pocillopora damicornis*, were cultured in the presence of inhibitors of Ca-ATPase (ruthenium red) and Ca channels (verapamil hydrochloride). Inhibitors were dissolved in dimethyl sulfoxide solution (DMSO) to a final concentration of 0.1%. In all, corals were cultured in 2 concentrations of ruthenium red, 3 concentrations of verapamil and in DMSO and seawater controls. Each treatment was tested in duplicate. A stable isotope tracer (^{42}Ca , added as $^{42}\text{CaCO}_3$), readily resolved by SIMS analysis, was added to the culture seawater at the same time as the inhibitors or solvent (if used), allowing accurate identification of the skeleton deposited in the presence of the inhibitors. The photosynthesis, respiration and calcification rates of the colonies were monitored throughout the experiment. The skeleton deposited in the presence of the inhibitors was identified (by ^{42}Ca spike) and analysed for Sr/Ca by SIMS. Analyses which did not exhibit enhanced $^{42}\text{Ca}/^{44}\text{Ca}$ throughout the analysis were rejected. 5-25 SIMS analyses were made per colony, typically sampling 4-5 corallites. Sections were repolished between batches of analyses to expose fresh areas for SIMS.

Results and Discussion

The skeleton deposited in the seawater control (no DMSO) had significantly lower skeletal Sr/Ca (Fig. 1) than all the other treatments with the exception of the DMSO control (ANOVA, $p=0.05$). The Sr/Ca of the aragonite deposited in the presence of either of the inhibitors was not significantly different from that of the solvent (DMSO) control, although the coral calcification rate was reduced by up to 66% and 73% in the ruthenium red and verapamil treatments respectively. Either Ca-ATPase and Ca channels transport Sr^{2+} and Ca^{2+} in virtually the same ratio in which they are present in seawater or transcellular processes contribute little Ca^{2+} to the skeleton and most Ca is derived from seawater transported directly to the calcification site. Variations in the activities of Ca-ATPase and Ca-channels are not responsible for the weekly-monthly Sr/Ca oscillations observed in paleoenvironmental chronologies, assuming that the specificities of Ca transcellular transport processes are similar between coral genera.

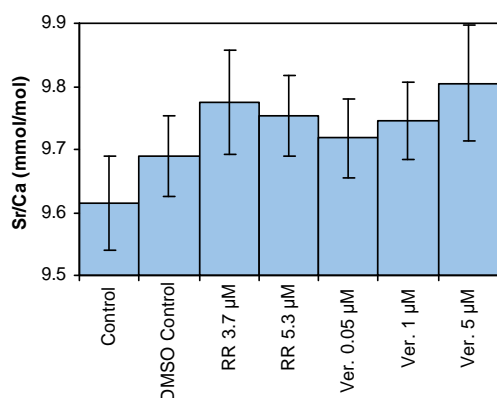


Figure 1. Mean Sr/Ca of coral aragonite deposited in each treatment. Error bars indicate 95% confidence limits ($2\sigma/\sqrt{n}$). RR = ruthenium red. Ver. = verapamil.

References: [1] J. Erez & A. Braun (2007) *Geochim. Cosmochim. Acta* 71, SA260 [2] Y.K. Ip et al. (1991) *Mar. Biol.* 111, 191-197 [3] D. Zoccola et al. (1999) *Gene* 227, 157-167 [4] Y.K. Ip & A.L.L. Lim, (1991) *J. Exp. Biol.* 159, 507-513 [5] X. Yu & G. Inesi (1995) *J. Biol. Chem.* 270, 4361-4367. [6] N. Allison et al. (2007) *Geochim. Cosmochim. Acta* 71, 4693-4703

The role of DIC in buffering coral skeletal $\delta^{11}\text{B}$: a high resolution $\delta^{13}\text{C}$ record in a *Porites lobata* coral

N. Allison, A.A. Finch

Department of Earth Sciences, University of St. Andrews, St. Andrews KY16 9AL, UK

Background information

The geochemistry of tropical coral skeletons is encoded by local seawater conditions at the time of deposition and the analysis of fossil corals provides a route to reconstruct past climates. In particular coral Sr/Ca is a commonly used palaeothermometer and has been used to estimate past sea surface temperatures (SSTs) while $\delta^{11}\text{B}$ may reflect past seawater pH. However SIMS studies demonstrate that coral skeletons are more geochemically heterogeneous with respect to Sr/Ca, B/Ca and $\delta^{11}\text{B}$ than expected from SST and water chemistry, indicating the importance of other, non climatic factors on skeletal geochemistry [e.g. 1]. During previous work [1] we have not observed a simple correlation between skeletal Sr/Ca and $\delta^{11}\text{B}$ /calcification site pH to support the hypothesis that Sr/Ca directly reflects Ca-ATPase activity i.e. the enzyme pumps Ca (but not Sr) into the calcification site and the Sr/Ca of the extracellular calcification fluid (ECF) is diluted during periods of high Ca-ATPase activity. To explore how skeletal Sr/Ca and calcification site pH may vary as observed we developed a model of the predicted Sr/Ca composition of the ECF and the aragonite precipitated from it, over a range of Ca-ATPase activities and DIC concentrations (Figure 1). The DIC concentration in the ECF will vary depending on the [DIC] in the overlying coral tissue, reflecting the balance of respiration and photosynthesis in the coral animal and the associated symbiotic algae. Photosynthesis and calcification compete for DIC in *Porites* corals [2]. We therefore hypothesise that pH changes in the calcification fluid, driven by Ca-ATPase activity, can be buffered by varying DIC concentrations in the calcification fluid.

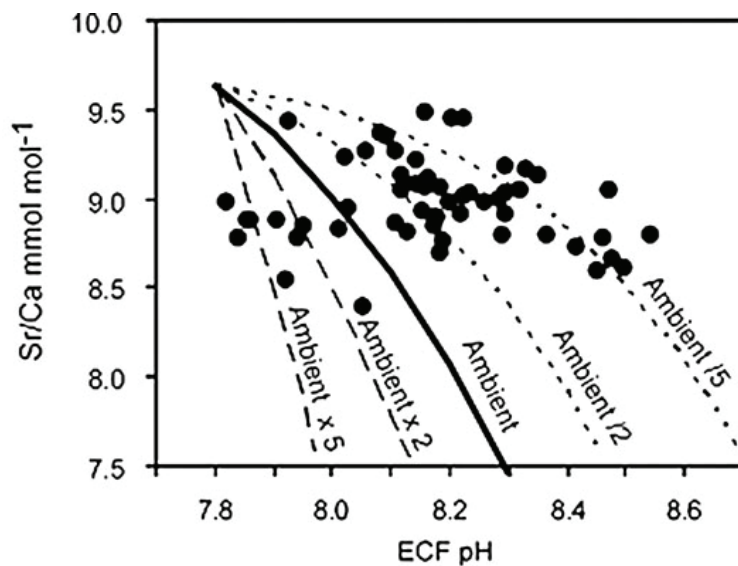


Figure 1. Modelled Sr/Ca (lines) of the coral aragonite as a function of ECF pH under a range of DIC concentrations. We assumed that the ECF is derived from seawater modified by Ca-ATPase which pumps one Ca^{2+} into the ECF for each 2H^+ ions pumped out. We assume that Sr^{2+} is not transported by the enzyme. The accompanying increase in pH of the ECF shifts the CO_2 system equilibrium in the favour of $\text{CO}_2 \rightarrow \text{HCO}_3^- \rightarrow \text{CO}_3^{2-}$. We have modelled the composition of the ECF under 5 carbonate regimes by assuming that the $[\text{CO}_2]$ of the fluid is in equilibrium with seawater (ambient) or is up to 5 times more or less than this value. Higher DIC values might reflect a high respiration/photosynthesis ratio and low

DIC the opposite. Observed SIMS data (•) are overlain on the graph.

This project was implemented to investigate the relationship between skeletal trace element, $\delta^{11}\text{B}$ (as an indicator of calcification site pH) and $\delta^{13}\text{C}$ (as an indicator of carbon source and concentration at the calcification site). Skeletal carbon is derived from both seawater DIC and from metabolic CO_2 which can readily diffuse across biological membranes to the calcification site. Metabolic CO_2 is substantially depleted in $\delta^{13}\text{C}$ compared to seawater $\delta^{13}\text{C}$ and variations in skeletal $\delta^{13}\text{C}$ reflect variations in the proportions of the two sources of carbon used in calcification [3]. Seawater diffuses passively to the calcification site and its input rate is likely to be constant. The input of metabolic CO_2 to the calcification site will vary to reflect $[\text{CO}_2]$ in the overlying coral tissue. Metabolic CO_2 input to the ECF is high when coral and zooxanthellae respiration rates are high and substantially exceed the photosynthetic rate of the zooxanthellae, resulting in high tissue CO_2 . In this case the [DIC] in the ECF

will increase and will become relatively depleted in ^{13}C . Metabolic CO_2 input to the ECF is low when tissue $[\text{CO}_2]$ is low e.g. when photosynthesis exceeds respiration. In this case a higher proportion of ECF DIC will be derived from seawater (rather than metabolic CO_2) and the ^{13}C of the ECF will be relatively enriched. If our hypothesis is correct then skeletal $\delta^{13}\text{C}$ variations will match the pattern predicted from our $\delta^{11}\text{B}$ and Sr/Ca data (Figure 2A).

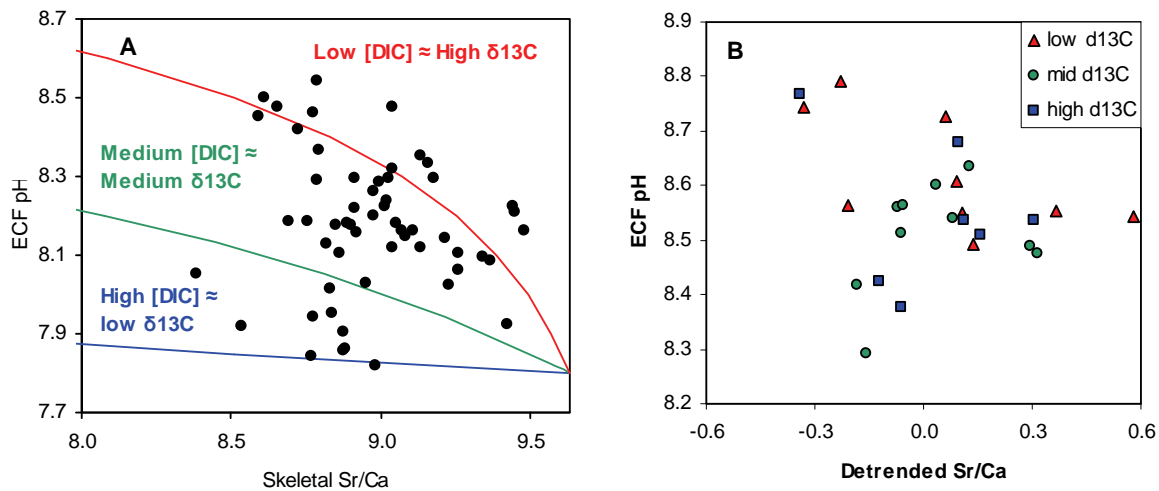


Figure 2. **A:** Modeled skeletal Sr/Ca as a function of ECF pH under a range of DIC scenarios. Green line shows $[\text{CO}_2]$ in the overlying coral tissue is ambient i.e. maintains equilibrium with atmospheric CO_2 levels. At low DIC tissue $[\text{CO}_2]$ is ambient/5 and at high DIC tissue $[\text{CO}_2]$ is ambient x5. Black dots represent observed SIMS data. **B:** Observed detrended skeletal Sr/Ca and ECF pH (estimated from skeletal $\delta^{11}\text{B}$), divided into groups of low, mid and high $\delta^{13}\text{C}$ values. $\delta^{13}\text{C}$ is detrended to remove the seasonal signal which may reflect seasonal variations in $\delta^{13}\text{C}$ of seawater or in the $\delta^{13}\text{C}$ of metabolic CO_2 (4).

Results and Discussion

To test this hypothesis we analysed $\delta^{13}\text{C}$ at key locations in the *Porites lobata* coral record, previously analysed for Sr/Ca and $\delta^{11}\text{B}$. We correlated skeletal $\delta^{13}\text{C}$ with both $\delta^{11}\text{B}$ and Sr/Ca using our model of ECF and carbonate composition (Figure 2B). We corrected (detrended) the coral Sr/Ca record for seasonal seawater temperature effects on Sr incorporation. We do not observe the predicted pattern in skeletal $\delta^{13}\text{C}$ to support the tested hypothesis i.e. skeletal Sr/Ca variations cannot be explained by variations in Ca-ATPase activity, which can be inferred from a combination of skeletal $\delta^{11}\text{B}$ and $\delta^{13}\text{C}$. Our other SIMS work (see report on “Controls on Sr/Ca in scleractinian corals: the effects of Ca-ATPase and transcellular Ca channels on skeletal chemistry”) suggests that either Ca-ATPase and Ca channels transport Sr^{2+} and Ca^{2+} in virtually the same ratio in which they are present in seawater or transcellular processes contribute little Ca^{2+} to the skeleton and most Ca is derived from seawater transported directly to the calcification site. Both these SIMS studies suggest that variations in the activity of Ca-ATPase are not the principal controls on skeletal Sr/Ca. The origin of the short temporal resolution skeletal Sr/Ca heterogeneity typically observed in coral skeletons remains to be resolved.

References

- [1] N. Allison et al. (2010) *Geochimica Cosmochimica Acta* **74**, 1790-1800
- [2] L. Herfort et al. (2008) *Journal of Phycology* **44**, 91-98
- [3] C. Rollion et al. (2003) *Coral Reefs* **22**, 405-415
- [4] P.K. Swart et al. (2005) *Geochimica Cosmochimica Acta* **69**, 1495-1509

Accurately determining the temperature of deformation in felsic mylonites: extending the Ti in quartz thermometer

G.D. Bromiley¹, G. Pennacchioni² & F. Nestola²

¹School of GeoSciences, University of Edinburgh, Edinburgh EH9 3JW, UK

²Dipartimento di Geoscienze, University of Padova, Italy

Introduction.

Ti in quartz thermometry (TiQ) allows accurate and precise determination of quartz crystallisation temperatures [1]. In this study we analysed TiQ contents in deformed monomineralic quartz veins in the Adamello tonalite (Southern Alps, Italy) to provide the first accurate determination of deformation temperatures during dynamic recrystallisation of felsic rocks. These rocks were deformed and recrystallised at low temperatures, necessitating use of SIMS in order to accurately determine Ti contents in quartz. Ti contents in vein quartz were determined by SIMS using the Cameca IMS 4f instrument at the Edinburgh IMF with a 5 nA beam. The spot size was approximately 20x25 μm , significantly smaller than the quartz grain size in all samples. Ti contents were calculated from ^{48}Ca -corrected $^{48}\text{Ti}/^{30}\text{Si}$ and $^{49}\text{Ti}/^{30}\text{Si}$ signal ratios and known SiO_2 contents of the samples and standard (NIST SRM610 glass).

Dynamic recrystallisation of quartz veins.

TiQ temperatures were determined from 2 types of veins: weakly deformed veins (WDV) and strongly deformed veins (SDV), both of which had previously been characterised by computer-integrated polarization microscopy (CIP) and X-ray texture goniometry. Analysis indicates that veins in the Adamello tonalite were opened and deformed at shear strains up to $\gamma > 15$ over a very small temperature window (~ 25 C) at ~ 500 C. Veins played a critical role in localising homogenous simple shear during postmagmatic cooling of the body. Analysis of quartz deformation in these veins provides a useful assessment of the applicability of deformation experiments in modelling the rheology of the lithosphere at low temperatures and most importantly, over longer durations and at much higher strains than can easily be achieved in the laboratory. Slip systems in vein quartz during plastic deformation were dominantly prism $\langle a \rangle$ and subordinate rhomb and basal $\langle a \rangle$. Dynamic recrystallisation occurred rather abruptly at $3 < \gamma < 4$.

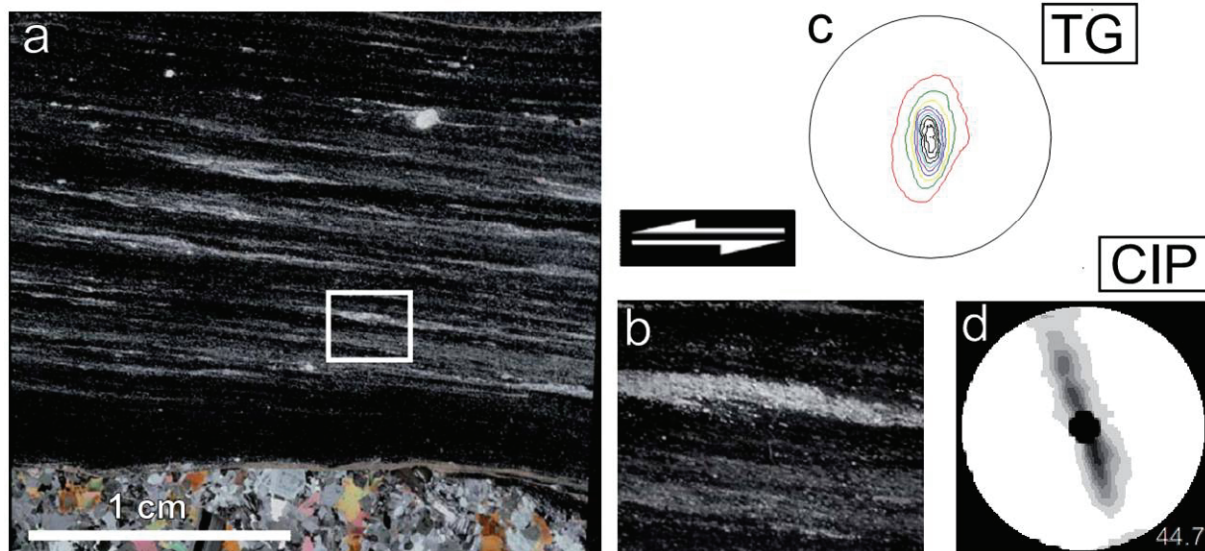


Figure 1. Local scale fabric heterogeneity in a strongly deformed vein (SDV). a) optical micrograph of a thin section under crossed polars with the area investigated by CIP outlined (enlarged view shown in b) where the extinction banding delineating foliation is clearly visible. The bulk CPO is shown in c (relative to an area of about 1 cm^2), and is dominated by c-axes close to the Y direction, which is typical of SDV in the samples studied. d) shows CPO measured by CIP for the area shown in (b). Mean recrystallisation temperature measured by SIMS and the TiQ method in this sample is 525 ± 7 C.

In contrast to creep experiments in quartz (and other minerals) a steady-state recrystallised fabric was then achieved during the early stages of deformation ($\gamma \sim 4$). There is no evidence, with increasing strain, of strengthening of crystal preferred orientation (CPO), or rotation of the fabric skeleton or of variation of grain size.

The observed relationship between the initial growth CPO and the kinematic framework suggests that the veins opened at a temperature close to that at which there is a switch between the activity of prism $\langle c \rangle$ and prism $\langle a \rangle$ slip in quartz, with the temperature of growth causing growth of crystals well oriented for slip. Differences between WDV and SDV can be explained in terms of the initial orientation of quartz crystals, with WDV representing the relicts of veins with an initial CPO developed during crystal growth which was unsuitably oriented for prism $\langle a \rangle$ slip during the subsequent shear. As such, this work demonstrates that initial CPO of veins from which quartz mylonites are commonly derived plays a critical role in fabric evolution. The strong growth- and strain-induced CPO of sheared veins inhibits significant reworking during lower temperature stages of pluton cooling when basal $\langle a \rangle$ slip is dominant. Work also demonstrates the applicability of the TiQ thermometer in accurately assessing recrystallisation temperatures at much lower temperatures than previously applied (the thermometer was calibrated [1] for a relatively high temperature range of 600-1000 C). Thus, the technique can be applied to provide information on the efficiency of shear heating during plastic deformation and post-magmatic deformation at natural strain strains, providing critical information required to understand key geological processes such as the rheological evolution of Earth's lithosphere. Results from this investigation were published in Pennachioni et al. (2010) [2].

References

- [1] D.A. Wark and E.B. Watson (2006) *Contributions to Mineralogy and Petrology* **152**, 743-754
- [2] G. Pennachioni, L. Menegon, B. Leiss, F. Nestola and G.D. Bromiley (2010) *Journal of Geophysical Research –Solid Earth* **115**, B12405

Zircon as a probe of the oxygen fugacity of magmas

A.P. Burnham & A.J. Berry

Department of Earth Science and Engineering, Imperial College London, South Kensington SW7 2AZ, UK

Introduction

Zircon is arguably the most important mineral in geology due to its use in radiometric dating and its preservation of trace element signatures that record geological processes. One such signature is defined by the rare-earth elements (REE). Anomalous abundances of Ce and Eu, usually both, are a feature of all igneous zircon. These anomalies are almost certainly related to the presence of oxidation states other than the trivalent, in which form the other REE occur exclusively. The presence of a positive Ce anomaly (Ce^{4+}) suggests an oxidised magma (substitution of Ce^{4+} for Zr^{4+}) while a coexisting negative Eu anomaly (Eu^{2+}) indicates reduced conditions (either Eu^{2+} in the melt from which the zircon crystallised or depletion of Eu due to the incorporation of Eu^{2+} into earlier crystallising plagioclase). This suggests a new potential role for zircon as a recorder of the oxygen fugacity ($f\text{O}_2$) of a melt, allowing insight into ancient magmas (such as those in the Hadean) that have long since eroded away.

A limitation in our ability to interpret the geochemical significance of these anomalies is the difficulty of growing experimental zircons from melts of sufficient size for trace element analyses. This has prevented the determination of zircon-melt partition coefficients as a function of $f\text{O}_2$. We have been successful in growing large (up to 100s of microns) zircon crystals from Zr-rich “natural” melts in a one-atmosphere gas mixing furnace where the $f\text{O}_2$ can be accurately controlled and continuously varied. Zircon-glass pairs were prepared over 14 log units in $f\text{O}_2$, corresponding to QFM-8 to QFM+6 (where QFM is the quartz-fayalite-magnetite buffer). The melts were doped with all the REE plus Sc, Ti, Th and U. A typical sample is shown in Figure 1.



Fig. 1. Cathodoluminescence image of synthetic zircon crystals in silicate glass, typical of the samples analysed in this study. The field of view is 500 μm .

Results

The concentration of trace elements in the zircon and glass of each sample was determined using the Cameca ims-4f ion probe. The resulting average zircon-melt partition coefficients for the REE are shown in Figure 2. The magnitude of the Ce and Eu anomalies varies systematically with $f\text{O}_2$. The anomalies coexist between QFM and QFM-3 although are smaller than seen in many natural samples. The coexistence indicates that there is a $f\text{O}_2$ window in natural systems where zircon will crystallise with both Ce and Eu anomalies. The decreased magnitudes of the anomalies compared to natural samples suggest that temperature or melt composition (in particular the effect of K, Na, and H) may have a significant effect on either the partition coefficients or the $f\text{O}_2$ dependence of $\text{Ce}^{3+}/\text{Ce}^{4+}$ relative to $\text{Eu}^{2+}/\text{Eu}^{3+}$ (i.e. the curve defining $\text{Ce}^{3+}/\text{Ce}^{4+}$ may shift to lower $f\text{O}_2$ s and that for $\text{Eu}^{2+}/\text{Eu}^{3+}$ to higher $f\text{O}_2$ s). Alternatively, changes in the relative abundance of the Eu and Ce relative to the other REE due to partitioning into earlier crystallising phases may be important in natural systems.

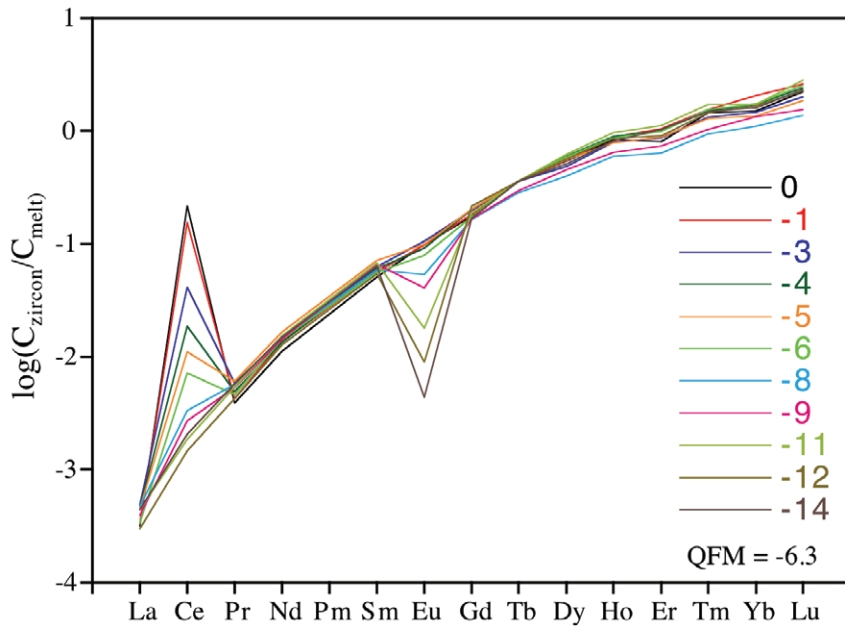


Figure 2: Average REE zircon-melt partition coefficients as a function of oxygen fugacity. The REE patterns have been referenced to Tb to aid comparison.

In related work we are attempting to quantify $\text{Eu}^{2+}/\text{Eu}^{3+}$ and $\text{Ce}^{3+}/\text{Ce}^{4+}$ in silicate melts as a function of $f\text{O}_2$ using X-ray absorption near edge structure (XANES) spectroscopy. The spectra (Figure 3) exhibit systematic changes that correspond to changes in $\text{Ce}^{3+}/\text{Ce}^{4+}$ and $\text{Eu}^{2+}/\text{Eu}^{3+}$ and we expect to quantify $\text{Ce}^{3+}/\Sigma\text{Ce}$ and $\text{Eu}^{2+}/\Sigma\text{Eu}$ to better than 2% absolute.

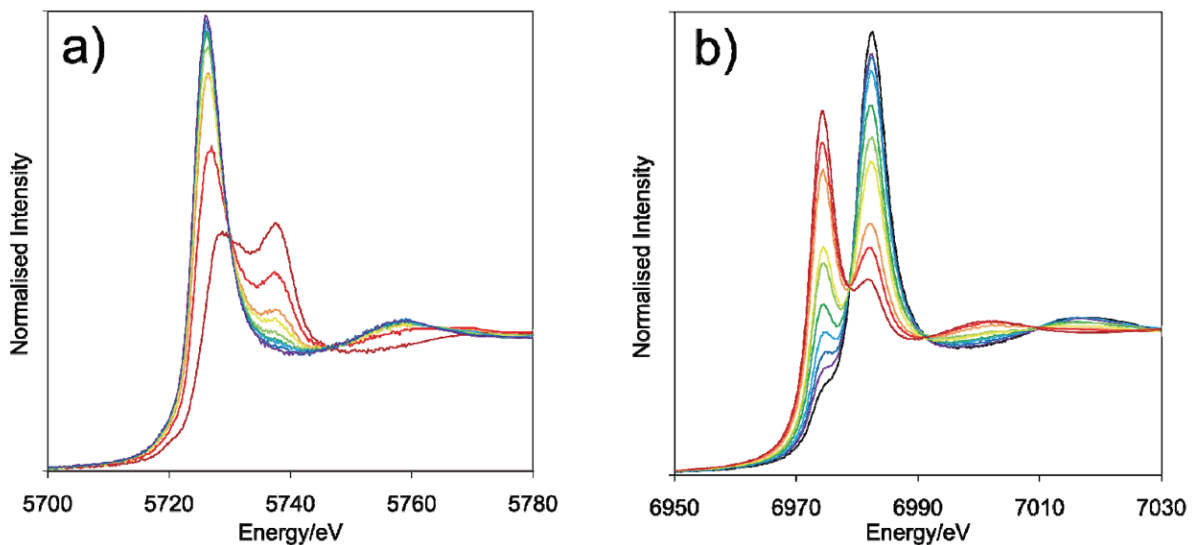


Figure 3: a) Ce and b) Eu XANES spectra of silicate glasses that were equilibrated as melts over a range of $f\text{O}_2$ s.

The zircon-melt partitioning of U and Th was also determined and $D_{\text{U}}/D_{\text{Th}}$ was found to decrease smoothly with increasing $f\text{O}_2$. Th occurs exclusively as Th^{4+} whereas U can occur as U^{4+} , U^{5+} , and U^{6+} . The $f\text{O}_2$ range over which $D_{\text{U}}/D_{\text{Th}}$ changes suggests that all three oxidation states of U occur in silicate melts under geological conditions. This unexpected result is consistent with our recent U XANES and U/Th clinopyroxene-melt partitioning experiments.

Origin of calcite within kimberlites: Implications for the formation of dark coherent kimberlite

B. Buse¹, R. S. J. Sparks¹ & J. C. Schumacher¹

¹School of Earth Sciences, University of Bristol, Bristol BS8 1RJ, UK

Introduction

The origin of calcite within kimberlites is widely disputed and has important implications for understanding the formation of the host kimberlite. This project focuses on coherent kimberlites, which have a controversial origin; they have been interpreted as intrusions and as welded pyroclastic rocks [1, 2, 3]. The calcite occurs as interstitial phase (Fig. 1) with possible origins including crystallization from melts, vapour-phase crystallization from volcanic gases, hydrothermal metamorphism during cooling of the deposits and low temperature diagenesis or weathering post-cooling. In distinguishing between these possible origins this project will provide important evidence to resolve the debate surrounding coherent kimberlite. To discriminate between the possible origins we have analysed the REE content of calcite from coherent kimberlite of the BK9 kimberlite, Botswana and reference materials including unequivocal igneous calcite from the Venetia kimberlite dykes and the Benfontein sills and secondary calcite from late stage veins within basalt breccias, contained within the BK9 pipe, and amygdales from the surrounding Karoo basalt.

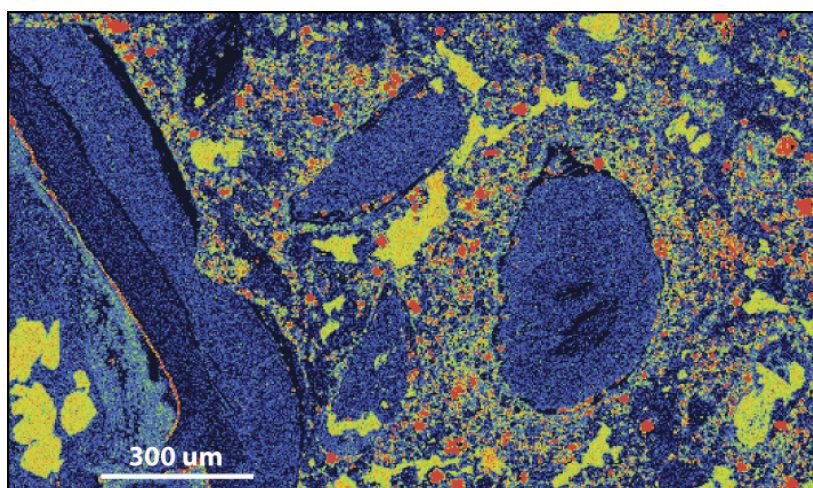


Figure 1. Interstitial calcite within coherent kimberlite. Dark blue grains are olivine clasts surrounding by kimberlite groundmass (red grains are oxide minerals); the yellow patches are the interstitial calcite.

Results

The resulting REE patterns from this analysis are given in Figure 2. The unequivocal igneous calcite from the Venetia kimberlite dykes and the Benfontein sills give steeply sloping REE patterns (Fig. 2a) as are expected for igneous calcite. The secondary calcite reference materials are distinguished from the igneous calcite by flatter REE patterns either across the entire range of REE, where the fluid precipitating the calcite is poor in REE (e.g. amygdales within the country rock Karoo basalt; Fig. 2b), or flatten for the heaviest and lightest REE, where the fluid precipitating the calcite is enriched in REE (e.g. secondary veins within the Venetia igneous dykes and the veins within the BK9 basalt breccia; Fig. 2a & c). This is consistent with the work by Bau [4] on REE mobility during metamorphism that showed that metamorphic fluids fractionate REE, with highly alkaline fluids preferentially dissolving HREE from primary calcite and precipitating secondary calcite enriched HREE. The analyses for the interstitial calcite from the BK9 coherent kimberlite give flat REE patterns (Fig. 2D) providing strong evidence that they are secondary precipitated from meteoric or groundwater fluids. This affirms the reinterpretation of many pipe filling coherent kimberlite bodies, previously considered intrusive bodies, as pyroclastic deposits in which the interstitial calcite fills primary porosity [2 & 3]. It also provides a strong case for largely hydrothermal alteration of kimberlite deposits, as oppose to deuteric alteration by late stage magmatic derived fluids, and is consistent with the other alteration phases commonly found, including serpentine, chlorite, diopside and hydrogarnet [5 & 6].

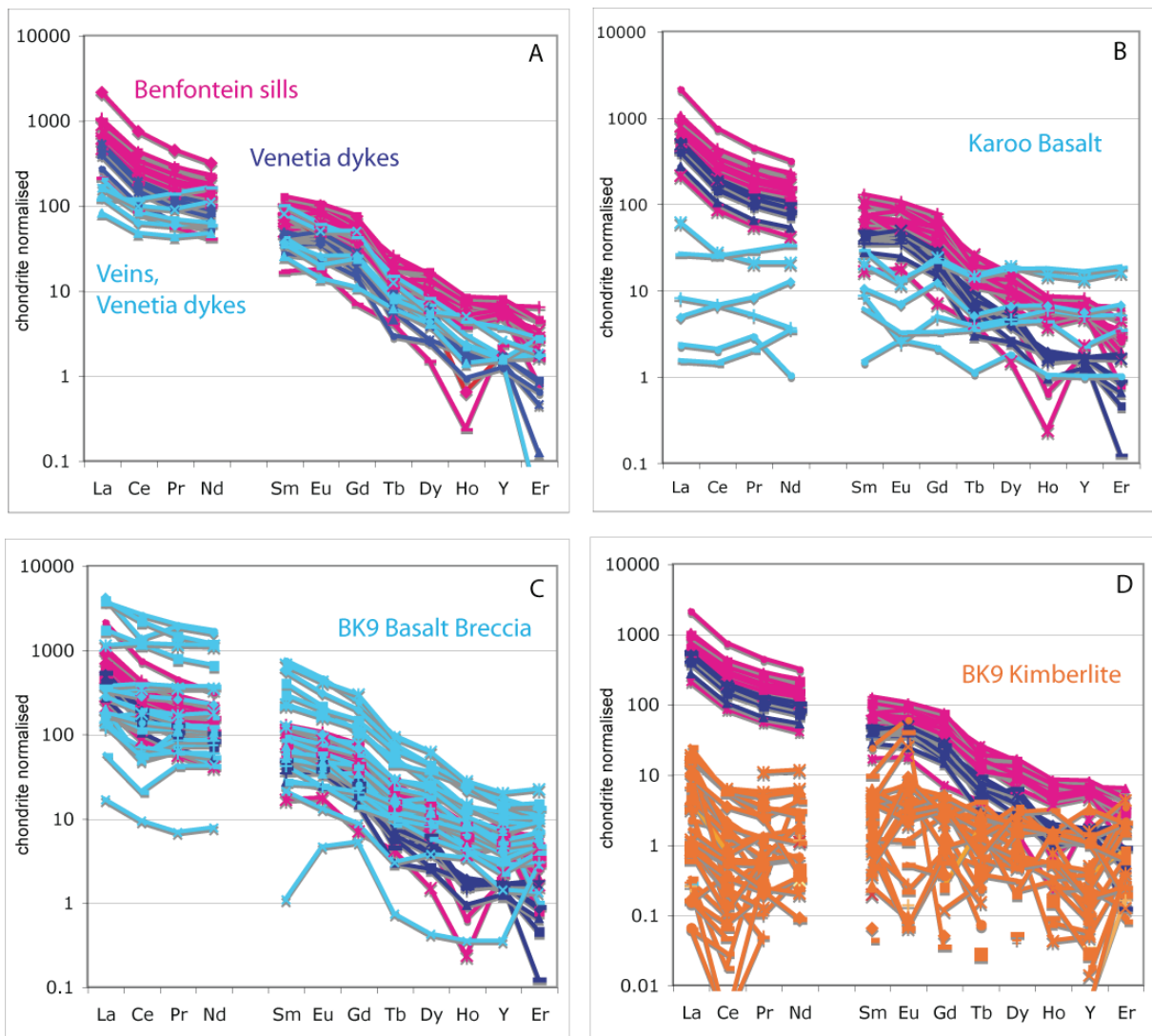


Figure 2. REE analyses acquired using SIMS. (A) Analyses of unequivocal igneous calcite from the Benfontein sills and Venetia sills as reference materials. The Venetia sills also include veins of calcite which show flatter REE patterns for the LREE and HREE. (B & C) Analyses of secondary calcite from amygdales within the country rock Karoo Basalt surrounding the BK9 kimberlite, and from veins within basalt contained within the BK9 kimberlite as reference materials. (D) Interstitial calcite from the coherent kimberlite of the BK9 kimberlite.

References

- [1] R.H. Mitchell (1986) *Kimberlites: Mineralogy, geochemistry and petrology*. Plenum Press, New York
- [2] R.S.J. Sparks et al. (2006) *Journal of Volcanology and Geothermal Research* **155**, 18-48
- [3] R.J. Brown et al. (2008) *Journal of Geology* **116**, 354-374
- [4] M. Bau (1991) *Chemical Geology* **93**, 219-230
- [5] G.R. Stripp et al. (2006) *Journal of Metamorphic Geology* **24**, 515-534
- [6] B. Buse et al. (2010) *Contributions to Mineralogy and Petrology* **160**, 533-550

New data on the dehydrogenation of Ti-rich biotite

B. Cesare¹, G. Cruciani² & M. Silvestri²

¹Department of GeoSciences, University of Padova, Italy

²Department of Earth Sciences, University of Ferrara, Italy

Introduction

The relationships between H and Ti contents in biotite are fundamental for a correct understanding and modelling of high-temperature metamorphism, anatexis and S-type granitic magmatism. In the last decade our group has worked on this topic using a multi-technique approach that includes SIMS analysis of H contents, and has brought significant advances in the crystal-chemistry of biotite from high-temperature metapelitic rocks [1, 2]. These results have allowed the refinement of the solution model of biotite to be used in thermodynamic modelling [3]. However, the H deficiency of biotite, proposed on the basis of a few case studies, is questioned in its general applicability [4]. More data are thus needed to solve this problem.

New SIMS analyses of H in biotite

Quantification of H in biotite by SIMS was performed on a Spl-Crd xenolith from El Hoyazo, in which biotite shows a wide range of Ti contents, microstructurally controlled with respect to garnet porphyroblasts and reflecting the progressive anatexis of the protolith.

33 analyses of H were obtained from microstructurally selected crystals, some of them at the lower limits of spatial resolution of the instrument, as in the sample image of Figure 1a.

The results (Figure 1b) confirm the negative correlation between Ti and H, and provide further support to the occurrence of an oxy-type exchange, expanding the data set to a wider range of TiO₂ contents, with maximum concentrations exceeding 7 wt%.

The data, utilized in a MsC thesis, will be soon submitted for publication as part of a wider paper on the dehydration-rehydration evolution of biotite during crustal anatexis.

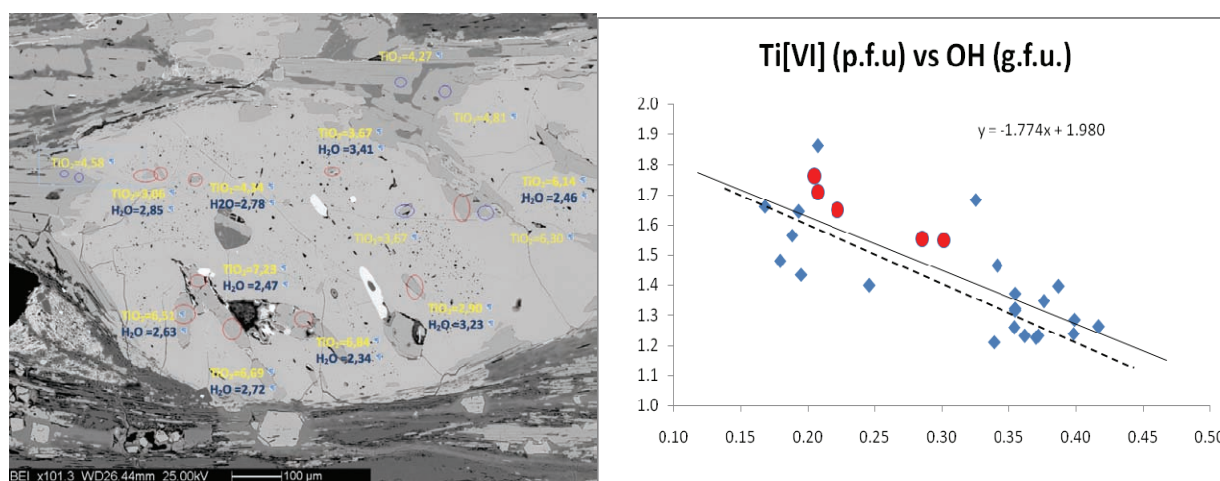


Figure 1. **a, left)** BSEM image of one of the analysed samples. Red and blue ellipses mark the biotite crystals, in variable microstructural position with respect to a porphyroblast of garnet, that have been analysed by electron microprobe (EMP). Blue (H₂O calculated from H concentrations) and yellow (TiO₂) labels refer to the chemical parameters obtained on the same crystals by SIMS and EMP, respectively. **b, right)** Ti vs. OH diagram illustrating the good fit of data with a Ti-oxy exchange (ideal substitution represented by dashed line). Blue datapoints obtained from H contents determined by SIMS. Red ellipses highlight crystals that were also studied by single-crystal X-ray diffraction

References

- [1] B. Cesare et al. (2003) *American Mineralogist* **88**, 583-595
- [2] B. Cesare et al. (2008) *American Mineralogist* **93**, 327-338
- [3] L. Tajcmanova et al. (2009) *Journal of Metamorphic Geology* **27**, 153-165
- [4] A.M. Alvarez-Valero & L.M. Kriegsman (2010) *Lithos* **116**, 300-309

Volatiles in volcanic systems undergoing mafic recharge

M. Edmonds¹, D. Neave¹, M. Plail², M. Humphreys³, J. Barclay², R. Herd²

¹Department of Earth Sciences, University of Cambridge, Downing Street, Cambridge CB2 3EQ, UK

²School of Environmental Sciences, University of East Anglia, Norwich NR4 7TJ, UK

³Department of Earth Sciences, University of Oxford, South Parks Road, Oxford OX1 3AN, UK

Background to study

Intermediate and silicic volcanic eruptions are often triggered by mafic recharge at depth. In many cases evidence for this mafic recharge comes in the form of mafic enclaves, as well as disequilibrium petrological features within the host silicic magma [1]. The volcanic systems that display these features are often associated with “excess degassing”, i.e. the volcanic gas emissions far exceed that which can be explained merely by degassing of erupted magma alone [2]. It has been suggested that the source of these excess volatiles is the recharging mafic magma, which is largely unerupted. There is abundant evidence that recharging mafic magma supplies heat to the resident magma. Commonly, significant mass transfer also takes place between the two magmas (in the form of melt and crystals and perhaps vapour). This study is part of a larger project looking at the volatile budget of andesitic-rhyolitic volcanic centres. We have focussed here on samples of andesite containing mafic enclaves from Soufriere Hills, Montserrat, and samples of peralkaline rhyolite containing trachytic enclaves from Pantelleria, Italy. We analysed rhyolitic glass matrix in the enclaves, and rhyolitic glass inclusions inside phenocrysts (plagioclase, orthoclase), for H₂O, Li and CO₂.

Samples

Soufriere Hills Volcano samples were collected from a pyroclastic flow deposit emplaced in January 2007 in the Belham River Valley. The samples were porphyritic andesite (with rhyolitic matrix glass) containing abundant basaltic andesite inclusions, some of which were glassy and vesicular (15-20 vol% porosity). Pantelleria samples were collected from a range of eruptive units, ranging from 45 to 2.5 ka in age. All of the samples were pyroclastic obsidian and contained <10 vol% phenocrysts (Figure 1).

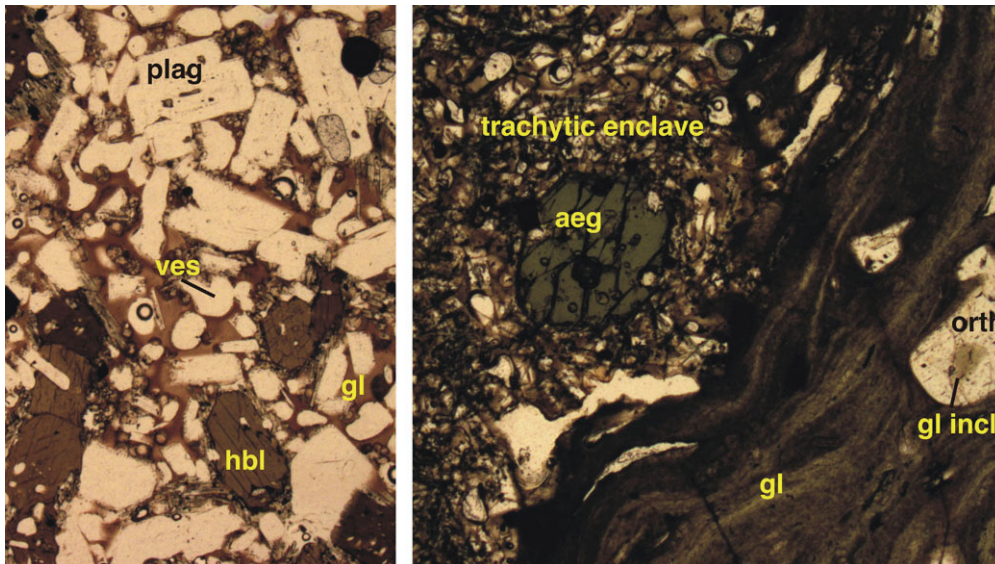


Figure 1. Left: Basaltic andesite enclave in Soufriere Hills Volcano andesite (glass is rhyolitic). Right: Trachytic enclave in peralkaline rhyolite from Pantelleria. Labels plag (plagioclase), ves (vesicle), gl (glass), hbl (hornblende) aeg (aegirine-augite), orth (orthoclase), gl incl (glass inclusion).

Results and preliminary interpretation

The rhyolitic glass in the basaltic andesite enclaves in the Soufriere Hills samples were poor in H₂O (<0.2 wt%) and ranged in CO₂ content from 0-3000 ppm (Figure 1). Some outlier data points with very high CO₂ (> 0.7 wt% and up to 3 wt%) were ascribed to ablating material from cracks on the surface of the thin section that might have harboured relict carbon coating. The range in CO₂ in the

glass was similar to the ranges measured in melt inclusions in lava dome rocks and in pumices (Figure 1; Humphreys, unpublished data).

The results for the enclaves (Figure 2) suggest that they have degassed much of their H₂O during slow magma ascent, but not all of their CO₂. The fractional degassing might be controlled by diffusivity. This will be investigated further.

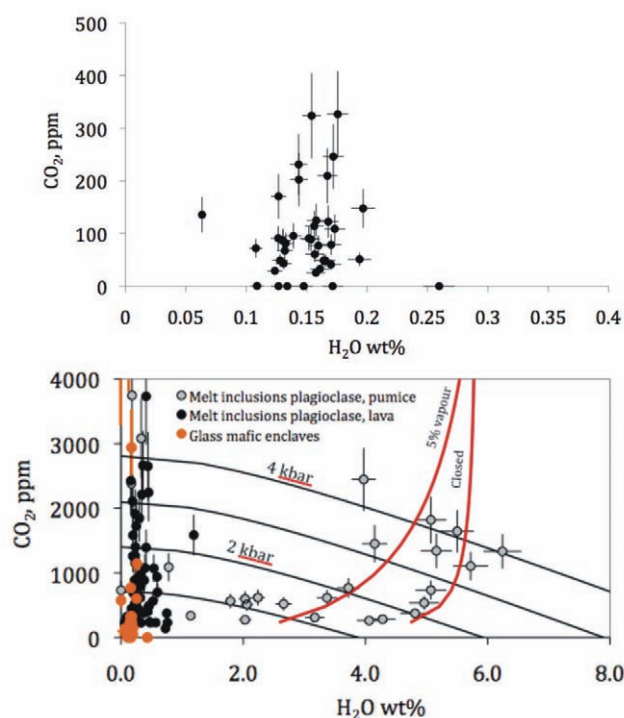


Figure 2. *Top:* H₂O and CO₂ concentrations in matrix glasses of basaltic andesite enclaves (glass is rhyolitic). Error bars are based on repeat analyses of standards.

Bottom: data in context of other analyses of glasses from Soufriere Hills [3]. The H₂O contents of the enclaves are similar to those measured in melt inclusions in lava dome rocks, suggesting they have equilibrated during prolonged magma storage at shallow levels.

Melt inclusions and matrix glasses from the Pantelleria rocks display a range in H₂O from 0 to 4.9 wt% and CO₂ between 0 and 190 ppm (Figure 3). This allows estimation of the equilibration pressure for the melts using VolatileCalc [4].

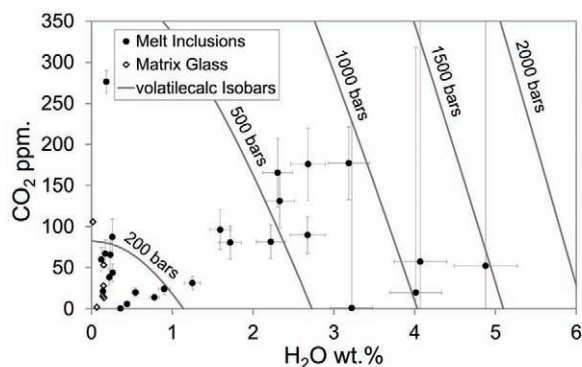


Figure 3. H₂O and CO₂ concentrations in glass inclusions and matrix glasses from Pantelleria.

Other related work

We are conducting a range of related studies on these volcanic systems. For Soufriere Hills, we have extensive electron microprobe data for glasses and phenocrysts, we are also measuring volcanic gases (CO₂, H₂O, SO₂) emitted from the

volcano, and carrying out textural studies of the andesite and mafic enclaves. The Pantelleria results were integrated with a detailed study of melt compositions (major and trace elements) to quantify differentiation, recharge and degassing [5].

References

- [1] M.A. Clyne (1998) *Journal of Petrology* **40**, 105-132
- [2] M. Edmonds et al. (2010) *Geochemistry Geophysics Geosystems*. DOI:10.1029/2009GC002781
- [3] M. Edmonds et al. (2010) AGU Fall Meeting abstract V52C-01
- [4] P. Newman and J. Lowenstern (2002) *Computers and Geosciences* **28**, 597-604
- [5] D.A. Neave et al., *Journal of Petrology* (in review)

The magmatic evolution of Dabbahu Volcano, Afar Rift, Ethiopia

L. Field, J. Blundy

Dept. of Earth Sciences, University of Bristol, Wills Memorial Building, Queen's Road, Bristol BS8 1RJ

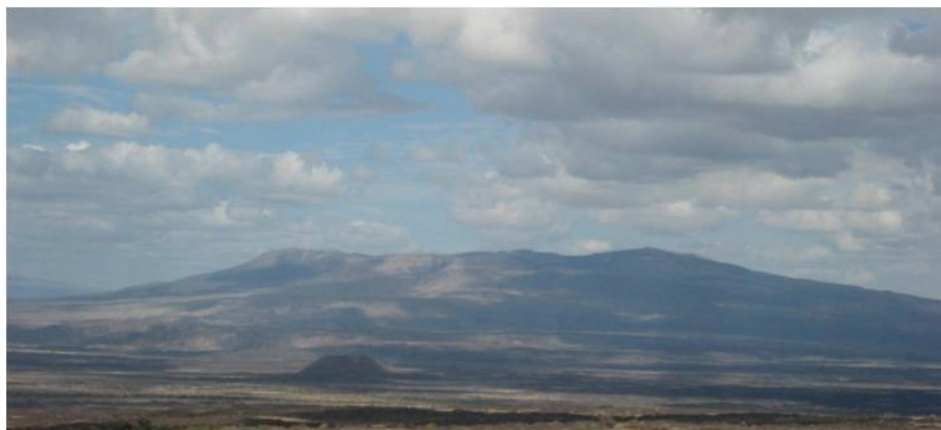


Figure 1. View of Dabbahu from the southwest.

Aims and objectives

The aim of this research is to gain further understanding of magmatic processes occurring in an active continental rift environment. The Dabbahu magmatic centre (Fig. 1), in the Afar region of Ethiopia, burst back into life in 2005 with rifting events associated with the emplacement of basaltic dykes; however the only associated erupted magma was rhyolitic. Analysis of melt inclusions in samples collected from Dabbahu will allow reconstruction of the history of the magma, evidencing any dramatic changes in conditions which have occurred. Phenocryst hosted melt inclusions are used to determine the depth-composition-density evolution of the magma. The NERC studentship is allied to a major interdisciplinary study investigating active magmatism and tectonics in the Afar region, Ethiopia. The larger project aims to track the creation, migration, evolution and emplacement of magma from the asthenosphere to the crust. This work builds on the foundations laid by Barberi, et al. [1], with the aim of gaining more of an understanding of pre-eruption processes and their timescales in continental rift related magma chambers.

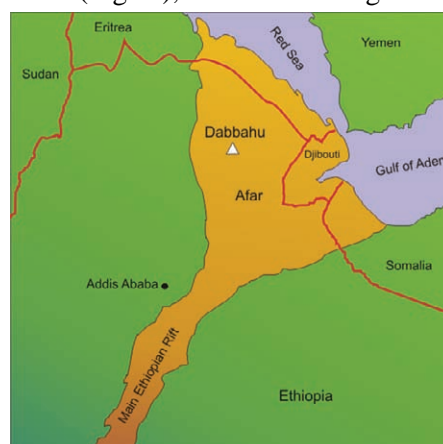


Figure 2. Map showing location of Dabbahu

Analysis

Samples were collected from Dabbahu during the Jan/Feb 2008 fieldseason (Fig. 2). Analysis in 2010 built on the analysis carried out in 2009, on samples from the rhyolitic obsidian flows which dominate the northern half of the volcano. The dominant phenocryst is alkali feldspar (anorthoclase, Fig. 3), although some cpx and fayalite hosted inclusions were also analysed. The lava flows are very young (preliminary Ar-Ar dating suggests the obsidian flows are <4 ka yrs) and therefore the phenocrysts are very fresh, and ideal for ion microprobe analysis. 70 analyses were carried out on melt inclusions and glasses.

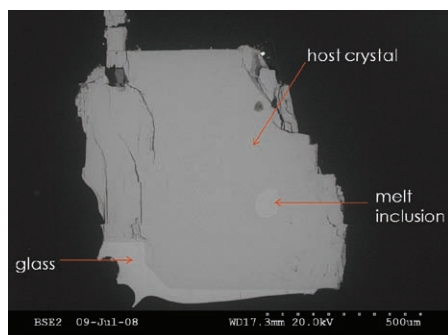


Figure 3. Backscatter SEM image of a typical melt inclusion and the alkali feldspar host

Individual crystals and glass fragments were picked and resin mounted. As ^{12}C was being measured in order to give CO_2 values, the mounts were left uncoated for preliminary SEM work to prevent contamination from the carbon coating. EMPA analysis was also carried out after the SIMS analysis. As well as ^{12}C , ^1H (to give H_2O values) and a range of trace elements were also measured.

Results

150 analyses were made in total across 2009 and 2010. The CO_2 and H_2O values obtained covered a range of values, with the melt inclusions having the highest values, and the pumice and obsidian glass have values at the lower end of the scale, consistent with degassing. H_2O values up to 5.8 wt% were obtained which is consistent with published data for pantellerites e.g. Greater Olkarra VP - 3.4 wt % [2], Eburru, Kenya, up to 5.6 wt % [3]. CO_2 values up to 462 ppm in the feldspar MI and 1457 in cpx hosted ones. Low CO_2 and H_2O values obtained from the matrix glasses indicate the lavas and pumices are largely degassed.

The solubility model of Papale et al. [4] was used to calculate pressure from the CO_2 and H_2O data, as this model does contain some peralkaline data which is known to have a strong compositional dependence in alkali rocks (e.g. Dixon et al. [5], Tamic et al. [6]). Entrapment temperatures for the feldspar hosted MI were calculated using the alkali feldspar – liquid thermometer of Putirka [7]. It was not possible to calculate temperatures for cpx or olivine hosted inclusions due to low to zero MgO contents. The MI analysis has indicated a shallow magma storage area, typical for peralkaline volcanoes, which is vertically extensive over ~ 4 km.

Further work

A paper is in preparation which uses the MI data together with geophysical data to constrain InSAR modelling. The three techniques together suggest magma storage has been stable over the past few thousand years, with historical peralkaline eruptions being sourced from magma storage of a similar size and geometry to that which is sourcing current eruptions.

References

- [1] F. Barberi (1975) *Journal of Petrology* **16**, 22-56
- [2] M.C. Wilding et al. (1993) *Contributions to Mineralogy and Petrology* **114**, 264-275
- [3] B. Scaillet and R. Macdonald (2006) *Lithos* **91**, 95-108
- [4] P. Papale et al. (2006) *Chemical Geology* **229**, 78-95
- [5] J.E. Dixon (1997) *American Mineralogist* **82**, 368-378
- [6] N. Tamic et al. (2001) *Chemical Geology* **174**, 333-347
- [7] K. D. Putirka (2008) *Reviews in Mineralogy and Geochemistry* **69**, 61-120

Past records of ocean acidification - the Palaeogene hyperthermals

L.C. Foster¹, R. W. Hinton², D. N. Schmidt¹, C. Coath¹, A. Ridgwell¹

¹Department of Earth Sciences, Will's Memorial Building, University of Bristol, Bristol, BS8 1RJ, UK

²School of GeoSciences, University of Edinburgh, Edinburgh, EH9 3JW, UK

Project background

The project examines four ocean acidification events during the time interval 58 and 52 Ma, namely: the Early Late Palaeocene, Paleocene-Eocene Thermal Maximum, ELMO, and 'X' events (EPLE, ETM 1,2,3). To allow palaeoenvironmental reconstructions, we are measuring boron isotopes and Mg/Ca ratios in benthic foraminifera from cores covering these time intervals obtained from a range of sites from the Atlantic, Indian and Pacific Oceans. The isotopic fractionation of B in sea water has been shown to be strongly related to pH. Mg/Ca can be used to reconstruct temperature variation. However, the benthic foraminifera in these samples are very thin-walled and furthermore, B concentrations in this species are relatively low (<10 ppm).

Measurements of $\delta^{11}\text{B}$ using 1270

The operating conditions and post processing are outlined in the previous year's report. In summary, O_2^- primary beam were used with a primary beam energy of 12.2 keV and secondary ion energy of 10keV, with illuminating the aperture after the primary mass filter. Surface contamination was minimised using a 30 second pre-sputter with a $\sim 10\mu\text{m}^2$ raster. The integration times for one measurement 'cycle' were optimised to 11s, 3s, 1s and 1s for ^{10}B , ^{11}B , Si^{2+} and Ca^{2+} with waiting time of 3s, 1s, and 1s respectively. Typically, a 'clean' measurement consisted of approximately 60 measurement cycles of useable data. In order to achieve at least 2‰ precision (1σ) for a single specimen it was necessary to combine at least 20 such measurements. With standards this number of repeats was possible in a single day using the 'Chain Analysis' option and 24 hour a day operation. By measuring Ca^{2+} we were able to monitor the ionisation behaviour of the carbonate and interaction with the beam, as well as B/Ca ratio, which can be used to provide information on the palaeoenvironment of the carbonate ion. Measurement of Si^{2+} allows us to determine if there is any contamination, in particular clays which potentially could have high boron content.

Post processing of data

Data points shown to have high Si^{2+} were removed from our analysis. A subsequent check by SEM analysis confirms the position of analysis and has shown that this method for removal is robust (i.e. any spots rejected by SEM analysis had already been rejected by using Si^{2+}). As the B secondary ion signal always decreased slowly with time, the subsequent data processing follows [1] which corrects for any systematic bias caused by the time-varying signal intensity. In addition, this treatment, which time-interpolates then averages each isotope's intensity before taking their ratio, largely avoids the bias which occurs by averaging ratios of individual cycles which is particularly acute in cases of very low count rates.

Application of new technique- preliminary findings

We have analysed foraminifera for $\delta^{11}\text{B}$ and trace elements from Walvis Ridge (1262, 1263), Shatsky Rise (1210), Central Exmouth Plateau (762), central Pacific (1221) and Kerguelen Plateau (1135). We have analysed samples from PETM, ELMO and EPLE events to quantify the changes during each of these hyperthermals and have built up a dataset of potential differences in $\delta^{11}\text{B}$ within different oceans during the PETM.

Some specimens during the EPLE were too small to measure and therefore the number of specimens analysed was limited. The dataset comprises measurements prior to the event and three measurements after the event (but none during). A number of these sites have shown significant diagenetic alteration of the sample (see Fig. 2) and Si^{2+} contamination from clay during analyses (notably 1221 see Fig. 3). This is particularly important in low $\%\text{CaCO}_3$ intervals but also affected carbonate richer ELMO samples. At site 1262, the loss of the carbonate due to the shoaling of the lysocline (and "burn-down" into the sediment) resulted in recrystallisation of the foraminifera also just prior to the event.

Site 1210 Shatsky Rise was analysed only for trace elements due to the small size of the foraminifera (typically two-thirds of the size found at Walvis Ridge). We are presently combining complimentary data to provide a firm basis of determining diagenetic alteration.

Our data show that $\delta^{11}\text{B}$ at Site 1262 was $17.5 \pm 1.6\%$ (1σ) prior to the PETM recovering only partially, to $9.8 \pm 2.3\%$ (1σ) in ~ 500 kyrs. The lack of excursion warming recorded in Mg/Ca is probably due to sediment burn-down. Boron isotopes data for shallower Site 1263 are within error of 1262 values prior to the excursion. Site 1263 also records the excursion itself, with a $\delta^{11}\text{B}$ value of $6.1 \pm 2.5\%$ (1σ) at 55.007 Ma. The data from the other sites will be combined to these initial findings to assess potential reorganization of the ocean circulation.

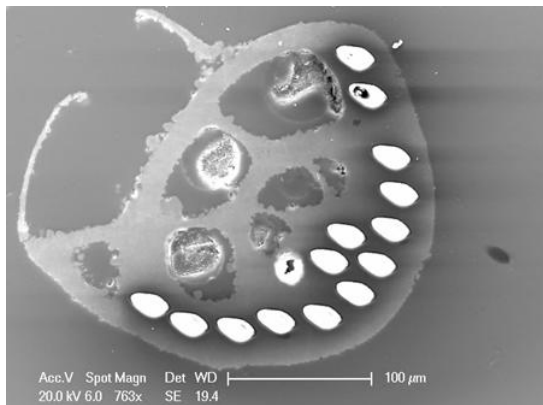


Fig. 1: SEM image of *O. umbonatus* from Central Exmouth Plateau (762) analysed by Cameca 1270 for $\delta^{11}\text{B}$.

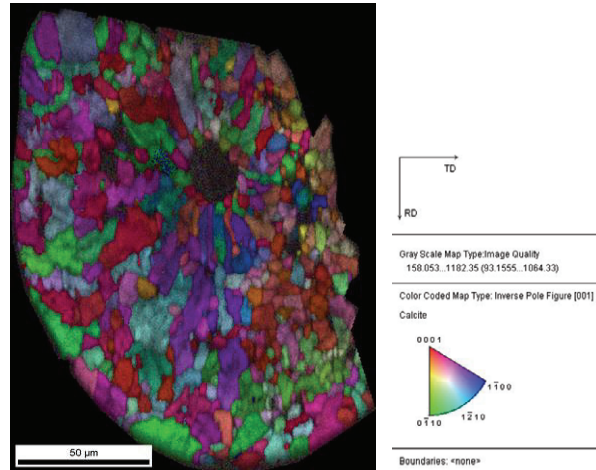


Fig. 2: Diagenetic alteration of *O. umbonatus* analysed by EBSD (site 1221C 11X3 2-3cm) which shows pattern indicative of recrystallisation.

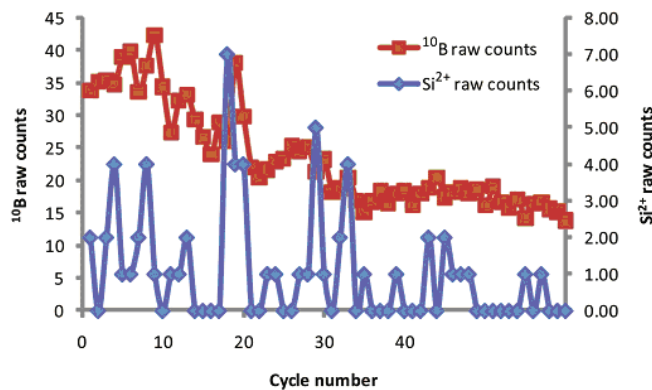


Fig. 3: Analyses of *O. umbonatus* (site 1221C) showing the relationship between ^{11}B counts and presence of Si^{2+} (indicative of clay which has high B content). Note that the relationship between Si^{2+} and ^{11}B counts is non-linear. These were analyses after the pre-spluttering indicating that the clays is found within the test walls themselves not just held within the chambers.

References

[1] K.J. Coakley et al. (2005) International Journal of Mass Spectrometry **240**, 107-120.

$\delta^{18}\text{O}$ & $\delta^{13}\text{C}$ profiles of Atlantic salmon otoliths

N.N. Hanson¹, C.M. Wurster² & C.D. Todd¹

¹Scottish Oceans Institute, University of St. Andrews, St. Andrews KY16 8LB, UK

²School of Earth & Environmental Science, James Cook University, PO Box 6811, Cairns, Queensland, Australia, 4870

Background

Long term declines in Atlantic salmon abundance have been linked to reductions in marine survivorship and, in particular, reductions in growth condition (a measure of fish quality) have been correlated to increased mid-winter sea surface temperature anomalies in the eastern North Atlantic [1]. $\delta^{18}\text{O}$ and $\delta^{13}\text{C}$ values of Atlantic salmon otoliths can act as natural ‘tags’, providing insight into the thermal and metabolic regimes experienced by fish during this elusive life stage. Otoliths are biomineralised aragonite structures of the inner ear. $\delta^{18}\text{O}$ values of otolith aragonite are deposited at or near equilibrium with the ambient water composition; the water temperature during otolith deposition can be resolved provided that $\delta^{18}\text{O}$ values of ambient water are known [2]. When $\delta^{13}\text{C}$ values of dissolved inorganic carbon (DIC) are relatively constant (such as in the North Atlantic Ocean), $\delta^{13}\text{C}_{\text{otolith}}$ values are dominantly reflective of differences in metabolic rate [3]. High resolution $\delta^{18}\text{O}$ and $\delta^{13}\text{C}$ profiles afforded by SIMS analyses provide access to more detailed isotopic profiles than traditional micromilling [4]; by combining these profiles with individual growth condition we addressed two inter-related hypotheses: (1; using $\delta^{18}\text{O}$) that poor condition, underweight one sea-winter (1SW) fish will have occupied significantly warmer waters during their marine residence compared to those returning in good condition; and (2; using $\delta^{13}\text{C}$) that poor condition fish had catabolised energy and protein reserves during the most recent months of return migration (and prior to capture), indicated by a signal of elevated metabolic rate.

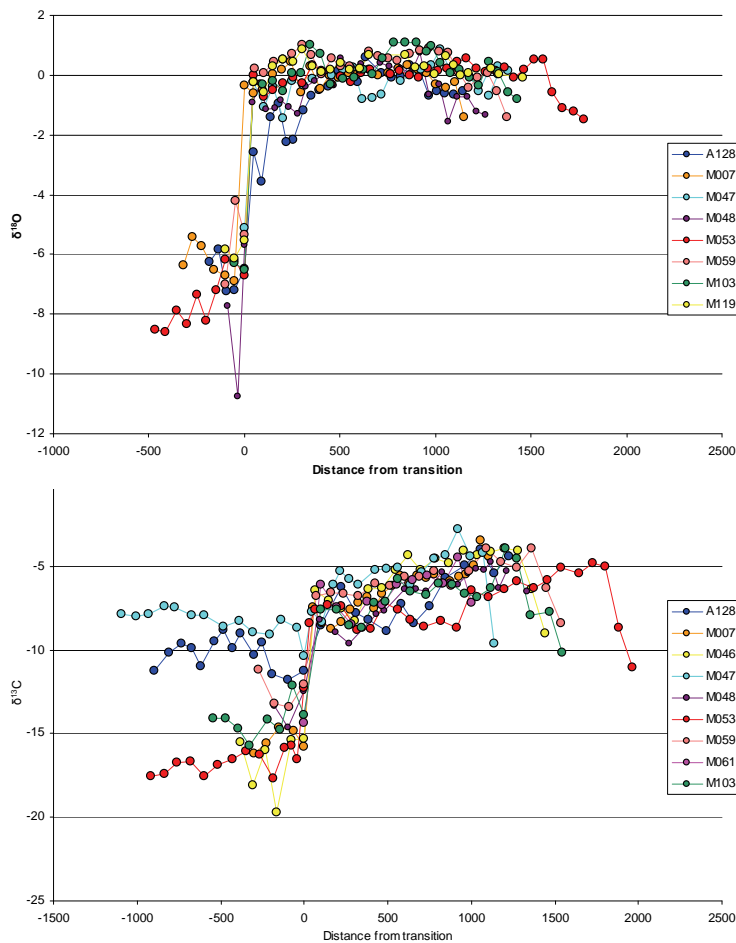


Figure 1: $\delta^{18}\text{O}$ (top) and $\delta^{13}\text{C}$ (bottom) profiles from the fresh-water/marine transition and marine zone of 1SW wild Atlantic salmon otoliths ($n = 8$ individuals for oxygen and $n = 9$ for carbon). Analytical precisions were better than 0.21‰ and 0.43‰ respectively.

Results & Discussion

Between 24 and 34 analyses per otolith were obtained for $\delta^{18}\text{O}$ ($n = 8$ individuals) and 11-24 per otolith for $\delta^{13}\text{C}$ ($n = 9$ individuals). A duplicate $\delta^{18}\text{O}_{\text{otolith}}$ transect, offset by approximately $25\mu\text{m}$ from the original, was completed for M007-09; SEM images guided the matching of points to particular growth zones and the matched profiles were highly correlated ($r^2 = 0.89$; Pearson's product-moment test), demonstrating that the pattern of stable isotope variation is repeatable across multiple transects. All profiles, scaled such that $x = 0$ refers to the freshwater/ marine emigration transition, are presented in Figure 1. There is considerable inter- and intra-individual variability both in oxygen and carbon stable isotopes. Individual A128-09 was particularly different in that the freshwater/marine transition from (oxygen isotope values) was gradual rather than stepped; this persistence of $\delta^{18}\text{O}$ may be

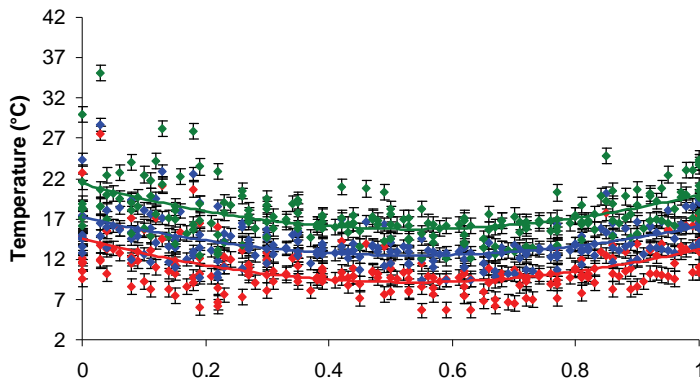


Figure 2: Temperature profiles of all fish combined using a derived equation (red), Storm-Suke *et al.* (blue) and Kim *et al.* (green) scaled by proportionate distance in the marine zone of the otolith

indicative of a prolonged estuarine residence or potentially a southerly river provenance because lighter oxygen isotopes are associated with (a) freshwater and (b) warmer temperatures. Despite inter-individual differences, all fish share common features. Both the oxygen and carbon stable isotope data increase steadily from the onset of marine residency (i.e. smolt emigration) to a point approximately three quarters of the way along the otolith, after which there is a relatively rapid decline. This was most pronounced in carbon (Fig 1). $\delta^{18}\text{O}$ values increased $\sim 1\text{‰}$ from -0.7‰ to a maximum of 0.4‰ , corresponding to a temperature decrease of $\sim 4\text{-}5^\circ\text{C}$. $\delta^{13}\text{C}$ values increased from -7.4‰ to a maximum of -4.8‰ at ~ 0.8 of the proportional otolith distance. Maximum values of oxygen isotopes occurred earlier at ~ 0.6 of the proportional otolith distance. Generalised Additive Model results indicated that both the calendar date of capture and length of the fish are related to the pattern of $\delta^{18}\text{O}$ and $\delta^{13}\text{C}$ variation, although these parameters were most prominent in $\delta^{13}\text{C}$ variation. Condition factor was non-significant ($\alpha > 0.05$) both in the carbon and oxygen analyses, indicating that thermal and metabolic histories are not the primary drivers of return adult condition. Thus, there is no evidence that “skinny” fish experienced warmer conditions and/or higher metabolic rates. Temperatures calculated from $\delta^{18}\text{O}$ values (excluding A128-09) using three different thermometry equations range from 5.6°C to 24.8°C . The ‘derived’ equation (using the slope for inorganic aragonite from Kim *et al.* 2007, and estimating an intercept based on $\delta^{18}\text{O}_{\text{seawater}}$ and coastal SST for the month of capture) provides temperature estimates most concordant with ocean catch data ([5]; i.e. $6\text{-}12^\circ\text{C}$), and was used in conjunction with information on the spatial distribution of $\delta^{18}\text{O}_{\text{seawater}}$ and SST values in the eastern North Atlantic to attempt recreations of salmon migratory routes (for details see [4]). These analyses demonstrate the potential for large differences in individual migration routes and open ocean destinations of wild 1SW Atlantic salmon.

References

- [1] C. D. Todd *et al.* (2008) *Global Change Biology* **14**, 958
- [2] C. M. Wurster *et al.* (2005) *Canadian Journal of Fisheries and Aquatic Sciences* **62**, 700
- [3] C. M. Wurster and W. P. Patterson (2003) *Paleobiology* **29**, 492
- [4] N. N. Hanson *et al.* (2010) *Rapid Communications in Mass Spectrometry* **24**, 2491
- [5] M. Holm *et al.* (2000) *ICES Journal of Marine Science* **57**, 955

Timescales of melting in hot orogens: ‘inside-out’ zircons from the Kerala Khondalite Belt, India

S.L. Harley¹ and V. Nandakumar²

¹School of GeoSciences, University of Edinburgh, Edinburgh EH9 3JW, UK

²Centre for Earth Science Studies, Trivandrum, Kerala, India

Background

An integrated monazite-zircon study of leucosomes and migmatites from the highest-T portion of the Kerala Khondalite Belt of southern India (P-T: 7 kbar, 930°C) has demonstrated that high-percentage melting (>20 vol%), leucogranitic melt migration, and interaction of melt with host rocks consequent on melt ponding and crystallisation occurred over a prolonged time interval of at least 25 Ma, from at least ca. 560 Ma to 535 Ma. Here we report results from one leucosome-rich migmatite (KUL), in which zircons preserve a remarkable textural record of growth, dissolution and modification. We have applied REE analysis to evaluate the growth behaviour of these unusual zircons and inform our strategy for the subsequent zircon U-Pb isotopic dating to be undertaken in the project.

Zircon textures and ‘inside-out’ growth model

KUL zircons preserve complex cores, planar-sector to ‘firtree’ and oscillatory zoned euhedral rim domains (‘bright planar’ and ‘dark planar’), and darker-CL rinds and invasive lobes (Fig. 1a). Complete ‘cores’ have square cross sections, divided into sectors by axial zones of dark-CL zircon that form trellis and feathery structures. Intervening bright-CL sectors contain either an inclusion of quartz or finely crystalline quartzofeldspathic material (Fig. 1b), or a circular to elliptical domain of markedly zoned zircon (Fig. 1a, 1c) that may be continuous with the lobes of invasive darker-CL zircon. Fig. 1c shows a composite zircon grain pair, in which one complex core has later been disrupted and replaced by a truncating lobe or domain of dark-CL zircon. The other complex core is mostly intact, with axial trellis zones, 1 inclusion, 2 circular oscillatory domains and one invasive lobe.

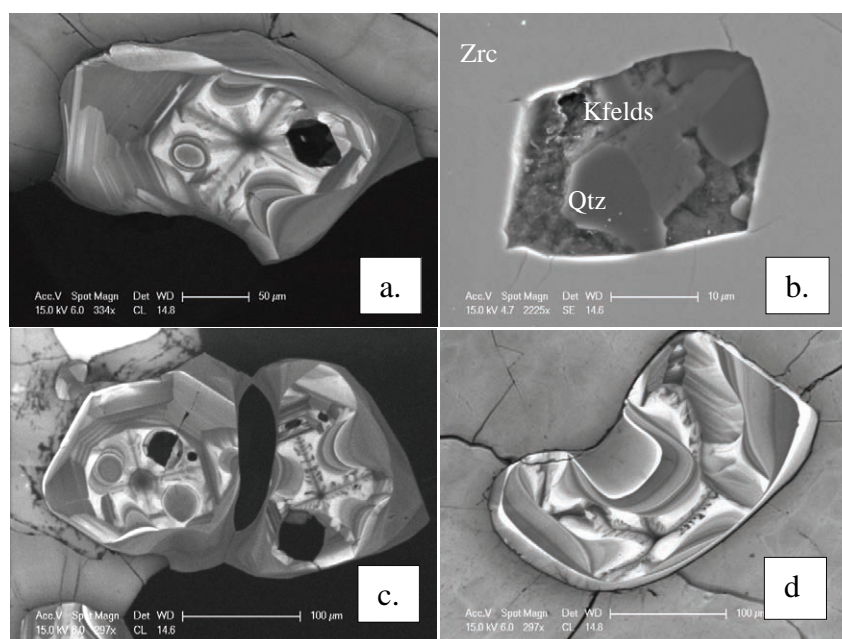


Fig. 1. CL (a, c, d) and SEI (b) images of zircon features in KUL. (a) shows the typical internal features of a zircon with a ‘complete’ core region and outer planar-zoned material, with some invasion of one sector by lobe of modified zircon, circular zircon in another sector, and a preserved former melt inclusion in another. (b) shows a nanogranite inclusion. (c) shows two grains welded together along a dissolution-reprecipitation front. (d) shows a composite of possibly 3 zircons (indicated by the trellis features) highly modified by invasive lobes.

Structurally simpler planar-sector zoned zircon surrounds the complex cores. Two planar-sector zone types occur: those that are brighter in CL (‘bright planar’) and moderately oscillatory, and those that are darker in CL (‘dark planar’) and weakly oscillatory. Both ‘core’ and ‘planar-sector’ type zircon domains are variably truncated, modified or replaced by lobate, curvilinear, ‘swirling’ and cusped zircon domains (‘lobate zircon’) that also form outermost rinds. This lobate zircon, whether on rims or invasive into complex cores, represents the final phase of KUL zircon formation and modification. The timing relationships between the spectacular complex core zircon domains and the planar-sector euhedral zircon zones are ambiguous. The complex cores show internal modifications that appear to truncate or interact with the most ‘internal’ of the planar-sector zones. This, coupled with the common observation of inclusions with negative crystal shapes, similar in mineralogy and microtexture to ‘nanogranite’ [1], suggests that the zircons may have grown as ‘hopper’ crystals in which the planar-

sector euhedral rims grew faster than cores. In this ‘inside-out’ growth model zircon cores would have contained tubes of melt, filled by late-stage zircon growth. This model is evaluated using the REE results, and will be tested further using zircon U-Pb dating

Analytical results

REE and other selected trace elements within zircons and garnets were determined using the EMMAC CAMECA ims-4f ion microprobe. Analytical conditions and correction procedures follow those of Harley & Kelly [2]. Analyses were conducted using a 6 nA O⁻ primary beam. Secondary ions were extracted at 4500V and measured at a 120eV high-energy offset for zircon and 75eV energy offset for garnet. Trace element abundances were calibrated against the NIST-610 glass standard and ion yields corrected by reference to zircon SL1 and garnet DDI garnet.

Trace element chemistry allows distinction of the texturally-defined bright-CL planar zircon from the dark-CL, weakly zoned but undisturbed zircon cores, elliptical / circular modified core zircon, and lobate invasive zircon. The former shows elevated and fractionated HREE (red diamonds in Fig. 2), moderate Th/U>0.3 and low U/Yb = 2.8. The latter types, grouped together on Fig. 2, have moderate and flat HREE, Th/U<0.3, and high U/Yb (20-64). Details of these zircon chemistries and the measured garnet REE features are provided in the captions to Fig. 2 and Fig. 3.

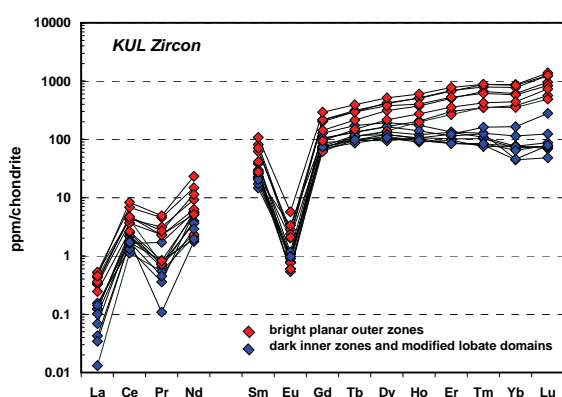
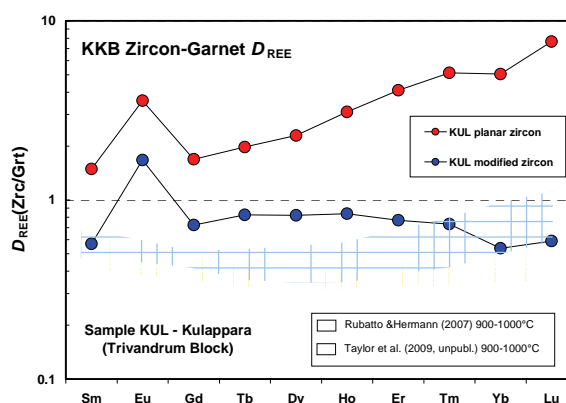


Fig. 3. Distribution of MREE-HREE between the two zircon textural types and garnet in KUL. Pairing of the planar-sector zoned zircon with garnet yields D_{HREE} that range from 1.7 at Gd to 5.1 at Yb, far removed from equilibrium. Pairing of the dark-zoned and modified zircon with garnet yields D_{HREE} that overlap with the preferred empirical equilibrium values at 850-1000°C [3] and lie within range of experimental D_{REE} results [4,5]. KUL zircon has undergone its late-stage crystallisation and modification in the presence of and in close equilibrium with garnet.

Fig. 2. Zircon Rare Earth Element patterns. Bright-CL planar-sector and axial zircon domains are high and fractionated in HREE ($\text{Yb}_n/\text{Gd}_n = 5.7 - 2.7$; $\text{Dy}_n = 140-520$) compared with darker-CL planar, interior lobate and modified domains, which have flat HREE ($\text{Yb}_n/\text{Gd}_n = 0.9$; $\text{Dy}_n = 130$). Garnet patterns (not shown) are characterised by flat HREE ($\text{Yb}_n/\text{Gd}_n = 1.2$) at $\text{Dy}_n = 165$.



Interpretation

The REE data indicate that only the darker-zoned and modified zircon, formed in the presence of melt, approached equilibrium with host-rock garnet. Initial zircon crystallisation from melt, producing ‘hopper’ type zircon with outer planar-sector zoning, occurred in a melt-rich open system prior interaction of the melt with garnet. Garnet-melt interaction later accompanied the continued precipitation of zircon as modified lobes and tubes filling melt-bearing zircon grains as the melt crystallised. The age of this phase of melt crystallisation, interaction and garnet-zircon-melt equilibration is at least 535 Ma, the age obtained from the main monazite population in KUL.

References

[1] B. Cesare et al. (2009) *Geology* **37**, 627-630 [2] Harley and Kelly (2007) *Chemical Geology* **241**, 62-87. [3] Harley et al. (2007) *Elements* **3**, 25-30. [4] Rubatto and Hermann (2007) *Chemical Geology* **241**, 38-61. [5] Taylor et al., (personal communication).

Geochemical variation in the melt source region beneath the Askja volcanic system, North Iceland

M.E. Hartley, T. Thordarson & J.G. Fitton

School of GeoSciences, University of Edinburgh, Edinburgh EH9 3JW, UK

Background

Current debate on Icelandic volcanotectonic episodes that simultaneously activate the central volcano and the associated fissure swarm centres around two contrasting ideas:

- (a) The lateral flow hypothesis [1]. Magma replenishment, pressurisation of a shallow crustal chamber and subsequent lateral injection of shallow crustal dykes into the fissure swarm is viewed as the driving mechanism of rifting on the volcanic system.
- (b) The magma reservoir hypothesis [2]. Volcanotectonic episodes are driven by magma pressurisation in large and elongate reservoirs at the base of the crust (>20 km depth) and subsequent injection of subvertical dykes into the upper crust.

The Askja volcanic system, north Iceland, is an ideal laboratory for testing these hypotheses, since both the central volcano and the fissure swarm were activated during the well-documented volcanotectonic episode of 1874-1876, most noted for the explosive, silicic eruption at Askja on 28th-29th March 1875. Basaltic activity during this period included small eruptions at Askja central volcano, and the Nyjahraun fissure eruptions, ~60 km north of Askja, which were active between February and November 1875.

Previous studies noted a strong whole-rock compositional similarity between Nyjahraun and several small-volume basaltic lavas erupted in the Askja caldera during the early 20th century. It was therefore proposed that the Nyjahraun lavas were fed by lateral flow from a shallow crustal holding chamber beneath the Askja central volcano, thus supporting hypothesis (a). However, existing major and trace element data are not conclusive in differentiating hypothesis (a) from (b). In particular, previous work has shown that Nyjahraun has a mantle $\delta^{18}\text{O}$ signature of +5.5‰ [3], suggesting that the Nyjahraun magma did not interact with the Askja shallow crustal magma reservoir prior to its eruption.

Previous studies have also suggested that the Holuhraun fissure eruption, ~20 km south of Askja, and two phreatomagmatic tuff sequences found within the Askja caldera, were erupted during the 1874-76 volcanotectonic episode [4]. Although it has since been shown that the two tuff cones were erupted over 2900 years BP, they represent the most primitive basaltic magma erupted within the Askja caldera. As such, their composition may be representative of basaltic magma upwelling beneath the Askja central volcano.

Objectives

We analysed trace and rare earth elements and oxygen isotopes in melt inclusions and groundmass glasses from various eruptions on the Askja volcanic system thought to relate to the 1874-76 volcanotectonic episode. The aims of the study were: to test the lateral flow hypothesis using the geochemical characteristics of melt inclusions and groundmass glasses from basaltic lavas and tephras erupted during the 1874-76 volcanotectonic episode and the early 20th century; to determine whether Holuhraun was associated with the 1874-76 volcanotectonic episode; and to determine whether the composition of the two Askja tuff cones is representative of the basaltic magma upwelling beneath Askja during the 1874-76 volcanotectonic episode.

Results

REE and trace element ratios have shown that Holuhraun has a different source composition to the two Askja tuff sequences. Therefore, Holuhraun was not connected with the 1874-76 Askja volcanotectonic episode. Holuhraun is also compositionally more similar to samples from the Veiðivötn volcanic system than to samples from Askja (Fig. 1). This has important implications for our understanding of how volcanic systems are delineated beneath the north-west sector of Vatnajökull glacier.

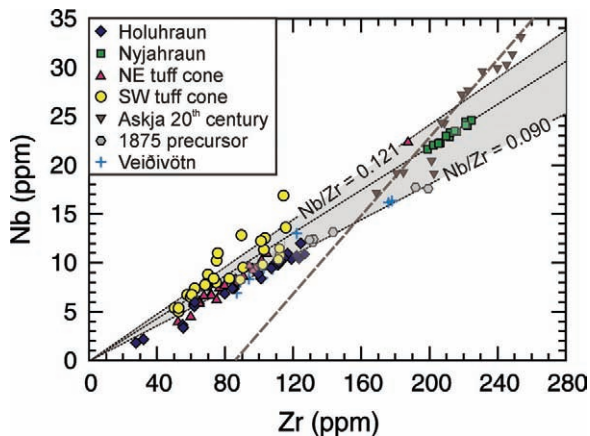


Figure 1. Nb/Zr ratios show that Holuhraun is more similar to lavas of the Veiðivötn volcanic system than lavas from Askja. The two tuff cones and Nyjahraun have Nb/Zr ratios consistent with evolution by fractional crystallisation. The Askja 20th century basalts show evidence of mixing with a Zr-rich contaminant.

The two Askja tuff sequences, despite having more primitive compositions than basaltic precursors to the 28th-29th March 1875 eruption, have almost identical trace element ratios to these precursor basalts. These tuff sequences are therefore thought to be compositionally representative of primitive basaltic melts supplied to the Askja central volcano.

Nb/Zr ratios reveal that groundmass glasses from the Askja 20th century eruptions show evidence of magma mixing with a Zr-rich contaminant, most probably rhyolitic magma resident in Askja's shallow magma chamber. However, melt inclusions and groundmass glasses from Nyjahraun do not show evidence of contamination or magma mixing, but evolved through a process of simple fractional crystallisation (Fig. 1). Thus, while the Askja 20th century basalts evolved via mixing with partial melts in the crust, the Nyjahraun magma evolved without such interactions. This suggests that Nyjahraun did not share a magma source with the Askja 20th century

basalts, and thus was not sourced by lateral flow from the Askja magma chamber.

Melt inclusions and groundmass glasses from Holuhraun have mantle-like $\delta^{18}\text{O}$ signatures (Fig. 2). Major and trace element abundances and ratios show that much of this variation is explained by fractional crystallisation. Some melt inclusions from the two Askja tuff cones have mantle-like $\delta^{18}\text{O}$, but more commonly have lower $\delta^{18}\text{O}$ consistent with magma mixing or crustal contamination. Trace element ratios show that the NE tuff sequence appears to have inherited its low $\delta^{18}\text{O}$ signature by mixing with a rhyolitic contaminant. The low $\delta^{18}\text{O}$ of the SW tuff sequence is more consistent with alteration by low- $\delta^{18}\text{O}$ hydrothermal fluids. Our results suggest that most Nyjahraun samples do not have a mantle-like $\delta^{18}\text{O}$, but they are less contaminated than the Askja 20th century basalts.

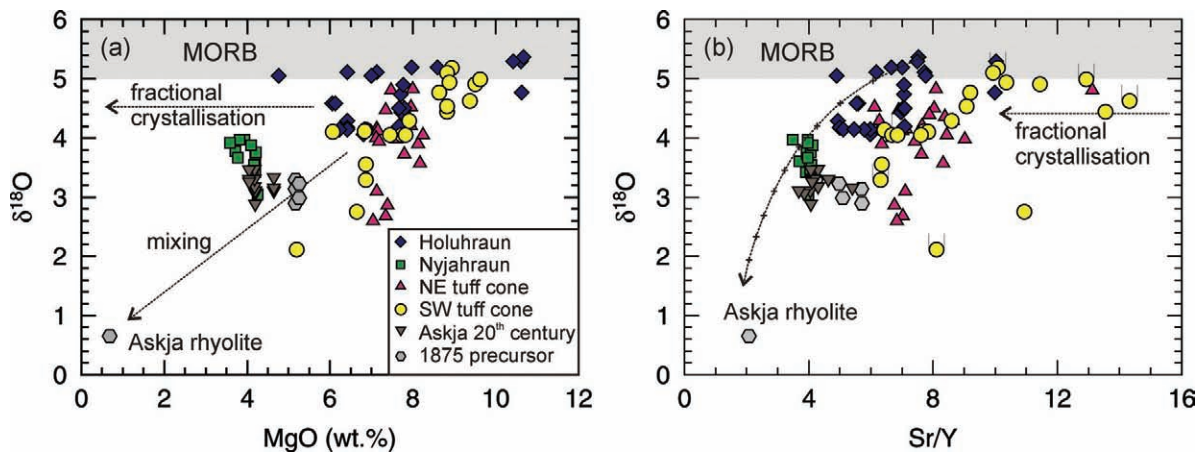


Figure 2. Variations in $\delta^{18}\text{O}$ vs MgO and Sr/Y for melt inclusions and glasses from the Askja volcanic system.

References

- [1] H. Sigurðsson, H. and R.S.J. Sparks (1978) *Bulletin of Volcanology* **41**, 149-167
- [2] A. Gudmundsson, J. (1995) *Journal of Volcanology and Geothermal Research* **64**, 1-22
- [3] R. Macdonald et al. (1987) *Mineralogical Magazine* **51**, 183-202
- [4] R.J. Carey et al. (2010) *Bulletin of Volcanology* **72**, 259-278

Geospeedometry of lithium isotopes in chondrites

J. Harvey^{1,2}, I.J. Parkinson¹, M.A. Fehr¹, R.H. James³, P.A. Bland⁴, M.A. Sephton⁴

¹ Department of Earth & Environmental Sciences, The Open University, Milton Keynes MK7 6AA

² Current address School of Earth & Environment, University of Leeds, LS2 9JT

³ National Oceanography Centre, University of Southampton, SO14 3ZH

⁴ Impacts and Astromaterials Research Centre, Imperial College London, SW7 2AZ

Background: Large ranges (up to 50 ‰) of $\delta^7\text{Li}$ in single mineral grains from terrestrial and meteorite samples are not uncommon^[1-3], and have been attributed to the difference in diffusion rates between ^7Li and ^6Li . This difference in diffusion rates is a direct result of the 16 % mass difference between ^7Li and ^6Li and both experimental and empirical studies indicate that ^6Li diffuses ~3.5 % faster than ^7Li ^[e.g. 4]. Diffusion is therefore a viable mechanism for generating a wide spectrum of $^7\text{Li}/^6\text{Li}$ ratios during high-temperature processes, for example during the growth of crystals in a cooling silicate melt. Experimentally determined Li diffusion rates are very high in both melts^[5,6] and silicate minerals^[7,8] relative to other cations, and so Li isotopic fractionation by diffusion occurs over short timescales. This potentially makes Li isotope fractionation an ideal tool for quantifying extremely rapid cooling events such as rates of chondrule formation^[9]. Rapid crystallisation may also result in the preservation of primary Li isotope ratios in chondrule phenocryst cores, and thus the Li isotope characteristics of the medium from which chondritic meteorite parent bodies were formed can be derived.

An electron microprobe and laser ablation ICP-MS reconnaissance study has allowed us to characterize a large number of chondrules and has already led to the identification of several with core to rim variations in Mg# (0.998 – 0.713) with concomitant variations in [Li] suitable for analysis by ion microprobe (i.e. [Li] \geq 1 ppm). As observed in terrestrial magmatic systems^[4] lithium concentrations tend to increase from chondrule cores towards the rims, where chondrules are in contact with chondrite matrix/mesostasis which commonly has a higher Li concentration (several ppm).

Testable Hypotheses: 1) Profiles of Mg# in our chondrule olivines suggested that they have primary core compositions, and this should also be true for Li isotopes on the basis of diffusion rates^[4]. Lithium concentration and Li isotope profiles can test this proposition and will be modelled in terms of diffusional equilibration^[2,4,9]. This modelling will provide information about the timescale and composition of any Li perturbation at the grain boundary and subsequent diffusion. We can then evaluate the range of primary $\delta^7\text{Li}$ found in chondrules and understand its distribution in chondritic meteorites.

2) Diffusional modelling of transects across individual chondrule phenocrysts will allow a calculation of the formation and cooling rate of the chondrules^[9].

Results: During two analytical sessions (10/5/2010 to 15/5/2010 and 6/12/2010 to 7/12/2010) 143 Li isotope and abundance measurements were made on phenocrysts in 22 chondrules from 5 classes of unequilibrated chondritic meteorites (CV, CO, CM, LL & H) and 4 in-house olivine standards. Measurements of both lithium isotopes and lithium abundance were made across the diameter of individual phenocrysts. The measured range of Li isotope ratios in chondrule phenocrysts in this study is an order of magnitude greater than that reported for bulk rock CV, CO, CM, LL & H meteorites (Figure 1) but the range obtained is consistent with the large degrees of fractionation of ^6Li from ^7Li observed in Li isotope diffusion studies in mafic phenocrysts reported elsewhere^[e.g. 2-4]. Unlike the other meteorite classes investigated here, the range of $\delta^7\text{Li}$ observed in bulk-rock measurements of H chondrites does not overlap with the $\delta^7\text{Li}$ of the chondrule phenocrysts from H chondrites; the bulk-rock values being significantly lower. Conversely, although within the range of $\delta^7\text{Li}$ for chondrule phenocrysts, both CO and CV bulk-rock measurements are towards the upper range of those derived for the corresponding chondrule phenocrysts.

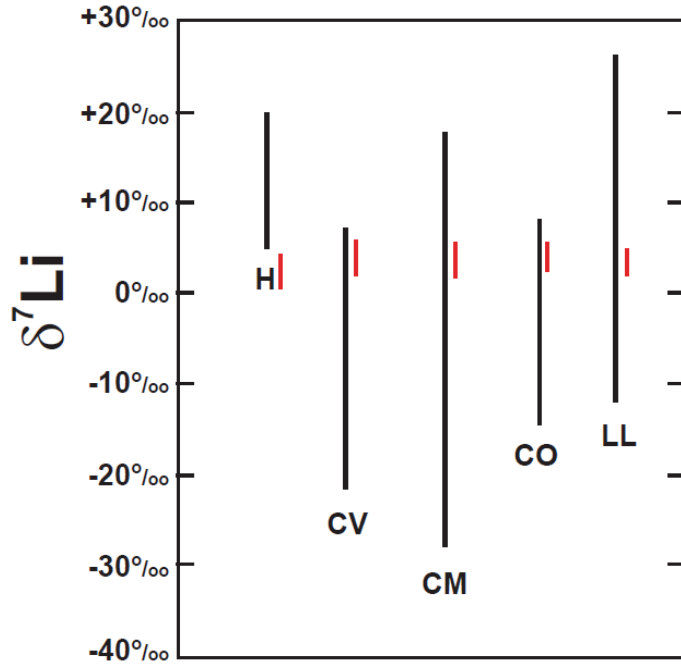


Figure 1. $\delta^7\text{Li}$ ranges for analyses of chondrule phenocrysts from this study (black lines) versus corresponding bulk-rock measurements red lines ^[11]

Both LL and CM chondrite bulk-rock $\delta^7\text{Li}$ values are however close to the mean $\delta^7\text{Li}$ obtained for their corresponding chondrule phenocrysts. At the present time the significance of this observation remains uncertain. In 7 chondrules (CO n=1, CV n=1, CM n=2, LL n=3) resolvable differences in Li isotopes between core and rim were identified, despite an unexpected paucity of Li (<1 ppm) in many of the analysed phenocrysts. However, where Li isotope variability was identified it was not possible to make measurements with a high enough spatial resolution such that Li isotope diffusion profiles could be discerned. This was due to unexpectedly low [Li]; consequently larger than originally anticipated beam sizes were required in order to assure the requisite degree of analytical precision. Therefore, although it was possible to make multiple measurements on individual phenocrysts the lack of spatial resolution attained by our

measurements means that at this stage it is not possible to interpret the data produced in the context of diffusion profiles; there is not enough data of suitable precision to model cooling rates of chondrule phenocrysts. Our measurements also revealed no resolvable difference in Li isotope ratios of chondrule phenocryst cores within a discrete class of chondrite. Similarly, different classes of chondrite cannot be distinguished on the basis of variations in the Li isotope ratios of their chondrule phenocryst cores.

Translating this wide range of Li isotope ratios into useful diffusion-related processes will be difficult as an initial examination of the data produced suggests that the distribution of Li in the chondrule phenocrysts is not consistent with a simple crystallization history alone. Mg-Fe diffusion profiles should be spatially related to Li isotope fractionation; phenocrysts with primary Mg# in their core and large differences between core and rim Mg# were targeted as being the most likely crystals to preserve a cooling history for the chondrules based upon the diffusion of Li isotopes. On reflection, it now seems unlikely that Mg-Fe diffusion profiles (and by analogy Li isotope diffusion profiles, should they be resolvable) are primary and rather represent the results of secondary processes instead of crystallization from a molten liquid. Large phenocrysts that have been fractured exhibit pronounced zoning of Mg-Fe in their individual sub-grains – this is not consistent with diffusion profiles derived from the initial crystallization of the phenocrysts and it seems more likely that in many instances any diffusional information preserved in these phenocrysts is the result of secondary processes, e.g. weathering or reheating.

References

- [1] Lundstrom et al., (2005) *Geochimica et Cosmochimica Acta* **69** 735–751. [2] Beck et al., (2006) *Geochimica et Cosmochimica Acta* **70** 4813–4825. [3] Jeffcoate et al., (2007) *Geochimica et Cosmochimica Acta* **71** 202–218. [4] Parkinson et al., (2007) *Earth and Planetary Science Letters* **257**, 609–621. [5] Richter et al., (2003) *Geochimica et Cosmochimica Acta* **67** 3905–3923. [6] Lundstrom, (2003) *Geochemistry Geophysics Geosystems* **4** (2001GC000224). [7] Giletti et al., (1997) *Chemical Geology* **139** 3–20. [8] Coogan et al., (2005) *Earth and Planetary Science Letters* **240** 415–424. [9] Bějina et al., (2009) *Physics of Earth and Planetary Interiors* **172**, 5–12. [10] Gallagher & Elliott, (2009), *Earth and Planetary Science Letters* **278**, 286–296. [11] Seitz et al., (2007), *Earth and Planetary Science Letters* **260**, 582–596.

U-Pb dating of the felsic footwall succession to the Cosmos nickel-sulfide deposits, Agnew-Wiluna greenstone belt, Yilgarn Craton, Western Australia

A. Kaye and T.Thordarson

School of GeoSciences, University of Edinburgh, Edinburgh EH9 3JW, UK

Introduction

The Archean Yilgarn Craton of Western Australia contains some of the most economically important nickel sulfide deposits in the world. The majority of these are hosted by thick ultramafic bodies that are interpreted to represent preferred lava pathways within large komatiite flow fields constructed by endogenous growth and inflation. The komatiite lavas became sulfur-saturated by the thermal and mechanical erosion of an underlying, often felsic substrate, promoting formation of immiscible sulfides. The Yilgarn Craton consists of metavolcanic and metasedimentary rocks, granites and granitic gneisses formed between 3.05-2.62 Ga. The Eastern Goldfields Superterrane of the Yilgarn craton is a linear, bimodal (mafic-ultramafic and felsic) volcanic greenstone belt sandwiched between voluminous granitoid bodies that range in age from 2760-2620 Ma [1]. SHRIMP U-Pb zircon ages indicate a major peak in volcanism between 2720-2650 Ma, with lesser peaks at 2950 Ma and 2810 Ma [1,2]. Current data indicates that the majority of the ore-hosting komatiites in the eastern part of the Yilgarn craton were deposited between 2713-2672 Ma [3].

Nickel Australasia's Cosmos mine is situated in the eastern part of the Yilgarn Craton within the Agnew-Wiluna belt of the Kalgoorlie Terrane, which is part of the Eastern Goldfields Superterrane. No dates currently exist for this ultramafic, intermediate and felsic succession and dating and geochronology in the surrounding region (Sir Samuel sheet area 1:250,000; [3]) is poorly constrained. A deformed felsic volcanic rock from the Rockys Reward mine near Leinster has a SHRIMP U-Pb zircon age of 2720 ± 14 Ma (4) whereas dating of the coherent dacite sequence in the Mt Keith region has yielded an age of 2706 ± 6 Ma (5).

Aim

U-Pb dating has been undertaken on zircons separated from four felsic units within the felsic footwall, one from an irregular, patchy felsic horizon contained within the Cosmos ultramafic and two later formed felsic porphyry intrusions. The aim is to develop the geochronology for the Cosmos succession. From these dates, we hope to bracket the age of the sulfide-hosting Cosmos ultramafics, and therefore the age of mineralisation.

Results

Zircon dating was performed on ~80 zircons obtained from seven separate felsic units in the Cosmos succession. Many of the zircons are small or in the range of $\sim 50 \mu\text{m}$ - $200 \mu\text{m}$ in diameter. Unfortunately a large fraction of the zircon grains were badly fractured, most likely due to radiation damage, thus it was difficult to locate areas large enough to be analysed at the standard beam size. Despite careful selection of the least fractured zircons, many analysed zircons still had high common lead concentrations and a large portion of the analyses were discordant, possibly due to the effect of later metamorphic events combined with the elevated common lead in the zircons.

Despite these difficulties, concordant dates were obtained for all but one of the analyzed stratigraphic units and these are summarised in the table below. They are listed in stratigraphic order starting with the units situated deepest in the footwall, and therefore considered to be older, then those at shallower position within the footwall, and finally later cross-cutting intrusions, which are considered to be youngest. These results are preliminary and treated accordingly. Further dating of a deeper footwall unit and two hanging wall units will hopefully be completed later in the year, as well as further dating of existing samples to obtain more concordant dates to improve the statistical significance of the data.

Discussion

Despite the limited amount of data, which as of yet has not been fully processed, clear age differences within the Cosmos succession can be seen. Felsic footwall rocks overall have an approximate $\text{Pb}^{207}/\text{Pb}^{206}$ age range of 2725-2729 Ma (± 3 -4Ma), which is older than much of the existing ages from

footwall rocks in other similar Ni-sulfide deposits within the Agnew-Wiluna greenstone belt. This supports the existing interpretation that the Cosmos succession is situated in a different ultramafic sequence to other ultramafic-hosted deposits in the east of the belt, such as Mount Keith and Perseverance. The two felsic porphyry intrusions are much younger: – the footwall intrusion is the youngest unit present with a Pb^{207}/Pb^{206} age of 2649 ± 4 Ma with the hanging wall intrusion occurring significantly earlier at 2679 ± 7 Ma. The above dates put some very broad constraints on the age of the eruption and mineralisation within the Cosmos ultramafic as both porphyries cross-cut the Cosmos ultramafic and therefore postdate its eruption and emplacement. The obtained ages clearly place the eruption of the Cosmos ultramafic lavas and associated sulfide mineralisation between 2725 Ma (± 3) and 2679 Ma (± 7) and the age for the AMD346 coherent dacite suggests emplacement around 2693 ± 4 Ma, which is in keeping with the age constraints of other ore-hosting komatiites in the eastern part of the Yilgarn craton of ~ 2713 - 2672 Ma (5). We stress, however, that these are tentative conclusions and hope to improve the statistical significance of these results with future work.

Table 1. Summary of concordant dates (in millions of years) obtained from six different felsic units within the Cosmos succession. The samples are arranged in order of stratigraphic position (age), with the oldest at the top. This established stratigraphic order is confirmed by the obtained age determinations. The late stage intrusions listed at the bottom of the table are considerably younger than the continuous extrusive succession.

| sample number | sample type | stratigraphic position | # concordant analyses | average $^{206}Pb/^{238}U$ age | average $^{207}Pb/^{235}Pb$ age | average $^{207}Pb/^{206}Pb$ age |
|---------------|--------------------------------|---|-----------------------|--------------------------------|---------------------------------|---------------------------------|
| BJD328F | Coarse-grained coherent dacite | Deepest footwall unit analysed | 11 | 2742 ± 31 | 2735 ± 13 | 2729 ± 3 |
| BJD090 | Dacite lava | Underlies Dacite Lapilli Tuff | 4 | 2732 ± 26 | 2729 ± 11 | 2727 ± 4 |
| BJD085 | Dacite lapilli tuff | Immediate Footwall unit to Cosmos Um | 2 | 2680 ± 31 | 2706 ± 13 | 2725 ± 3 |
| AMD346 | Coherent dacite | Internal to the Cosmos Um at a reactivation contact | 2 | 2705 ± 29 | 2698 ± 13 | 2693 ± 4 |
| BJD320 | Felsic porphyry intrusion | Intrudes between Cosmos Um upper contact and Hanging Wall Felsics/Sediments | 3 | 2665 ± 27 | 2673 ± 12 | 2679 ± 7 |
| AMD273 | Felsic porphyry intrusion | Intrudes around Cosmos Um basal contact and Felsic FW | 4 | 2646 ± 26 | 2648 ± 11 | 2649 ± 4 |

Further work

We plan to analyse additional units from the footwall as well as the hanging wall to the Cosmos ultramafic to improve the chronology of the Cosmos succession and better constrain the age of the ore-hosting ultramafic lavas.

References

- [1] Cassidy *et al.* (2006) Western Australia Geological Survey, *Record 2006/8*, 8p.
- [2] Nelson, D.R. (1997) Western Australia Geological Survey, *Record 1997/2*, 189p.
- [3] Lui *et al.* (2002) Western Australia: Geoscience Australia, *Record 2002/14*.
- [4] Nelson, D.R. (1998) *Earth and Planetary Science Letters* **158**, 109-119.
- [5] Rosengren *et al.* (2008) *Precambrian Research* **161**, 34-52, and references therein.

Archaean to Early Proterozoic crust generation in north-west Scotland

P.J. Lancaster, C.D. Storey & C.J. Hawkesworth

Department of Earth Sciences, University of Bristol, Bristol BS8 1RJ, UK

Introduction

The study of Earth's earliest continental crust is hampered by the lack of primary material older than ~4Ga and a very limited distribution older than 3Ga. Instead, we must turn to the detrital record, which can preserve refractory minerals that grew in these older rocks long after the parental rocks have been destroyed. Zircon is one such refractory mineral, capable of preserving its chemical and isotopic composition up to granulite facies conditions [1]. As a result, it often survives multiple crystallisation events, with each event recorded and preserved in sequence. Modern *in situ* techniques, such as ion microscopy and laser ablation inductively-coupled plasma mass spectrometry (LA-ICP-MS), sample material on such small scales that clusters of growth zones can be characterised.

Zircon incorporates three relevant isotopic signatures into its structure: U–Pb for zircon crystallisation ages, ϵHf for mantle extraction model ages of the parental melt, and $\delta^{18}\text{O}$ for tracking contamination of parental melts with sedimentary contributions from the pre-existing continental crust. Much recent work has combined U–Pb crystallisation and Hf model ages to identify pulses of crustal production in some of the world's oldest zircons, including the Jack Hills, the Acasta Gneiss and the Limpopo Belt [2-4]. However, these zircons are restricted in number, and limit the study of any changes in crustal production since ~3Ga. One of the largest continental cratons, Laurentia, remains largely unstudied beyond U–Pb provenance work. Detrital remnants of the region are now scattered around the northern Atlantic from Canada to Scotland [5-9].

Eighteen samples were collected across the rock sequence in north-west Scotland, from Archaean basement gneiss to Neoproterozoic quartzites, of which thirteen produced enough zircons for analysis. Zircons were separated by traditional methods, and mounted in epoxy resin mounts along with suitable standards. All oxygen isotope measurements and some U–Pb analyses in this study were measured on the Cameca ims-1270 multi collector ion microprobe at Edinburgh. Most U–Pb and all Hf isotope measurements were made by LA-ICP-MS at the University of Bristol. Where U–Pb analyses were measured by both techniques, the results were typically indistinguishable within the stated precision. All U–Pb and $\delta^{18}\text{O}$ analyses were standardised using bracketing analyses of international standard 91500; all $\delta^{18}\text{O}$ analyses are reported relative to VSMOW.

Results

A wide range of $\delta^{18}\text{O}$ values was obtained from 844 analyses, of which 686 avoided cracks, inclusions and other irregular features (81%). Nearly half (45%) record basalt-like values, while a third range as high as 12.2‰. The remainder preserve values of less than 5.0‰, reaching as low as 2.3‰ (and one analysis of -2.1‰). There are no obvious core to rim trends in the data sample (Fig. 1), nor is there any simple correlation between U–Pb age and oxygen value.

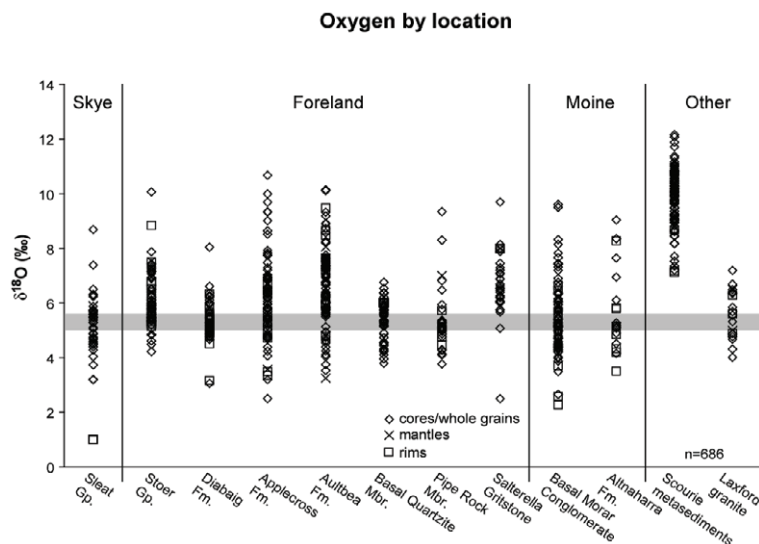


Figure 1. All oxygen analyses sorted by sample (in stratigraphic order) and zircon growth zone. Diamonds - cores and whole grains; crosses - mantles; squares - rims. Grey bar indicates expected range of oxygen values in zircons crystallising directly from mantle material.

The U–Pb crystallisation ages range from 1059Ma to 3772Ma, recording apparent crystallisation events at 1.2Ga, 1.8Ga and 2.7-2.8Ga, consistent with results from previous studies. Of 134 analyses made at EIMF, 104 (78%) were free from irregularities and less than 5% discordant. Each of the significant peaks in crystallisation ages corresponds with the growth and stabilisation of supercontinents (Rodinia, Nuna and Superia, respectively). Such correspondence could therefore indicate preferential preservation instead of increased crystallisation.

Hf model ages fall into four main episodes of melt extraction: c. 1.7Ga, 2.2Ga, 3.3Ga and 4.0Ga. Each of these events is described by zircons plotting along lines with ‘average crustal’ $^{176}\text{Lu}/^{177}\text{Hf}$ ratios of 0.015. There is considerable overlap between samples, indicating the Laurentian craton experienced multiple cycles of zircon crystallisation and sedimentary recycling over a large area to concentrate resistant detrital material into the sampled Neoproterozoic and Cambrian sedimentary units.

Combining all three measurements creates a more complete picture (Fig. 2). The large number of zircons in each crystallisation episode provides clear evidence of mixing between juvenile melts, particularly when filtered by the oxygen data. The majority of analyses delineating extraction events fall between mantle ($5.3\pm 0.6\%$) and basaltic ($<6.5\%$) oxygen values. Zircons growing during observed crystallisation events preserve a range of ϵHf_t values, suggesting mixing of juvenile melts with pre-existing crustal material. The presence of analyses with elevated ($>6.5\%$) oxygen values indicates interaction with sedimentary material at the time of juvenile melt formation.

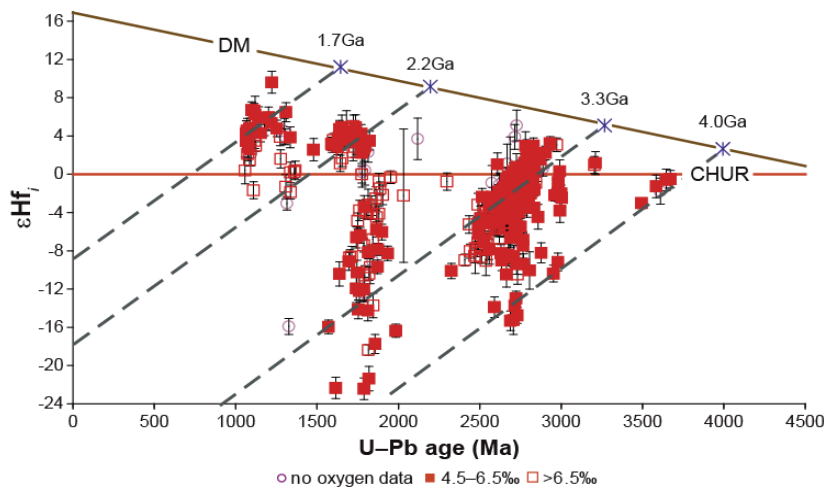


Figure 2. ϵHf_t vs. U–Pb zircon crystallisation age across north-west Scotland, sorted by oxygen values. Filled squares - oxygen in mantle to basaltic range. Open squares - elevated oxygen values, suggesting crustal contamination. Circles - no oxygen.

Summary

The first detrital zircon ϵHf_t analyses from the greater Laurentian region indicate four main episodes of juvenile crustal extraction, separated by 0.5-0.8Ga, and that the new crust had a granitic composition. Three significant crystallisation episodes follow the youngest extraction events, lagging by ~ 0.4 Ga and coinciding with supercontinent stabilisation.

References

- [1] Cherniak, D.J. and Watson, E.B. (2003) Reviews in Mineralogy and Geochemistry **53**, 113-44
- [2] Kemp, A.I.S. et al. (2006) Nature, **439**, 580-3
- [3] Pietranik, A.B. et al. (2008) Geology, **36**, 875-8
- [4] Zeh, A. et al. (2008). Geochimica et Cosmochimica Acta **72**, 5304-29
- [5] Whitehouse, M.J. et al. (1997) Terra Nova, **9**, 260-3
- [6] Rainbird, R.H. et al. (2001) Journal of the Geological Society of London, **158**, 15-27
- [7] Kinnaird, T.C. et al. (2007) Journal of the Geological Society of London, **164**, 541-51
- [8] Kirkland, C.L. et al. (2008) Precambrian Research, **163**, 332–50
- [9] Krabbendam, M. et al. (2008) Journal of the Geological Society of London, **165**, 379-94

Understanding the mechanisms of gas loss at persistently degassing basaltic volcanoes

P. Lesne, J. Blundy, F. Witham, S.C. Kohn

University of Bristol, School of Earth Sciences, Wills Memorial Building, Queens Road, Bristol BS8 1RJ, UK

Introduction

Water and CO₂ are the main volatiles involved in basaltic magma degassing. They control physical and chemical properties of silicate liquids (e.g. viscosity, density), and therefore control the eruptive dynamics. Studying the behaviour of magmatic volatiles is of utmost importance to understand degassing process and therefore to forecast major eruptions. However, the influence of other volatile species such as S and Cl on volatile phase relations is yet unknown.

For the first time, a H-C-O-S-Cl fluid phase has been equilibrated experimentally with basaltic melts in order to study the degassing of two basaltic systems (Stromboli, Italy, and Masaya, Nicaragua). Experiments were performed at supraliquidus temperature (1150 °C), pressures of 25 to 400 MPa and oxygen fugacity ~1 log unit above the NNO buffer. The aim of the study was to produce fluid-melt partition coefficients of different magmatic volatiles, in order to track the evolution of the melt and the fluid phase in equilibrium from the magma chamber to the near surface. As it is very difficult to measure directly the composition of coexisting vapour, we measured accurately the volatiles dissolved in melt, in order to determine precisely the fluid phase composition by mass balance calculation.

Different techniques have been developed to measure H₂O and CO₂ dissolved in melt, including both destructive (i.e., Karl-Fischer Titration, LECO) and non-destructive techniques (i.e., Raman, FTIR). These are well-established, reliable techniques. However, large amount of material are needed for the destructive techniques, whereas well-constrained calibration parameters (e.g. extinction coefficients for FTIR) are needed for the non-destructive techniques. The ionprobe affords a high spatial-resolution, low-damage technique for analysis of volatiles in experimental run products, provided only that calibration standards are available.

Secondary ion mass spectrometry (SIMS)

SIMS was applied only to those experimental glasses whose H₂O and CO₂ concentrations were below detection by FTIR. In addition we analysed several glasses by SIMS that had also been analysed by FTIR to evaluate the consistency of the two techniques. Analytical techniques are described in the appendix.

To calibrate H₂O and CO₂ we followed the method of [1], by analyzing basaltic glass standards with known H₂O and CO₂ contents, and by building working curves of ¹H/³⁰Si versus H₂O (Figure 1) and ¹²C/³⁰Si versus CO₂ (Figure 2). A total of 7 basaltic glass standards for H₂O, and 5 basaltic glass standards for CO₂ were run, covering a range of 0.15 to 4.6 wt% H₂O and 0 to 1000 ppm CO₂. Calibration was performed afresh on each analysis day and uncertainties on the working curve were propagated through to calculate uncertainty on dissolved H₂O and CO₂.

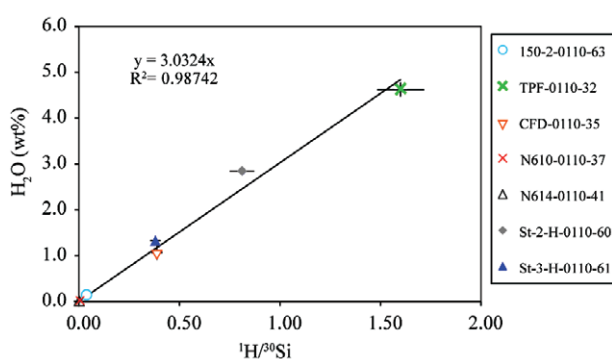


Figure 1. Working curve calibrated for basaltic melts using ¹H/³⁰Si ratios of seven basaltic glass standards.

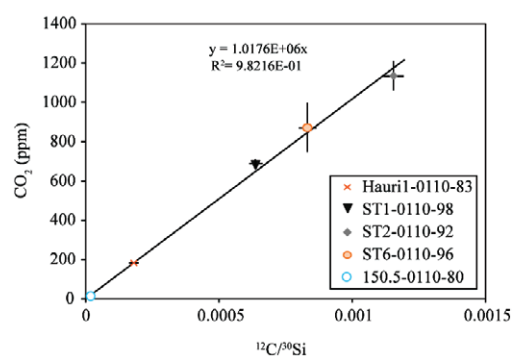


Figure 2. Working curve calibrated for basaltic melts using ¹²C/³⁰Si ratios of five basaltic glass standards.

For glasses analysed by both SIMS and FTIR we observed a consistent offset in H₂O contents, with FTIR giving values 18.5% relative higher than SIMS (Figure 3). We attribute this difference to uncertainty in the FTIR absorption coefficients, which are very sensitive to bulk composition. This affects accuracy rather than precision. As SIMS analysis of H₂O is less compositionally-sensitive than FTIR, and given that SIMS analyses of the most H₂O-rich experimental glasses give better overall agreement to the initial H₂O content as determined by KFT, we have reduced *all* FTIR H₂O data by a factor of 1.185 (see [3]). For CO₂ agreement between SIMS and FTIR showed no such offset (Figure 4), suggesting that the absorption coefficients of [2] are well-suited to our glass compositions. Consequently no correction was made to FTIR CO₂ data.

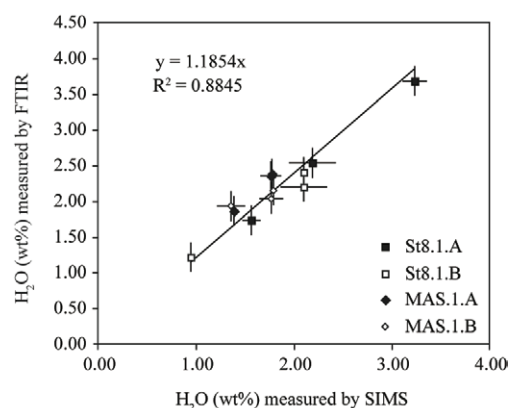


Figure 4. Comparison of H₂O contents of experimental glasses measured by both FTIR and SIMS. Deviation from a 1:1 line is attributed to uncertainty in the extinction coefficient used for processing FTIR data. A correction factor of 1.1854 has been applied to all of the FTIR data to bring them into line with SIMS. No such correction was required for CO₂ data.

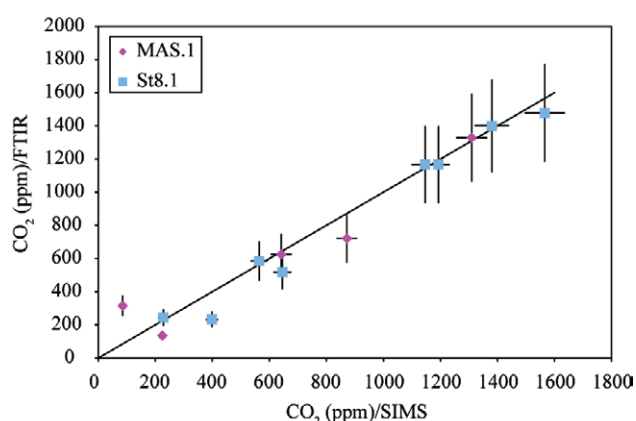


Figure 3. Comparison of CO₂ contents of experimental glasses measured by both FTIR and SIMS. Deviation from a 1:1 line is attributed to uncertainty in the extinction coefficient used for processing FTIR data.

Using the Cameca IMS-4f ion microprobe at the University of Edinburgh allowed us to obtain accurate data on the major volatiles H₂O and CO₂. These data have been combined with electron-microprobe data for S and Cl in order to derive fluid-melt partition coefficients. These data have been used to develop a numerical model of degassing of magmas in the system basalt-H₂O-CO₂-S-Cl [3].

References

- [1] J. Blundy and K. Cashman (2008) *Reviews in Mineralogy and Geochemistry* **69**, 179-239
- [2] G. Fine & E. Stolper (1986) *Earth and Planetary Science Letters* **76**, 263-278
- [3] P. Lesne, S.C. Kohn, J. Blundy, F. Witham, R.E. Botcharnikov & H. Behrens (2011) *Journal of Petrology* (accepted for publication)

Disentangling environmental and physiological influences on otolith growth: unlocking the potential use of otoliths as natural tags

A. Lewis^{1,2}, C. Trueman¹, and E. Hunter²

¹ National Oceanography Centre, University of Southampton, Waterfront Campus, Southampton SO14 3ZH, UK
² Centre for the Environment, Fisheries & Aquaculture Science, Pakefield Road, Lowestoft NR33 0HT, UK

Background

Despite its potential value as a recorder of the environmental history of individual fish, “otolith chemistry” (minor/trace metal concentrations and $\delta^{18}\text{O}$) is not well understood, with little *in situ* validation and the effects of physiology remaining largely unknown. This project aims to address both issues by 1) coupling ground tracks of wild marine fish (*Pleuronectes platessa*) recorded by electronic Data Storage Tags (DSTs) with chemical profiles across otoliths of the same fish and 2) tracking otolith chemistry alongside blood chemistry and physiological variables in mature and immature fish maintained over an entire reproductive cycle. To address either objective, an accurate identification of the timing of otolith deposition is crucial. As such, we have been measuring $\delta^{18}\text{O}$ at $\sim 20\mu\text{m}$ resolution on the otoliths of experimental and wild plaice to synchronise otolith growth with known water temperature records and provide a timescale within otoliths. We have also been measuring Ca, Sr, Mg, K, Ba and Li concentrations at $\sim 8\mu\text{m}$ resolution in a subset of otoliths from wild fish to examine pre-DST chemical histories. Analyses are ongoing, but preliminary results are promising and the full dataset will be reported in next year’s report.

Results - trace metal data (Cameca 4f)

All otoliths exhibited fluctuations in element concentrations that tended to increase in amplitude with age, particularly for Sr. This may be due to increasing migratory behaviour exposing individuals to a wider range of environments and/or ontogenetic changes in physiology. Interpretation of these data will be aided by future SIMS analyses in which we will measure trace metal concentrations across the experimental portion of the otoliths. We will also carry out parallel LA-ICPMS transects at NOC to examine correspondence between the two techniques. For two wild fish, Sr concentrations were measured by SIMS that had previously been analysed by LA-ICPMS (using the same portion of the alternative otolith, Fig. 1) (A. Darnaude, Université Montpellier 2, unpubl.). Generally there was good correspondence among techniques ($r^2 > 0.8$), however, SIMS had far superior spatial resolution.

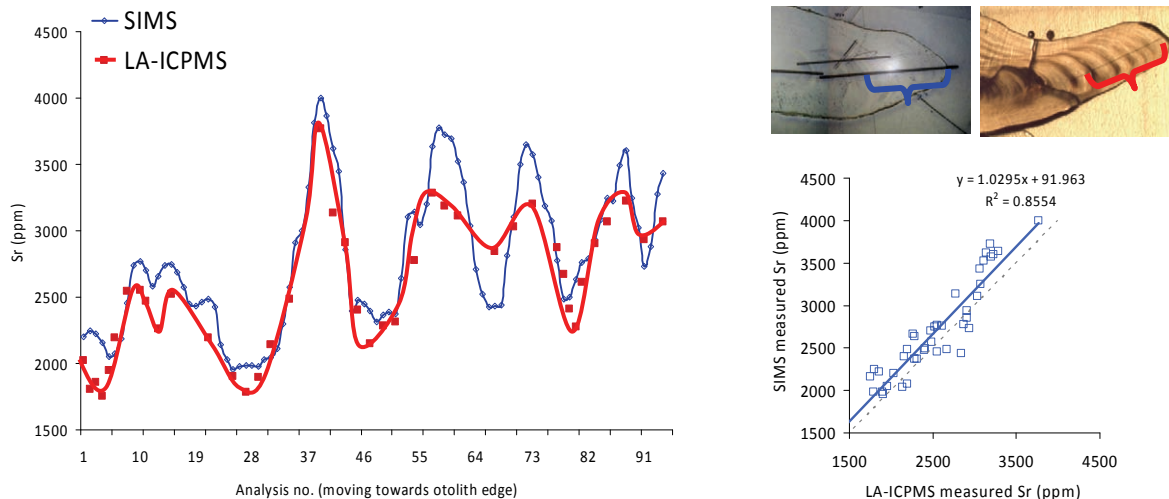


Fig. 1 Otolith Sr profiles for the last 6 years of life for a DST tagged plaice. SIMS analyses were carried out on the asymmetric otolith (thin blue line; left image) while LA-ICPMS analyses were carried out on the symmetrical otolith (thick red line; right image) (A. Darnaude & E. Hunter, CEFAS). The inset graph shows the relationship between the two datasets (blue line) with the 1:1 line displayed as a grey dotted line

Results - $\delta^{18}\text{O}$ data (Cameca 1270): Experimental fish

The predicted $\delta^{18}\text{O}$ values (Fig. 2) indicated that otolith $\delta^{18}\text{O}$ of the experimental fish should reach a maximum between January and late March 2010, coinciding directly with the spawning period.

The shape of the measured otolith $\delta^{18}\text{O}$ profiles generally corresponded to the predicted profile (Fig. 2 & 3), providing a solid basis for identifying timelines within each otolith. There was considerable variation in otolith growth rate among seasons and individuals, highlighting the necessity of this work to time match otolith trace metal concentrations with blood samples and physiological measurements.

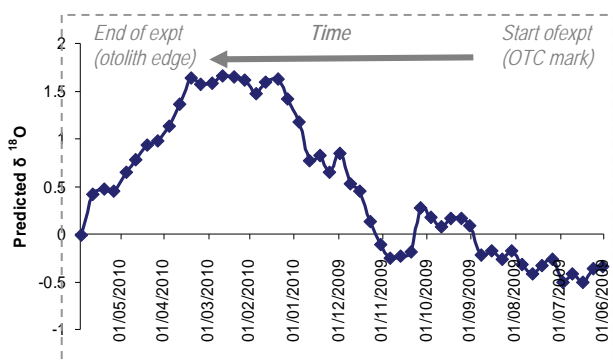


Fig. 2 Predicted $\delta^{18}\text{O}$ data for experimental plaice maintained at the CEFAS aquarium for 12 months from June 2009. The prediction is based on an equation derived from experimental work with juvenile North Sea cod (*I.*). In all figures in this report, the dotted line box indicates the period of interest (aquarium or DST experiment) and the shaded boxes indicate inferred seasons (summer: orange, winter: blue).

While profiles were generally comparable, there were often differences between measured and predicted values. It has yet to be determined whether these differences are real, an artefact of sample-standard matrix differences, or an issue with the prediction equation, which is derived from experimental work on juvenile cod so has potential for interspecific or ontogenetic cross-over issues.

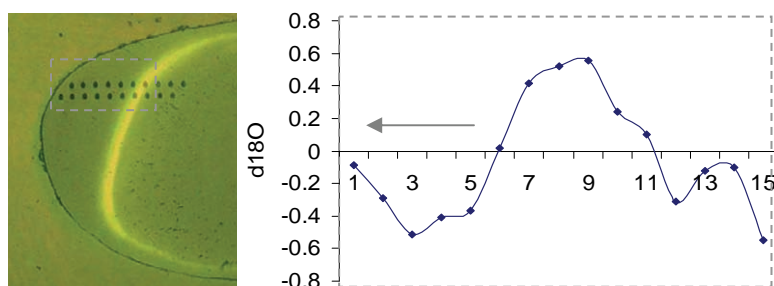


Fig. 3 $\delta^{18}\text{O}$ profile for a female plaice maintained at CEFAS for 12 months. The photograph shows the otolith pit marks and the OTC (yellow) mark indicates the experiment start point. The graph shows $\delta^{18}\text{O}$ values for the experimental period. The arrow indicates particularly fast growth post-spawning.

Results - $\delta^{18}\text{O}$ data (Cameca 1270): Wild fish

Measured otolith $\delta^{18}\text{O}$ exhibited clear seasonal fluctuations in the wild fish, allowing a basic timeline to be attributed to the period of interest through wiggle matching with predicted $\delta^{18}\text{O}$ values. In the example shown in Figure 4 there was considerable slowing of growth during the winter spawning season that would have been difficult or impossible to identify using visual banding alone.

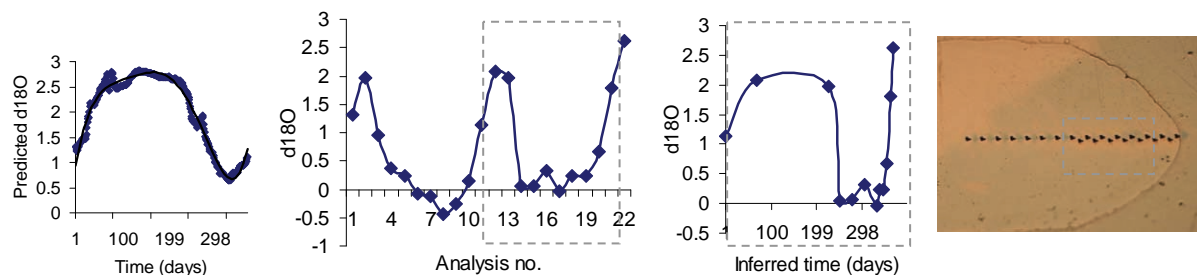


Fig. 4 $\delta^{18}\text{O}$ profiles for a female plaice tagged by DST (pit marks shown in photograph). The predicted $\delta^{18}\text{O}$ profile (left) is based on the DST-recorded temperature for this fish and an assumed constant salinity of 35 PSU. This predicted profile was used to modify the x-axis of the measured profile (centre) to give an inferred timeline for the experimental period (right). Note that unlike Figures 2 & 3, time is displayed from left to right.

References

1. H. Hoie et al. (2004) ICES Journal of Marine Science: Journal du Conseil **61**, 243.

The effects of metamorphic overprinting on zircon

J.M. MacDonald¹, J. Wheeler¹, S.L. Harley², Q.C. Crowley³, K.M. Goodenough⁴ & E. Mariani¹

¹School of Environmental Sciences, University of Liverpool, Liverpool L69 3GP, UK

²School of GeoSciences, University of Edinburgh, Edinburgh EH9 3JW, UK

³School of Natural Sciences, Trinity College, Dublin, IRL

⁴British Geological Survey, Edinburgh EH9 3LA, UK

Background and aim

In principle the temperature-time history of a high-grade metamorphic complex, and origins of its constituent precursor rocks, can be evaluated from U-Pb isotopic and Ti [1] and REE abundance data obtained from zircon grown before or during metamorphism or modified by the recrystallisation and fluid-activated processes operating during and after metamorphic events. However, interpretations of thermal evolution and crustal history based on zircon can be complicated by the presence of multiple metamorphic events, each of which may partially and variably ‘overprint’ pre-existing chemical signatures that could otherwise be used to link zircon ages to temperature and process.

In order to evaluate the impact of multiple metamorphic events on the chemical records retained in zircon this study has examined in detail zircons from rocks which have undergone polymetamorphism at varying temperatures and pressures. Samples from the Lewisian Gneiss Complex (LGC) of northwest Scotland, considered to have been formed as granite-like rocks in the lower continental crust and subsequently metamorphosed and deformed several times, have been selected based on detailed field mapping of deformation zones. Zircons from the selected samples have been imaged with Cathode Luminescence (CL) [2] and their crystal lattice distortions characterised using Electron Backscatter Diffraction (EBSD) [3]. U-Pb radiometric dating was conducted on the Cameca 1270 while the net abundances of REEs, Ti, Y, Ba and Hf were measured on the Cameca 4f. Plesovice and 91500 zircons along with NIST SRM-610 glass were used as analytical standards. Analytical procedures are those of [4].

Results and interpretation

The primary aim of the ion microprobe analysis was to determine the effects of overprinting in rocks with varying temperature and deformation histories by examination of similarities and differences in zircon chemical signatures and ages, linked to texture and mineral setting. In particular, we have compared zircon characteristics in those rocks that are ‘weakly deformed’ (these retain mineral layering) with those in ‘strongly deformed’ rocks in which a strong crystal alignment is evident. This process-related aim also yields new insights into the evolution of the LGC. Here we give a brief overview whilst detailed analysis of data is still ongoing.

Generic aspects of zircon behaviour

- The differences in average REE abundance in zircons between strongly- and weakly- deformed rocks are negligible, suggesting that high-T deformation has little effect on zircon REE chemistry at any chosen site. Though they have similar shapes, REE patterns *do* vary from site to site (Fig. A1).
- The preliminary EBSD analysis detected a few zircon crystals which had distorted (bent) crystal lattices. The ²⁰⁷Pb/²⁰⁶Pb ages calculated for the distorted zircons were younger than those from undistorted zircons from the same sample. This indicates that distortion of the crystal lattice facilitates escape of Pb (Fig. 1a). Figure 1b shows how the timing of crystal lattice distortion can be deduced through combining zircon U-Pb age information from the distorted zircons with those from undistorted zircons in the same sample. In the age of this distortion (the lower intercept on the plot) is within error of a previously published age for a metamorphic event occurring in the LGC [5].
- Zircon Ti abundances in distorted zircon grains show considerable variability, with unusually high concentrations of Ti in two cases. This indicates some uptake of Ti ions by the distorted zircon lattice. If this is the case then the calculated minimum temperature of these zircons (900°C) is not reliable.
- Ti contents of zircons that yield differing U-Pb ages suggest their repeated recrystallization or modification at temperatures of at least 760°C (Figure 2); CL zoning features indicative of partial zircon recrystallization are prevalent, along with occasional instances of new-growth textures. This appears to support an interpretation of LGC deep continental crust residency for a period of ~350Ma.

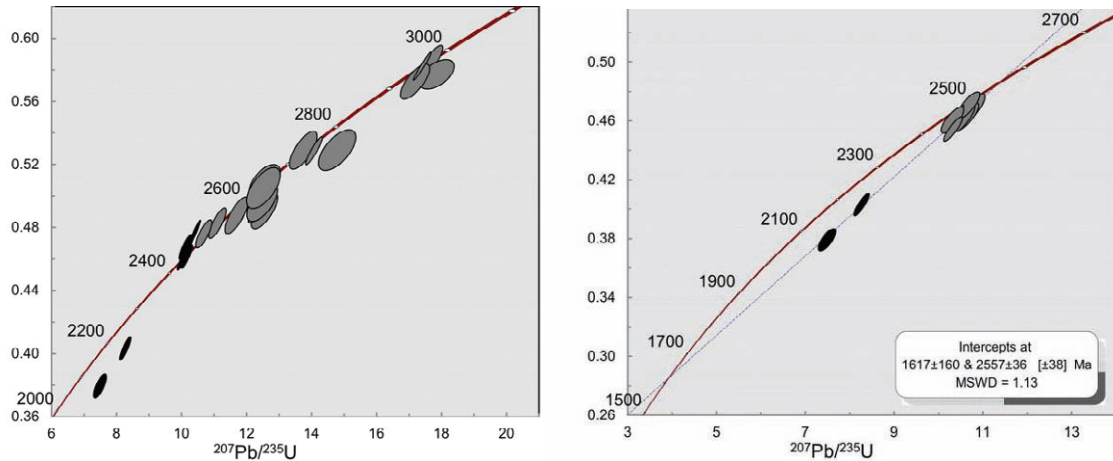


Fig. 1 A) (left) Concordia plot (Isoplot v3.0) showing data points from undeformed (grey) and deformed (black) zircons; B) (right) Concordia plot of zircon data from one sample with a Discordia line plotted through deformed zircon data points; the lower intercept age is interpreted to be the age of the zircon lattice deformation

Implications for Lewisian Gneiss Complex

Previous work has suggested the presence of a distinct metamorphic event at ~2750Ma followed by a slightly lower temperature event at ~2490Ma [6]. However, LGC age data plotted against minimum temperature as determined from zircon Ti contents (Figure 2) fails to show any distinct event at ~2730Ma. It is proposed that the zircons and their host rocks remained deep in the continental crust at a temperature of >760°C from their formation at ~2850Ma until uplift at ~2480Ma.

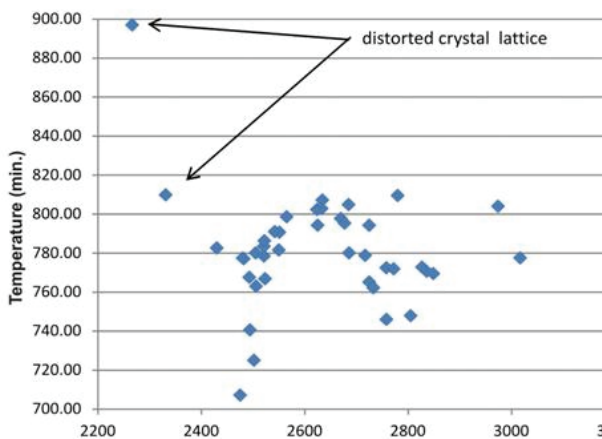


Fig. 2 Graph of Ti-in-zircon thermometer temperatures (which are *minima*) and carefully selected $^{207}\text{Pb}/^{206}\text{Pb}$ ages from a zircon population. Each blue diamond represents one analytical spot. We consider it extremely unlikely that the LGC was cooled and reheated multiple times to create the graph of Fig. 3. A far simpler explanation is that the zircons and their host rocks remained in a stable high temperature environment in the Earth's crust for this long period of time.

Conclusions

Our data indicate that whilst REEs in zircon are unresponsive to deformation, lattice distortions can cause Pb mobility and resetting and hence allow that deformation to be dated. It appears likely from zircon Ti / age data that the LGC remained at granulite facies temperatures for 350 Ma. In contrast to the evolution of mountain belts in the Phanerozoic, which evolve quickly, these rocks appear to have remained in a hot yet stable tectonic setting following their formation.

References

- [1] E.B. Watson et al (2006) Contributions to Mineralogy and Petrology **151**, 413-433
- [2] F. Corfu et al. (2003) Reviews in Mineralogy and Geochemistry **53**, 469-500
- [3] D.J. Prior et al. (1999) American Mineralogist **84**, 1741-1759
- [4] N.M. Kelly and S.L. Harley (2005) Contributions to Mineralogy and Petrology **149**, 57-84
- [5] P.D. Kinny et al. (2005) Journal of the Geological Society of London **162**, 175-186
- [6] G.J. Love et al. (2004) Contributions to Mineralogy and Petrology **146**, 620-636

Origins of large volume ignimbrites from the Taupo Volcanic Zone, New Zealand

N. Matthews¹, D.M Pyle¹ & C.J.N. Wilson²

¹Department of Earth Sciences, University of Oxford, Oxford OX1 3AN, UK

²School of Geography, Environment and Earth Sciences, Victoria University, Wellington 6040, New Zealand

Introduction

The Taupo Volcanic Zone (TVZ) is one of the most active zones of rhyolitic volcanism in the world, and the location of several super-eruptions (>500 km³ of magma [1]) over the past 2 Ma. It is an ideal place to test models of how large volumes of silicic magma are assembled prior to eruption. This project focused on SIMS analysis (by Cameca 1270-IMS) of $\delta^{18}\text{O}$ of zircon, quartz and feldspar from single pumice clasts from the Whakamaru² group ignimbrites (>1500 km³; Fig. 1). The data will be modeled and interpreted in terms of the broader framework provided by other microanalytical techniques (U-Pb ages and trace elements by SHRIMP-RG; glass chemistry by EPMA and LA-ICP-MS; Ti-in-quartz mapping by synchrotron micro-XRF) to quantify the evolutionary history of the silicic chamber prior to eruption.

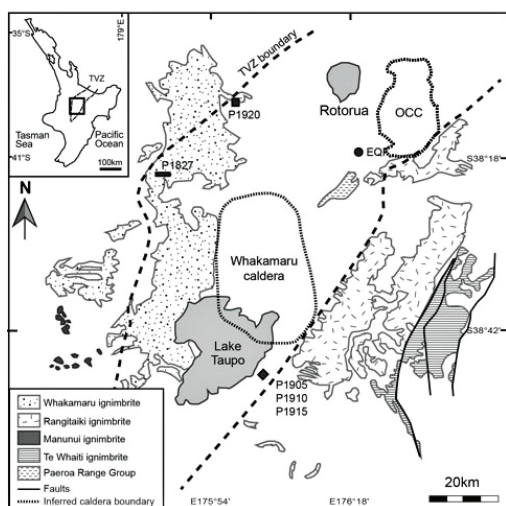


Fig.1: Whakamaru ignimbrite distribution; inset TVZ, North Island, New Zealand. Inferred Whakamaru caldera boundary outlined by dashed black line; OCC refers to the Okataina Caldera Complex.; Sample localities and sample codes are marked: P1905, P1910 and P1915 are Rangitaiki pumices, P1920 and P1827 are Whakamaru.

Background to the Whakamaru super-eruption

The central TVZ is a zone of prolific silicic volcanism in a rifting continental arc. The Whakamaru super-eruption deposits are the main products of a pulse of volcanism at 340 ka following a c. 350 ka hiatus in caldera-forming activity [2]. With a volume of >1500 km³ (Fig. 1), it is the largest known eruption in TVZ history. The physical and chemical complexities of the deposits hold critical information about how supervolcanoes develop and their

mechanisms of eruption. Earlier work has illustrated the complexity of chemical variation between eruption units, and indicates that the eruption involved five distinct magma batches (Fig. 2).

Objectives

The aims of this research were to determine whether the mineral phases grew together from the same batch(es) of pre-eruptive magma; and to identify the sources contributing to magma

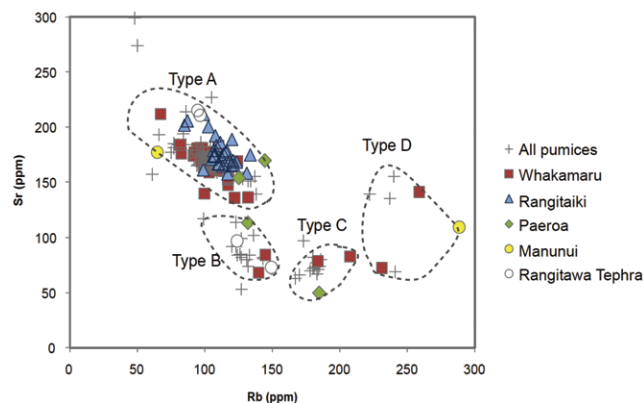


Fig. 2: Trace element variation in Whakamaru pumices (whole-rock XRF data), showing chemical variation within and between ignimbrite units– indicating four discrete magma batches (type A-D).

genesis and the degree to which magma was homogenized prior to eruption. Comparisons will be drawn with other large-volume silicic systems (e.g. Yellowstone) to test whether these eruptions followed a similar pattern of pre-eruption development. There have been no recent investigations of O-isotope signatures in TVZ rhyolites at the mineral scale. Our results provide a significant test of the hypothesis that rhyolite genesis in TVZ involves protracted crystallisation of basalts coupled with limited assimilation of crustal rocks.

Results

A summary of $\delta^{18}\text{O}$ results is provided in Fig. 3. For quartz, we find that cores, mid-sections and rims show no systematic patterns of $\delta^{18}\text{O}$ variation within any particular sample. Intra-sample variation of $\delta^{18}\text{O}(\text{quartz})$ is significantly larger than that for zircon, and the quartz-zircon fractionation varies between samples. There is little evidence for the extreme variations in pre-eruption $\delta^{18}\text{O}$ observed at Yellowstone, for example [3]. Indeed, our new analyses of zircon from Yellowstone's Huckleberry Ridge Tuff also suggest that most zircons are homogenous in $\delta^{18}\text{O}$ within error (Fig. A4).

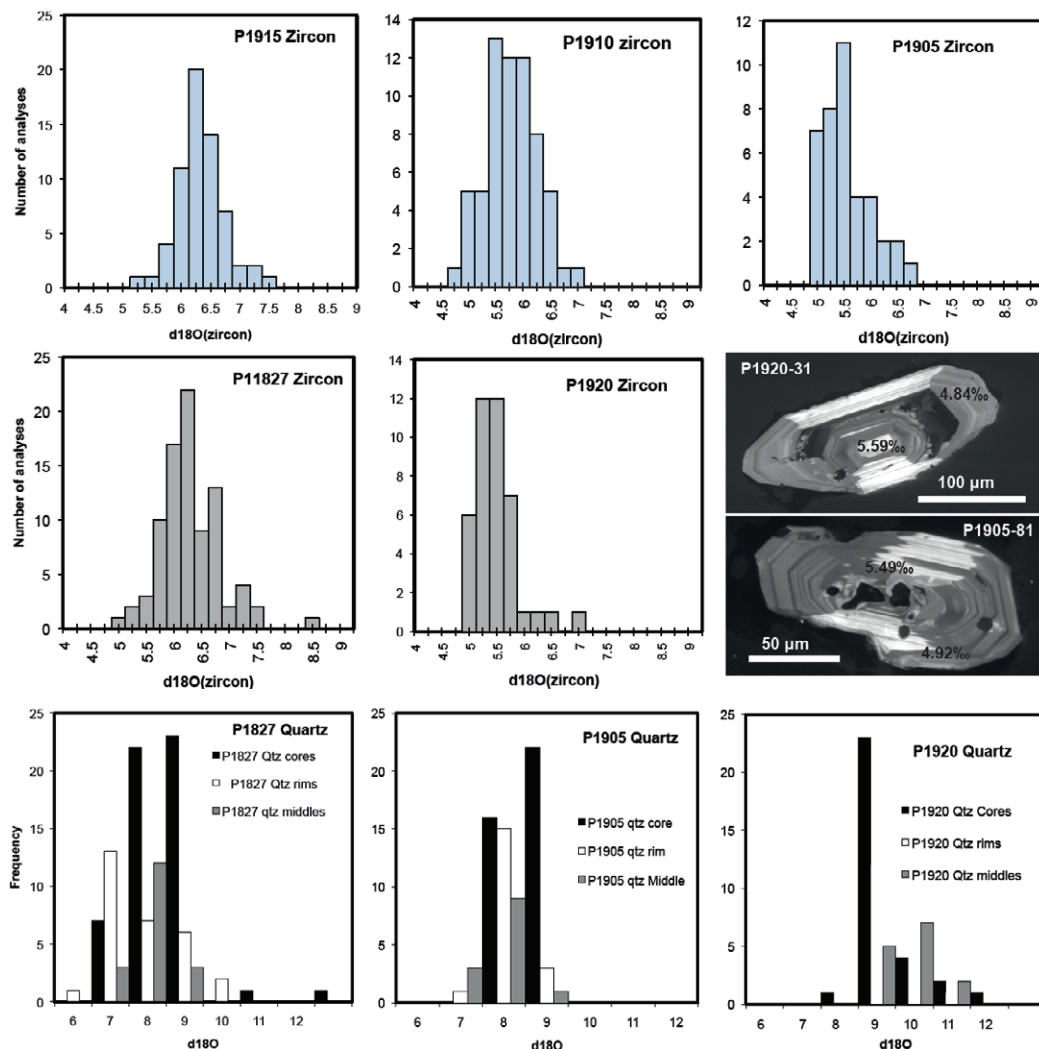


Fig. 3: $\delta^{18}\text{O}$ variation for zircon and quartz extracted from single Whakamaru pumice clasts (including core, mid and rim analyses). CL images show two zircon crystal extracted from pumice samples P1920 and P1905, with cores of 5.59‰ and 5.49‰ and rims of 4.94‰ and 4.92‰ respectively ($\pm 0.3\text{‰}$).

Discussion

$\delta^{18}\text{O}$ data for dated zircons, in addition to quartz and feldspar crystals extracted from the same pumice clasts, illustrate that co-erupted mineral phases did not all crystallise together in isotopic equilibrium, suggesting that multiple magma sources were entrained by the eruption. Variability between crystal cores and rims is inconsistent, suggesting complex pre-eruptive mixing and partial homogenization processes in the large silicic reservoir. These observations are consistent with our developing model of rapid pre-eruptive heating and rejuvenation of the magmatic system, based on mineral thermobarometry. We are currently completing our modeling and interpretation of these data as part of our U-Pb geochronology work on the same samples (at the joint USGS-Stanford SHRIMP-RG facility).

References

- [1] C.J.N. Wilson, et al. (1995) *Journal of Volcanology and Geothermal Research* **68**, 1-28
- [2] S.J.A. Brown et al. (1998) *Journal of Volcanology and Geothermal Research* **84**, 1-37
- [3] I.N. Bindeman and J.W. Valley (2001) *Journal of Petrology* **42**, 1491-157

The preservation of magmatic processes in the isotopic and trace element stratigraphy of zircon and apatite

Andrew Miles¹, Colin Graham¹, Martin Gillespie², Chris Hawkesworth³ and Richard Hinton¹

¹School of GeoSciences, West Mains Road, University of Edinburgh Edinburgh, EH9 3JW, UK

²British Geological Survey Murchison House, West Mains Road, Edinburgh, EH9 3LA, UK

³School of Geography and Geosciences, University of St Andrews, North Street, St Andrews, KY16 9AL, UK

Introduction

Our ability to document the evolution of Earth's continents has been fundamentally enhanced by modern developments in the microanalysis of the robust geochemical stratigraphy of accessory minerals such as zircon (e.g. [1]). As a dominant constituent of the upper continental crust, granites and their abundant accessory minerals provide a representative record of the wider processes that govern the crust's role as a global geochemical reservoir and preserve a record of its preservation potential in different tectonic regimes.

This study aims to exploit the ability of zircon to preserve a robust record of the magma sources involved in the formation of post Caledonian, 400Ma Scottish granites. Oxygen isotopes, measured using the Cameca ims 1270, have been used in conjunction with Hf isotopes (measured by LA-ICP-MS at the University of Bristol) to assess the varying roles of crust and mantle components in the magmatic evolution of geochemically zoned plutons. Further assessment of granite sources has been made by zircon U-Pb dating using the Cameca ims 1270, while zircon trace element compositions have been measured using the Cameca ims 4f. A new method has also been developed to test the timing of zircon formation using apatite compositions as a proxy for the relative timing of crystallization of different phases.

Results

Zircon oxygen isotope compositions were measured from the outer and least evolved to the inner and most evolved zones of the Criffel pluton. Oxygen isotope values ($\delta^{18}\text{O}$) increase systematically from $<6\text{‰}$ to $>9\text{‰}$, with increasingly wide distribution profiles signifying increasing ranges in melt compositions with distance from the pluton margin (Fig. 1). The oxygen isotope compositions of the melts from which zircon crystallised have been calculated and compared to those of the whole rock (carried out at SUERC). The latter show good evidence of correlations with other indices of magma differentiation and are thus assumed to be the result of magmatic processes. Disequilibrium between measured whole rock $\delta^{18}\text{O}$ and melt $\delta^{18}\text{O}$ calculated from zircon $\delta^{18}\text{O}$ compositions indicates early zircon crystallisation.

U-Pb dating has confirmed textural evidence that these zircons are primary and of magmatic origin, consistent with the work of [2]. The large number of zircons with very similar ages has enabled a closer examination of the matrix effects of zircon U and Th concentrations on the calculated U-Pb ages of zircons analysed using SIMS more generally. An apparent correlation has been found between the calculated age and U and Th concentrations below the threshold concentrations previously assumed. A linear correction to U-Pb ages is therefore suggested for all zircon U-Pb analyses, including those below the currently accepted threshold value of $\sim 2500\text{ppm}$ [3]. Preliminary results suggest that the new correction for zircons from the Criffel pluton with U and Th concentrations of $\sim 300\text{-}500\text{ppm}$ can lead to an overestimate of $\sim 4\text{-}5$ Ma in the calculated U-Pb age.

Despite the ability of zircon to record and preserve magmatic compositions, its timing of crystallisation relative to other phases remains poorly constrained. Textural evidence from other studies has been used to suggest both late and early zircon crystallization (e.g. [4]). Apatite inclusions occur within almost all minerals in the Criffel granite, including zircon, indicating that it crystallised continuously throughout the evolution of these granitic magmas. Apatite also shows greater sensitivity than zircon to changing melt compositions, particularly in terms of its F and trace element compositions [5]. Cameca ims 4f analyses of apatite crystals have been compared with analyses made on a Cameca SX100 electron microprobe at the University of Edinburgh. The data reveal that apatite hosted by zircon is consistently the most primitive (F-depleted) and therefore earliest to crystallise relative to those hosted by other phases.

A relative order of crystallization has therefore been developed that is independent of - but complementary to - textural evidence. This inclusion study therefore provides a new method whereby

the timing of zircon crystallisation can be tested, enabling subsequent O and Hf analyses to be better assessed in the context of magma evolution.

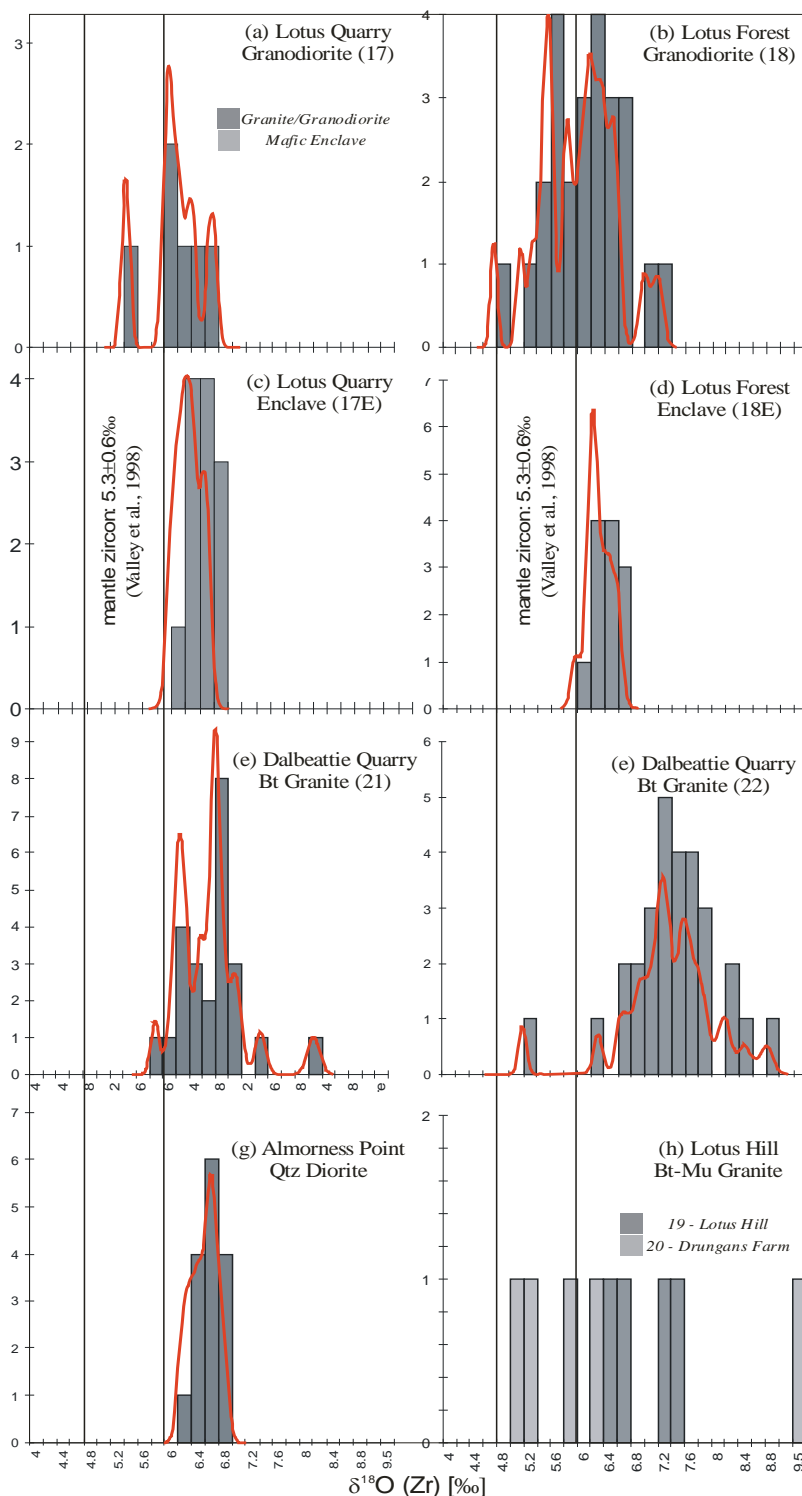


Fig. 1 Zircon oxygen isotope compositions for the outer- to inner-most zones 1 (sample 17), 2 (sample 18), 3 (sample 21), 4 (sample 22) and 5 (samples 19 and 20). Mean oxygen isotope compositions increase systematically from outer to inner zones, with an increase in the width of the associated probability distribution. Also shown are the oxygen isotope compositions of zircons from two mafic enclaves from zones 1 and 2 (17E and 18E respectively) and the marginal quartz diorite.

References

- [1] Hawkesworth et al. (2010) *Journal of the Geological Society* **167**, 229-248.
- [2] Pigeon and Aftalion (1978) *Geological Journal Special Issues* 183-220.
- [3] McLaren et al. (1994) *Geochemica et Cosmochemica Acta* **58**, 993-1005.
- [4] Darling et al. (2009) *Geology* **37**, 927-930.
- [5] Sha and Cahppell (1999) *Geochemica et Cosmochemica Acta* **63**, 3861-3881.

Oxygen isotope studies of serpentine in kimberlite

R. H. Mitchell

Department of Geology, Lakehead University, Thunder Bay, Ontario, Canada P7B 5E1

Introduction

Although serpentine is a ubiquitous mineral in hypabyssal and diatreme zone kimberlites, its origin remains controversial. Some petrologists claim that all serpentine is secondary and produced by the introduction of externally-derived fluids into the kimberlite. In contrast, others [1] suggest, on the basis of detailed mineralogical studies, that serpentine is a primary mineral formed mainly from deuteritic fluids. To date the only investigations of the isotopic composition of kimberlite serpentine have been by bulk analysis of samples that have undergone subaerial alteration, and hence undoubtedly interacted with meteoric water. Consequently, as previous studies have failed to resolve the serpentine genetic problem, an investigation of the isotopic composition of oxygen in kimberlite serpentine using the Edinburgh ion probe facility was instigated.

Serpentine in kimberlite

Serpentine and chlorite in kimberlites occurs as: (1) pseudomorphic retrograde lizardite and chlorite after primary olivine (2) late stage primary serpophitic serpentine; (3) prograde serpophitic serpentine replacing retrograde lizardite; (4) chlorite replacing interclast phlogopite in diatreme zone rocks. Textural/mineralogical relationships indicate that retrograde lizardite is derived from hydrous deuteritic fluids. Serpophitic or polygonal serpentine is a primary low temperature phase that common forms monomineralic segregations in the groundmass of hypabyssal kimberlites. Experimental studies have shown that polygonal serpentine can form from Mg-Si gels at low temperatures (300°C). In this study all paragenetic types of serpentine and chlorite have been analysed.

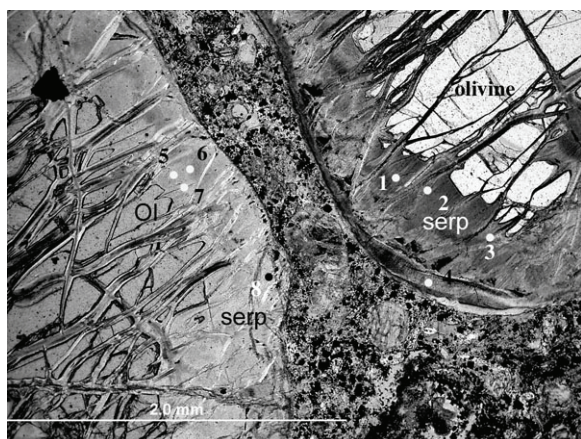


Fig. 1 Retrograde pseudomorphic serpentine.

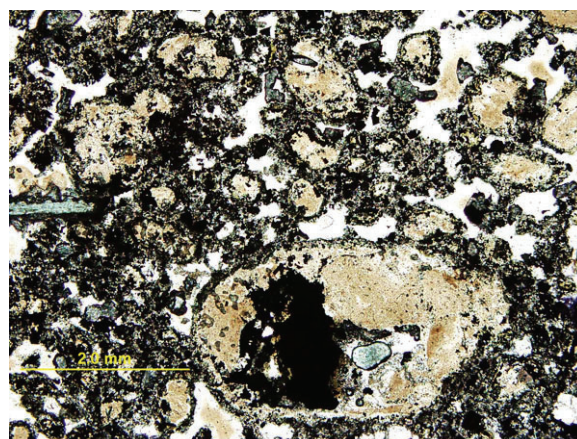


Fig. 2 Serpophitic segregatory serpentine (white).

Results

The oxygen isotopic composition of all varieties of serpentine was determined in hypabyssal and diatreme facies kimberlites from Southern Africa, Canada and the USA. Data were acquired with the Cameca ims 1270 (#309) ion microprobe. The internal precision of each analysis is $< 0.2\text{‰}$, and the external precision, calculated from multiple analyses of the standard, that is assumed to be homogeneous, is estimated at $< 0.3\text{‰}$. The analytical standard used was a sample of antigorite (Royal Ontario Museum acquisition #M8571) whose bulk isotopic composition had been determined by standard fluorination methods at Queen's University (Kingston, Ontario) *i.e.* $\delta^{18}\text{O} = +8.8\text{‰}$, $\delta\text{D} = -63.5\text{‰}$. Secondary analytical controls included lizardite-1T (Royal Ontario Museum acquisition #M19804; $\delta^{18}\text{O} = +9.9\text{‰}$, $\delta\text{D} = -121.5\text{‰}$).

The analyses showed that in Iron Mountain hypabyssal kimberlites the $\delta^{18}\text{O}$ of pseudomorphic marginal and vein serpentine is similar and ranges between $+4.25$ and $+6.25\text{‰}$. For compositionally zoned pseudomorphic marginal serpentines $\delta^{18}\text{O}$ decreases from core-to-rim (cores 6.42 to 3.77‰

$\delta^{18}\text{O}$; rims 2.67 to 0.57‰ $\delta^{18}\text{O}$). Prograde pseudomorphic serpophite in the Ham West HW20 and HW11 kimberlites ranges in $\delta^{18}\text{O}$ from +4.14 to -0.50 ‰, with segregatory primary serpophite $\delta^{18}\text{O}$ ranging from +1.60 to -1.84‰. In diatreme zone rocks at Letseng-la-terae, the earliest pseudomorphic serpentines range in $\delta^{18}\text{O}$ from +5.03 to +3.49‰, later-forming rim and marginal serpentines from +4.34 to -1.77‰, with interclast serpophite from +3.41 to +1.47‰. At Kao, the earliest pseudomorphic serpentines are relatively uniform in composition and range in $\delta^{18}\text{O}$ from +4.94 to +4.50‰, later rim and marginal serpentines from +4.92 to +4.78‰, and interclast serpophite from +6.25 to +3.80‰.

Interpretation

These data show that the kimberlites investigated have not interacted with large volumes of light meteoric waters. Similar oxygen isotopic compositions in hypabyssal and diatreme zones rocks from different localities certainly preclude introduction of meteoritic water. The trends from mantle oxygen $\delta^{18}\text{O}$ to lighter oxygen are a result of either fluid compositional evolution or very minor introduction of light water. Figure 3 shows how the oxygen isotopic compositions of pseudomorphic serpentine might change as a function of water/serpentine ratios in open and closed systems. It is assumed that parental olivine has a primary $\delta^{18}\text{O}$ of about +6‰ and that this is reduced by ^{16}O enrichment due to reactions with isotopically lighter water. Figure 3 is based upon the serpentine-water fractionation factor ($\Delta^{18}\text{O}$) determined by Wenner & Taylor [2], and indicates that for serpentinization at 200-300°C in closed systems with initial water compositions ranging from -10 to -20‰, that “water/serpentine” ratios cannot exceed 0.8 at.%. These data are interpreted to suggest that there was not an influx of significant volumes of low temperature meteoric water as a cause of serpentinization. This conclusion is supported by the absence of extremely light oxygen (*i.e.* $^{18}\text{O} < -5\text{‰}$) in all of the serpentines occurring in the kimberlites investigated. Similar conclusions can be drawn for open systems (Fig. 3).

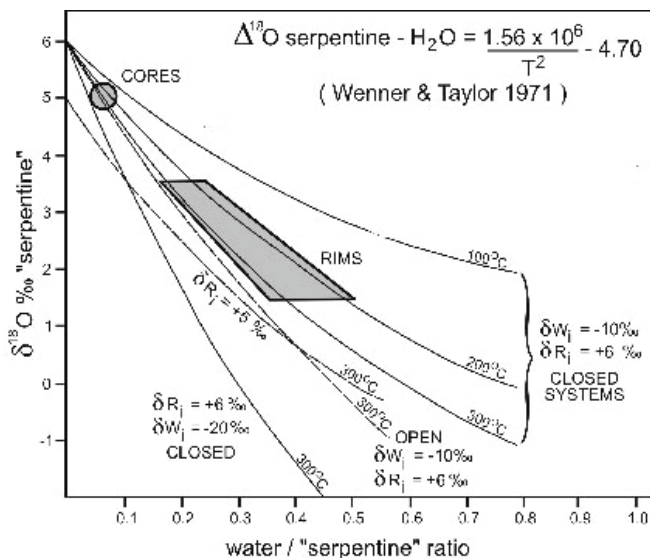


Fig. 3 Serpentine composition as a function of “water/serpentine” ratios in open and closed systems.

References

- [1] R.H. Mitchell et al. (2009) *Lithos* **112**, 452-464
- [2] D.B. Wenner and H.P. Taylor (1973) *American Journal of Science* **273**, 207-239

Trace element and Li isotope geochemistry of nyerereite and gregoryite phenocrysts from natrocarbonatite lava, Oldoinyo Lengai, Tanzania

R. H. Mitchell

Department of Geology, Lakehead University, Thunder Bay, Ontario, Canada P7B 5E1

Introduction

Oldoinyo Lengai, the world's only active carbonatite volcano, lies in the Gregory Rift Valley in northern Tanzania, eastern Africa (2.764°S, 35.914°E). The natrocarbonatite lavas erupted exhibit a wide variety of textures reflecting the conditions of eruption and crystal-liquid fractionation; these can range from phenocryst-dominated vesicular spatter to aphyric cryptocrystalline filter-pressed residua containing skeletal nyerereite. The natrocarbonatites are composed dominantly of gregoryite [(Na,Ca,K)₂CO₃] and nyerereite [(Na,K)₂Ca(CO₃)₂] phenocrysts (Fig.1) set in a matrix of a gregoryite-like phase, barian nyerereite, halite-sylvite, fluorite, potassian neighborite, and khanneshite (Ba-Sr-Mg-Na-Cl-F-rich carbonate). Although the major element compositional variation of the minerals forming natrocarbonatite are relatively well known [1,2], there are few data on their minor and trace element contents [3]. These data are important for understanding the differentiation of carbonate melts, as trace elements that are typically incompatible with respect to phenocrysts in common silicate magmas, are compatible in phenocrysts in natrocarbonatite. Many lavas are considered to be hybrids formed by the mixing of different batches of phenocryst-rich natrocarbonatite. Consequently, the phenocrysts could have been derived from magmas at different stages of evolution. The objective of the present study was to obtain trace element data for phenocrysts and apply these data to investigate the role of hybridization in the evolution of natrocarbonatite lavas.

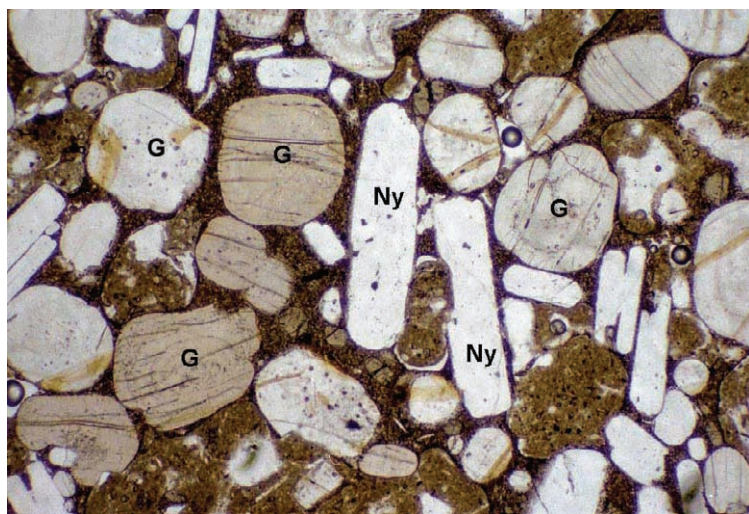


Fig.1 Natrocarbonatite lava with phenocrysts of gregoryite (G) and nyerereite (Ny).

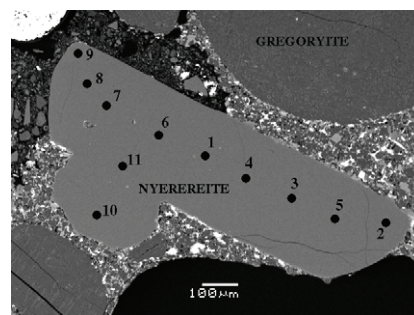


Fig. 2. SIMS analysis spots in a nyerereite crystal.

Analytical Methods

Trace elements and Li isotopic compositions of nyerereite (Fig. 2) and gregoryite were determined by secondary ion mass spectrometry using a Cameca IMS 4f instrument at the University of Edinburgh Ion Microprobe Facility. We used in-house carbonate standards *m93* and *Haxby* (both corals) for calibration of Na, Sr, Ba, Li and B contents, and NIST SRM610 glass for the remaining elements. All $\delta^7\text{Li}$ values were calculated with reference to the in-house *Haxby* coral standard ($\delta^7\text{Li} +28.01$). Gregoryite rims have $\delta^7\text{Li}$ values significantly different to those of nyerereite by amount +10%. Although data for nyerereite are considered to be realistic using this carbonate standard, gregoryite data may require calibration with an appropriate standard.

Results

This study determined the abundances of Li, B, F, Cl, P, Rb, Sr, Y, Ce, Ba, within and between nyerereite and gregoryite phenocrysts. These data show that, in general, nyerereite is enriched in Rb, Sr, Y, Ba, and Ce, but poorer in Li and P relative to gregoryite. Nyerereites

contain from 19700 to 25600 ppm Sr, and 300 to 1000 ppm Ce, whereas gregoryites typically have less than 8000 ppm Sr and less than 200 ppm Ce. Individual nyerereite and gregoryite crystals within and between natrocarbonatite samples are very variable in composition (Figs 3-4). Individual crystals are typically zoned with increasing or decreasing Sr and Ba from core to rim. Nyerereite from natrocarbonatites erupted at the same date from vents T49-2000 and T37B-2000 have a limited, but different range in composition. In contrast, nyerereite in natrocarbonatites erupted from vents T58 and T37, in 2004 and 1996, respectively exhibit a very wide range in composition that overlaps the T49-2000 and T37B-2000 data. In contrast to nyerereite, gregoryite does not exhibit any well-defined intra- or inter-occurrence or secular compositional variation. Natrocarbonatites represent rocks whose bulk composition has been determined by crystal accumulation in continually replenished magma chambers. Thus, phenocrysts and groundmass are not an equilibrium assemblage and bulk rock compositions do not represent those of the parental magmas.

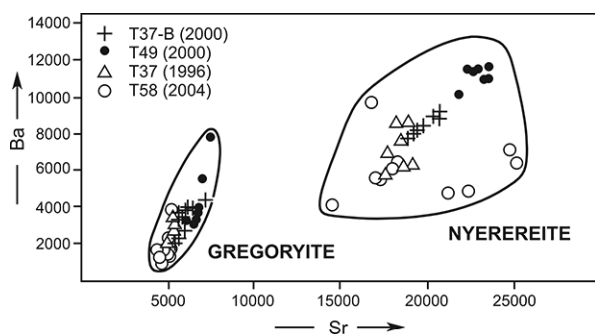


Fig. 3. Ba and Sr compositions of gregoryite and nyerereite

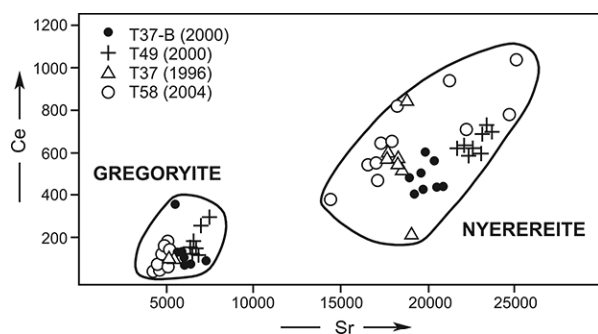


Fig. 4. Ce and Sr compositions of gregoryite and nyerereite

The Li isotopic composition of nyerereite ranges from +9.1 to -3.5 ‰ $\delta^7\text{Li}$ (Fig. 5), with the majority of these data ranging from about +3.5 to -2 ‰ $\delta^7\text{Li}$. These data show a wider range in $\delta^7\text{Li}$ compared to whole rock Li isotopic compositions (+3.3 to +5.1 ‰ $\delta^7\text{Li}$; [4]). Although individual crystals vary widely in their isotopic composition, there is trend of the margins of the crystal being enriched in ^6Li relative to the cores. Preliminary investigations by SIMS indicate that the groundmass of natrocarbonatite is richer in Li (>500 ppm) than the gregoryite phenocrysts. This can be considered to be a consequence of the enrichment in Mg, and hence Li^{2+} , in residual melt with differentiation, and the formation potassian neighborite $[(\text{K},\text{Na})\text{MgF}_3]$ and eitelite $[\text{Na}_2\text{Mg}(\text{CO}_3)_2]$. This observation suggests that isotopic compositions of the margins of the nyerereite phenocrysts can be explained by metasomatic interaction with the Li-rich groundmass of natrocarbonatite due to the more rapid diffusion of ^6Li relative to ^7Li .

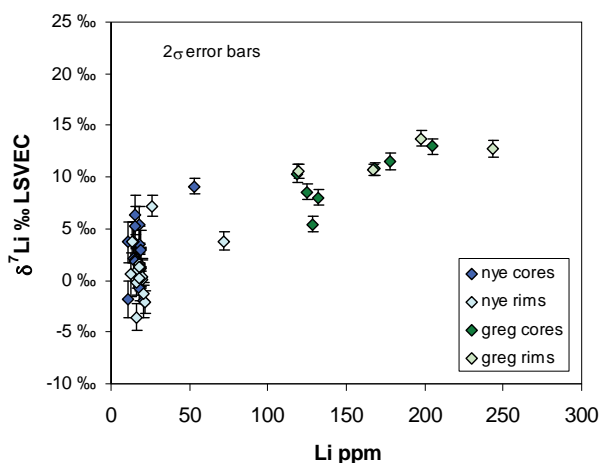


Fig. 5. Li isotope systematics of gregoryite and nyerereite cores and rims.

References

- [1] Keller J, Krafft M (1990) Bulletin of Volcanology **52**, 629-645.
- [2] Mitchell RH (1997) Mineral Magazine **61**, 779-789.
- [3] Zaitsev AN, et al. (2008) Proceedings of the Russian Mineral Society **137**, 101-111 (in Russian).
- [4] Halama et al. (2007) Earth and Planetary Science Letters **254**, 77-89.

In-situ isotope and volatile measurements of melt inclusions hosted in olivines from Phlegraean and Stromboli volcanoes, Southern Italy

M. Piochi¹, R. Moretti², G. De Astis³ & A. Mormone^{1,4}

¹Istituto Nazionale di Geofisica e Vulcanologia, Osservatorio Vesuviano, Via Diocleziano 328, Napoli, Italy

²Dipartimento di Ingegneria Civile, Seconda Università degli Studi di Napoli, Via Roma 29, Aversa, CE, Italy

³Istituto Nazionale di Geofisica e Vulcanologia, sezione di Roma, Via di Vigna Murata, Roma, Italy

⁴Dipartimento di Scienze della Terra, Università Federico II, Via di Vigna Murata, Napoli, Italy

Introduction

The conducted study is part of a research project funded by the Italian Government to Prof. R. Moretti. The project aims to study magma degassing through the analyses of variably differentiated (basaltic to trachytic) melts and data modelling based on a thermodynamic approach. The Ion Microprobe Facilities in Edinburgh provided analyses of the melt inclusions in olivine recovered as phenocrysts in pyroclastic products from the 2009 paroxysm of Stromboli and a 18-ka old eruption (Solchiaro I) from the Phlegraean Volcanic District, both in Southern Italy.

In particular, our interest was to obtain the isotopic ratios of O, S, B and, possibly, C, H, in addition to H₂O and CO₂, Cl and B contents of the melt inclusion from selected Phlegraean samples which have already been analysed by FT-IR. These data are in our opinion crucial 1) to define chemical homogeneity/heterogeneity of magma at a microscopic scale, 2) to constrain the mechanism of magma evolution and degassing, 3) to link type and relative content of the gases emitted at the surface during quiescent and eruptive phases with those of magmatic volatiles. Furthermore, the new data will complement the current literature that reported a number of petrological studies of the above mentioned volcanoes, and, in particular, H₂O and CO₂ contents determined by FT-IR on various deposits from the Campanian Volcanic Region. This information is vital for understanding magma petrology along the Italian volcanic belt and on volcanic risk monitoring and assessment.

The first part of this project in Edinburgh, for which we report preliminary results, concerned with melt inclusion-bearing olivine phenocrysts, 8 from the Phlegraean Volcanic District and 11 from Stromboli.

Sample features and results

Melt inclusions from Phlegraean Volcanic District are >100 µm (Fig. 1a) in size, the Stromboli ones are generally <200 µm (Fig. 1b). Some of them are glassy, some others contain bubbles and underwent micro-crystallization.

The Phlegraean Volcanic District melt inclusions had consistently high CO₂ contents (831-2620 ppm), water contents ranging from 0.9-1.3 wt.% and a narrow range of MgO contents (5.7-6.6wt.%) comparable to the average MgO content measured on a separated set of trachy-basaltic inclusions by electron microprobe at the Istituto Nazionale di Geofisica e Vulcanologia, Rome, Italy. The H₂O and CO₂ contents measured by ion microprobe are comparable to those determined by FT-IR on a separated set of olivines, although showing a deviation towards lower water content in the most carbonated glass (Fig. 1c). The volatile distribution reproduces the degassing pattern of a magma batch uprising from at least 350 MPa. Fluorine contents are between 1437 and 2402 ppm. Interesting features are the inter-relationships between the B isotopes and the H₂O, CO₂, MgO and B contents. B contents (up to ~15 ppm) are in the range of those indicated for the surface reservoirs (~2 ppm for the lower crust, ~10 ppm for the upper crust). The higher contents characterize the least carbonated and more hydrous and evolved melt inclusions. The relative δ¹¹B values are between -3.8 and -11.2‰ and decrease with CO₂. The lowermost values are comparable to those of Campi Flegrei and Ischia whole rocks.

The Stromboli inclusions had low to very low CO₂ contents (40-371 ppm). Three inclusions had very low MgO contents (0.1-0.3 wt%) low H₂O (<0.02 wt%), low TiO₂ (<0.06 wt%) but high CaO (>10 wt.%), suggesting these inclusions were not basaltic and probably not glass. The remaining inclusions had 1.9-3.8 wt.% MgO and 0.21-1.54 wt% H₂O. These inclusions are not basaltic and this contrast with data in the literature. F is between 852 and 2091 ppm, B between 31.4 and 49.7 ppm, the δ¹¹B between -2 and 11‰.

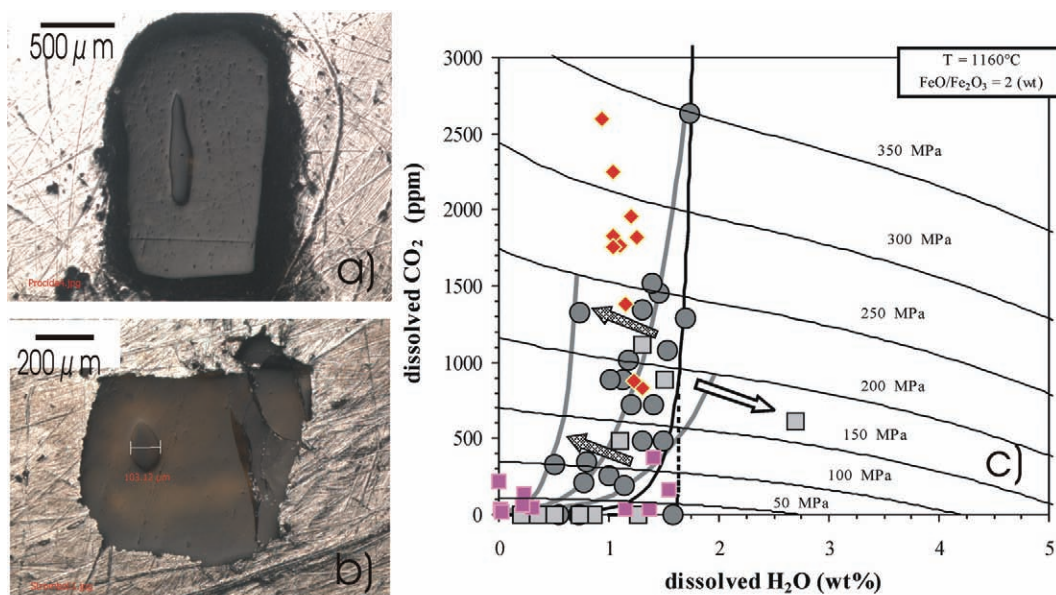


Figure 1- Melt inclusion in olivine phenocrysts from Solchiaro I in the Phlegraean Volcanic District (a) and Stromboli (b). In (c) variation of CO₂ and H₂O dissolved in the MIs glass trapped in the olivines from Solchiaro I. Isobars and the isopleths showing the pressure-related CO₂-H₂O evolution are re-calculated for the average shoshonitic composition of our analysed MIs and assuming a FeO/Fe₂O₃=2 and temperature of 1150°C using Papale's update model [1]. The diverse paths represent plausibly closed-system degassing conditions for the least evolved magmas with variable CO₂gas/H₂Ogas ratios in the gas phase. Arrows indicate isobaric processes of crystallization (white arrow) or CO₂ fluxing (semi-transparent grey line). Gray squares and circles are analyses by FT-IR vy [2], coloured symbols are new data: squares for Stromboli and rhombus for Solchiaro I.

Future work

The next step will concern with further preparation of already analysed inclusions (if survived) or on newly prepared olivines that must be adequately flat to allow high-precision measurements of O, S and possibly C isotopes. For this last set of isotopic measurements we plan to synthesize a glass from hydrous and carbonated shoshonitic rocks with known isotopic compositions to use as a calibration material.

Acknowledgement This work was supported by INGV-DPC 2005-2006 and by PRIN 2007M4K94A projects. We are grateful with Dr. John Craven for helpful indications and support in sample preparation and Dr. Cees-Jan De Hoog for measurements.

References

- [1] P. Papale et al. (2006) *Chemical Geology* 229, 78-95
- [2] A. Mormone et al. (2011) *Chemical Geology*, in revision

Appendix

Olivines were separated by hand-picking and polished in order to expose the hosted melt inclusion after mounting on a slide with Crystalbond™ at the Istituto Nazionale di Geofisica e Vulcanologia, in Napoli (Italy). Successive preparation were made at the Edinburgh by Dr. J. Craven. Olivines were removed from the glass slides and pressed in indium. Electron microscope investigations revealed that most of the melt inclusions were adequate for ion microprobe analyses of volatile concentrations and B isotopes. These analyses were done using a Cameca IMS 4f at the Edinburgh Ion Microprobe Facility. Unfortunately significant relief was observed on the samples and were therefore unsuitable for high-precision O isotopes.

The influence of CO₂ on phase relations and crystallisation kinetics in silicic magmas: a case study at Mount St. Helens

J. Riker¹, J. Blundy¹, A. Rust¹ & O. Melnik²

¹School of Earth Sciences, University of Bristol, Bristol, BS8 1RJ, UK

²Institute of Mechanics, Moscow State University, Moscow, 119192, Russia

Project motivation

Volatiles play a critical role in magma generation, ascent, and eruption due to their pressure-dependent solubilities. The H₂O and CO₂ contents of volcanic glasses and glassy melt inclusions are now routinely used to interpret magmatic processes [1]. While the effect of water on silicate melts is well-characterized, the effect of CO₂ on phase equilibria and crystallization kinetics, particularly in silicic magmas, remains poorly-understood. This project aims to clarify the influence of mixed H₂O-CO₂ fluids on the behavior of silicic magmas through a series of high-temperature, high-pressure experiments.

Our experiments are of three types: 1) volatile solubility experiments at lower crustal pressures; 2) low-pressure phase equilibrium experiments, to simulate shallow magma storage; and 3) isothermal decompression experiments, to simulate magmatic ascent. SIMS is the preferred technique for H₂O and CO₂ analysis of experimentally-produced glasses due to beam size requirements of vesicular and/or crystalline samples.

Results

We visited the IMF in June 2010 to measure H₂O and CO₂ contents in glasses from a preliminary suite of high-pressure solubility and isobaric phase equilibria experiments. These included samples run at 7-13 kbar and 800-1100 °C on a piston cylinder apparatus and 0.5-2 kbar and 800-950 °C on a cold-seal pressure vessel. Charges consisted primarily of CO₂-free and low-CO₂ bubbly glasses ± crystals. Our results highlight the difficulties of generating and preserving very hydrous glasses, and of limiting carbon contamination in CO₂-poor systems.

Water contents of analysed glasses range from 4.4-9.6 wt% in solubility experiments and 4.0-5.7 wt% in phase equilibria experiments. The latter have homogenous H₂O contents in good agreement with modelled water solubilities. In contrast, solubility experiments yield heterogeneous H₂O contents that fall well below model predictions for pure-water solubility (Fig. 1). This result was not wholly

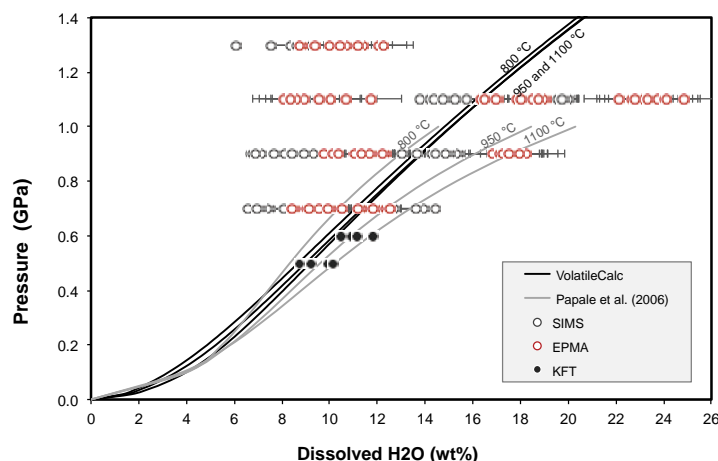


Figure 1. Pressure versus H₂O content of glasses from solubility experiments, measured by SIMS, EPMA, and KFT. Water contents have been corrected for quench vesiculation using an appropriate equation of state, assuming a pure water vapour. Modelled H₂O solubility curves from [3] and [4] are shown for reference.

anticipated due to the presence of quench bubbles in most samples. Such bubbles routinely form during quenching of hydrous silicate melts as a result of prograde H₂O solubility at pressures above ~5 kbar [2]. Analysis of resulting glasses will yield H₂O contents below true equilibrium values; however, we have tried to correct for the effects of quench vesiculation in Figure 1. Dissolved water contents may be further reduced by diffusion of H₂O from the surface of quenched glasses at room-temperature or under vacuum [2], as indicated by a comparison of SIMS analyses with EMPA analyses of water-by-difference (Fig. 1). The presence of unknown

amounts of carbon, discussed below, will also lower dissolved H₂O contents. Together, these factors may explain the extreme heterogeneity of measured water contents, which vary within individual samples by several weight percent. The highest water contents may reflect spots minimally affected by a combination of quench vesiculation, post-quench diffusion, and carbon contamination.

An unexpected result of this work was the discovery of substantial dissolved carbon in experimental glasses intended to be CO₂-free (hundreds, or more rarely, thousands of ppm of carbon as CO₂). Measured CO₂-H₂O contents indicate unreasonably low equilibration pressures, due in part to H₂O

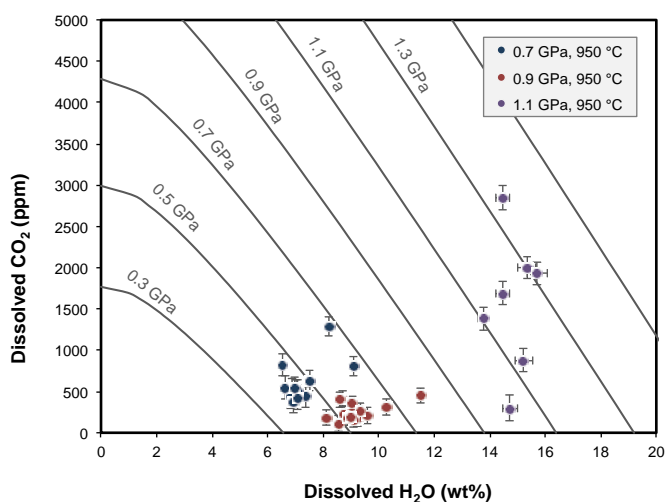


Figure 2. H₂O and CO₂ contents of three experimental glasses measured by SIMS, plotted against modelled solubility isobars [3]. These runs were intended to be CO₂-free, but carbon is clearly present. CO₂ contents inferred from carbon measurements are variable within each sample and range from hundreds to thousands of ppm.

loss, although CO₂ contents within single samples are still highly variable (Fig. 2). Unanticipated, or ‘phantom’, carbon is a much-discussed (but rarely published) problem in the field of experimental petrology. Moreover, the presence of carbon is often wholly undocumented in H₂O-only experiments, where carbon is not expected to be present and is therefore not analysed. Minor carbon contamination in subsolidus or carbon-rich systems is unlikely to significantly alter phase relations. However, in our system, any carbon present as CO₂ in the capsule will reduce H₂O solubility (see isobars in Fig. 2) and partition readily into vapour. Because the amount and speciation of carbon in the system is unknown (and perhaps time-dependent, as discussed below), its presence severely limits our ability to interpret volatile solubilities and phase equilibria.

Discussion

Data obtained at the IMF has been pivotal in directing experimental technique and data interpretation as this project continues. SIMS is the ideal technique for H₂O analysis of low-pressure run products, although water analysis by SIMS alone may not be feasible for the most hydrous glasses generated in solubility experiments (>~10 wt% H₂O). Bulk carbon analysis indicates that carbon contents measured by SIMS cannot be accounted for by contamination of starting materials. However, carbon from graphite furnaces used in piston cylinder assemblies can potentially infiltrate samples by diffusing through noble metal capsules [5]. Such an origin is consistent with the heterogeneity of carbon analyses within single samples, as carbon does not penetrate capsules evenly, and the degree of carbon infiltration will vary with time [5]. We are currently exploring methods for trapping carbon prior to sample infiltration. SIMS remains the preferred method for CO₂ analyses associated with this project and will be supplemented by FTIR to distinguish the effects of carbon infiltration from external sources.

References

- [1] G. Moore (2008) *Reviews in Mineralogy and Geochemistry* **69**, 333-361
- [2] O. Paillat et al. (1992) *Contributions to Mineralogy and Petrology* **112**, 490-500
- [3] S. Newman and J.B. Lowenstern (2002) *Computers and Geosciences* **28**, 597-604
- [4] P. Papale et al. (2006) *Chemical Geology* **229**, 78-95
- [5] R. Brooker et al. (1998) *American Mineralogist* **83**, 985-994

Towards developing a proxy for ocean seasonality: Step 1. Characterisation of natural variability in geochemical signals of planktonic foraminiferal populations

Aleksey Sadekov¹, Kate Darling¹, Dick Kroon¹, Raja Ganeshram¹, Ulrike Fallet², Geert-Jan Brummer²

¹ School of GeoSciences, University of Edinburgh, Edinburgh EH9 3JW, UK

² Royal Netherlands Institute for Sea Research, NL-1790 AB Den Burg, The Netherlands

Introduction

The coupled ocean-atmosphere climate system is responsible for seasonal and interannual changes in seawater temperature and salinity [1]. Accurate reconstruction of ocean variability is crucial in understanding complex climate changes in areas with high seasonal and interannual variability such as the Eastern Equatorial Pacific (EEP) and monsoon-affected regions [2], but remains mostly unachieved. The primary obstruction in reconstructing seasonality is the presence of large and mostly unconstrained biological effects on proxies for seawater temperature and salinity, such as Mg/Ca and $\delta^{18}\text{O}$ compositions of foraminiferal shells [3, 4].

In this pilot project we proposed to use SIMS to study the natural variability in geochemical signals of modern and fossil populations of *G. sacculifer* (planktonic foraminifera) to evaluate their potential use as a proxy for seasonality. The two main objectives of this project are: 1) to develop a fast and precise (reproducible) method of measuring Mg/Ca composition of foraminifera shell chambers using SIMS; and 2) to quantify the natural variability of Mg/Ca values using high quality sediment trap samples (live population) with bi-weekly resolution and core-top samples (fossil population) collected directly below the sediment trap.

Method development

Development of the SIMS method for Mg/Ca measurement was primarily focused on achieving sufficient internal precision and external day to day reproducibility of the measurements to obtain statistically significant variations between sediment trap samples. To achieve this we measured Mg/Ca values of *G. sacculifer* shells using a very low intensity beam (0.02-0.04 nA) focused to 1-2 μm size and by profiling across the shell cross-sections with 1 μm step size. This allowed us to generate 15-60 individual spot measurements for each profile giving sufficient statistical background to accurately measure profile mean Mg/Ca values. To minimise the effect of Mg/Ca heterogeneity within foraminifera shells three to four replicate profiles for each shell were averaged to produce mean shell Mg/Ca values. We found that using this method we were able to achieve 1-4% precision for Mg/Ca ratios of individual foraminifera shells (**Fig. 1**), which is comparable or better to previously reported microanalytical methods such as laser ablation ICP-MS, SIMS or electron microprobe [4, 5]. We also found that a significant proportion of day to day variability is caused by heterogeneity of the standards used for calculating absolute Mg/Ca values at 1 μm spatial resolution. This variability reached 50-100% for standards based on biogenic CaCO_3 such as coral aragonite, which made these standards unreliable for the proposed measurements. We found that the OKA-C standard gave the most reliable measurements of Mg, Ca concentration (i.e. 0.5-1% variability) and is therefore preferable for standardisation under small size beam conditions.

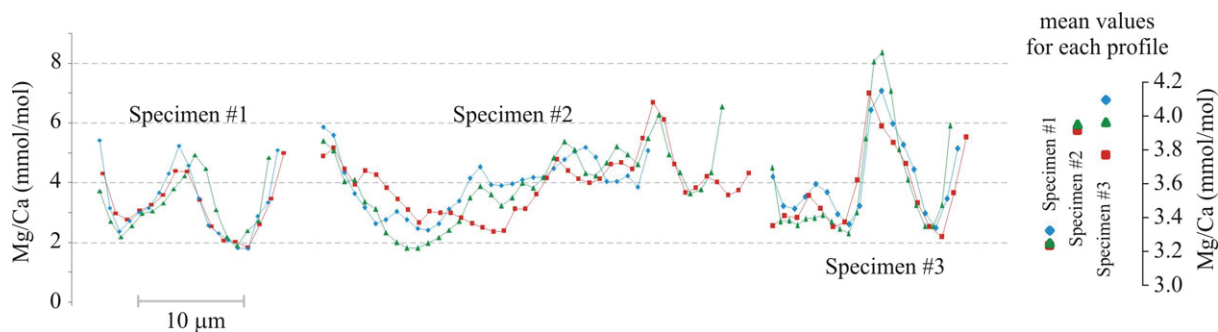


Fig. 1 Reproducibility of Mg/Ca measurements of *G. sacculifer* final chambers using SIMS 1- μm step profiling across the chamber cross-section. Three replicate profiles (marked by coloured symbols) show reproducible Mg/Ca patterns and average Mg/Ca values for each specimen (indicated on the right).

Results

Natural variability of the *G. sacculifer* population was measured using the following approach. Four samples from a sediment trap, each containing 13-15 individual shells of *G. sacculifer*, were selected to quantify Mg/Ca variability of 'live' species populations. These four samples were collected biweekly in Mozambique Channel (Fig. 2) and represent periods with warmest (first two samples) and coldest (the other two sample) sea surface temperatures. In addition we also measured 30 shells from sediment population of *G. sacculifer* collected from core-top samples located below the sediment trap site. As seawater temperature was closely monitored during sample collection this approach gave us a unique opportunity to quantify the biological component of Mg/Ca variability. It also allowed us to compare natural Mg/Ca variability with recorded seawater temperature variability to test the sensitivity of the Mg/Ca ratio in recording the amplitude of seawater temperature changes.

Analyses of the natural variability of *G. sacculifer* were completed only a few months ago and consequently most of the results are currently still being processed. However, preliminary results show the great potential of Mg/Ca proxy in recording seawater temperature variations. For example, using *G. sacculifer* Mg/Ca ratios from one of the sediment trap samples collected in March 2004, we were able to track the change in seawater temperature cause by typhoon disturbance of the water column (Fig. 2). The Gafilo Typhoon passed near the sediment trap site on 3-11 March 2004 causing local upwelling of relatively cold subsurface waters, which was recorded by satellite and *in situ* measurements as a 2-3°C drop in temperature. This increase in temperature variability was recorded in foraminiferal Mg/Ca composition collected during this period. Mg/Ca values of the foraminiferal shell collected during the week of typhoon activity show much greater variability in comparison with other sediment trap samples collected several weeks later (Fig. 2 right) and are characterised by stable sea surface temperatures (SST).

Direct comparison of absolute temperature variation recorded by Mg/Ca proxy and measured *in situ* SST show significant deviations. These deviations are attributed to biological effects on foraminiferal Mg/Ca composition as well as the fact that *G. sacculifer* inhabit the upper 100 m of the water column and therefore integrate temperatures across its habitat interval into Mg/Ca variability. We are currently working to decouple these two possible sources of variability to accurately quantify the biological component. Regardless of these deviations in absolute values it is clear that Mg/Ca proxy is sensitive enough to record even small (weekly) disturbances in seawater temperatures providing significant support in its use for reconstructing seasonal, decadal and multi-decadal variations in seawater temperatures.

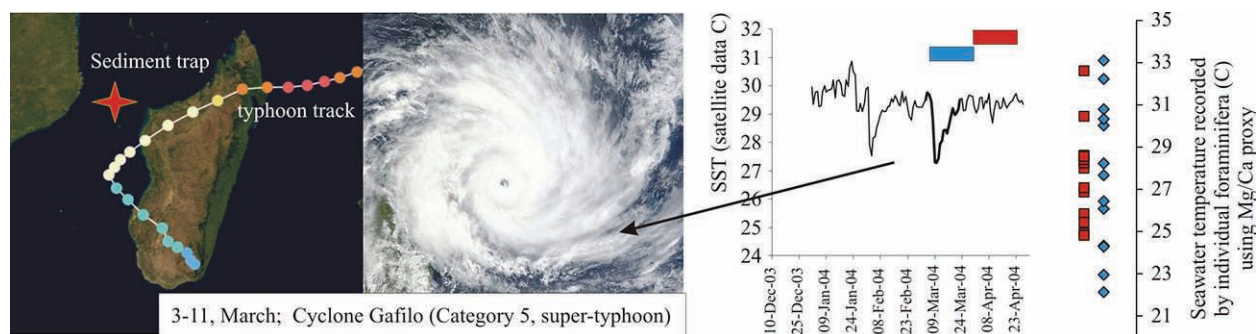


Fig. 2 Left: Location of the sediment trap, track and satellite image of the Cyclone Gafilo passed in Madagascar area during March 2004. Note that scale on both images is approximately the same. **Right:** Variation in sea surface temperature at sediment trap site recorded by satellite. Bold line marks time of the cyclone activity in this area. Blue and red rectangles correspond to two sediment trap collection intervals of foraminiferal samples analysed using SIMS. The small red squares and blue diamonds (13 shells each) represent temperatures recorded by individual foraminifera based on their Mg/Ca ratios. Note that most of the red symbols are tightly group around 25-29°C temperature range whereas blue symbols (foraminifera collected during cyclone activity) are spread along a 22-33°C interval reflecting a significant increase in variability.

References

- [1] J. Berdowski et al. (2000) *The Climate System*. Balkema Publishers/Swets & Zeitlinger Publishers, Lisse, The Netherlands. 186 pp.
- [2] D. W. Lea (2003) in: *The Ocean and Marine Geochemistry* (H. Elderfield, Ed.) Elsevier, New York.
- [3] H. J. Spero and D. W. Lea (1993) *Marine Micropaleontology*, 221-234
- [4] A. S. Sadekov et al. (2008) *Paleoceanography*. DOI:10.1029/2007PA001452
- [5] K. L. Bice et al. (2005) *Geochemistry Geophysics Geosystems*. DOI:10.1029/2005GC000974

Petrogenesis of kimberlite: mantle sources and shallow level contamination

C. Sarkar¹, C. D. Storey² & C. J. Hawkesworth³

¹Department of Earth Sciences, University of Bristol, Bristol, BS8 1RJ, UK

²School of Earth and Environmental Sciences, University of Portsmouth, Portsmouth PO1 3QL, UK

³Office of the Principal, University of St. Andrews, St Andrews, Fife, KY16 9AJ, Scotland

Introduction

Kimberlite is potentially one of the most important rocks to study mantle geochemistry but it is often difficult to derive primary geochemical signatures as it contains considerable amounts of foreign material and its primary geochemical characteristics are strongly affected by secondary alteration after emplacement [1]. Using different geochemical criteria it is possible to determine the effect of crustal contamination. However, it is almost impossible to eradicate all of the effects of the contaminants from bulk rock analyses of kimberlites. Recent developments in analytical technology have enabled analyses of mineral separates, which, in some circumstances, can circumvent the affects of crustal contamination and late stage alteration successfully. Perovskite (CaTiO₃), a common groundmass mineral in kimberlites, has increasingly been used to determine more reliable isotopic signatures (Sr, Nd and Hf) than available from whole rock studies [2-4]. It is a major repository of the trace elements and REE with a very low Rb/Sr (<0.005) ratio. Thus perovskite has great potential to represent the pre shallow level contamination kimberlite magma. Although the crystallisation of perovskite takes place at a relatively late stage (1000^o-800^oC), due to rapid ascent of kimberlites [5] the geochemical characteristics of the magma, which perovskites crystallise from, are thought not likely to change much from their near-source characteristics.

Stable oxygen isotopes can distinguish between certain magmatic and crustal processes. The upper mantle is relatively homogeneous with respect to $\delta^{18}\text{O}$, as reflected in olivine and pyroxenes in mantle peridotites [6] and zircon megacrysts in kimberlites [7]. Zircon, being a refractory mineral with a higher closure temperature, provides a more robust isotope composition of the upper mantle. On the other hand, $\delta^{18}\text{O}$ of sediments from the upper crust and meteoric water have elevated $\delta^{18}\text{O}$. Thus, the $\delta^{18}\text{O}$ values of typical mantle zircon ($\delta^{18}\text{O} = 5.3 \pm 0.3\text{‰}$) can be used to distinguish primary mantle-derived magmatic signatures from those altered by hydrothermal processes and interaction with meteoric water and incorporation of sediments [8]. The objective of this study was to use O isotope and trace elements to distinguish between contaminated and uncontaminated perovskites from two kimberlites from South Africa. The Orapa A/K1 kimberlite (93 Ma) is a typical crater and diatreme facies kimberlite with both volcanoclastic and pyroclastic deposits. The Wesselton kimberlite (90 Ma) is a complex mixture of hypabyssal (that was not violently disrupted during emplacement) and tuffisitic kimberlite in a simple diatreme with more complex root zones. We developed and utilised the technique for measuring in-situ O isotopes (Cameca 1270 ion microprobe) followed by trace element analysis (Cameca ims 4f ion microprobe) in perovskites at Edinburgh. We also analysed Sr isotope ratios at the University of Bristol. Combined use of O isotope with trace elements and Sr isotopes would help us to determine the effect of contamination and also to interpret the variation of O isotopic signature from perovskites, if any.

Results

One hundred and eighteen perovskites from 12 samples from Orapa A/K1 kimberlite have two distinct peaks in $\delta^{18}\text{O}$ with mean values of +3.6 ‰ and -0.6 ‰ respectively with a variable Fe/Nb (0.36-1.37). The Wesselton perovskites have $\delta^{18}\text{O}$ around +4 ‰, and they have higher Fe/Nb ratios (Fig 1). Trace element concentrations and the chondrite normalised REE pattern of all perovskites from Orapa kimberlites are similar except Nb content which is low in the negative $\delta^{18}\text{O}$ perovskite population (Fig 2). Wesselton perovskites also have similar trace element content, however the ranges of concentrations of most of the elements are smaller compared to Orapa perovskites. ⁸⁷Sr/⁸⁶Sr ratio from perovskites from Orapa shows variation between 0.703102 - 0.705407 ± 31 (2SD) compared to Wesselton perovskites which are clustered between 0.704408 - 0.705580 ± 19 (2SD).

Interpretation

Absence of any perovskite with an elevated $\delta^{18}\text{O}$ from both kimberlites is an important observation and it has been interpreted that the perovskites crystallised from magma that was not contaminated by

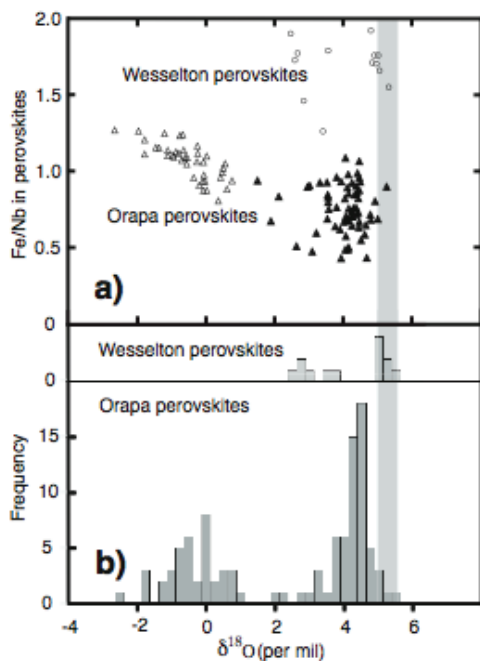


Fig 1: a) $\delta^{18}\text{O}$ vs Fe/Nb plot of the perovskites from Orapa (open and closed triangle) and Wesselton (open circle) kimberlites. Different symbols have been used for Orapa perovskites to differentiate between the 2 perovskite clusters. The shaded area shows the $\delta^{18}\text{O}$ value of mantle based on zircon analyses [7]. b) Histogram showing the distribution of $\delta^{18}\text{O}$ of all Orapa and Wesselton perovskites.

upper crustal sediment or meteoric water. Similarity of all trace elements also supports this hypothesis. The relatively larger range of trace elements in Orapa perovskites are possibly due to longer crystallisation over Wesselton and it indicates a fractionation trend in Orapa. No experimental data exists regarding the O fractionation between perovskite and kimberlitic melt. Thus, based on the theoretical calculations of Zheng et al., (1998) [9] and Zhao and Zheng (2002) [10] we propose that one group of Orapa perovskites (with $\delta^{18}\text{O}$ of +3.6 ‰) and the Wesselton perovskites (with $\delta^{18}\text{O}$ of +4 ‰) are representative of mantle like O isotope signature from perovskites. However there are several processes that can produce negative $\delta^{18}\text{O}$ which include high temperature water-rock interaction and post magmatic hydrothermal activity, assimilation, longer crystallisation and degassing. Though the Sr isotope ratio shows some variation in Orapa perovskites, it is difficult to modify $^{87}\text{Sr}/^{86}\text{Sr}$ by assimilation as the calculated liquid, from which perovskites crystallised, contain abundant Sr (>1000 ppm) while the country rock in South Africa have little Sr (up to 50 ppm) which is also not very radiogenic (0.704-0.706) [11]. The variation in $^{87}\text{Sr}/^{86}\text{Sr}$ is possibly due to calcite containing radiogenic Sr present in fractures within perovskites. Although water-rock interaction and/or crystallisation for a longer period can produce negative $\delta^{18}\text{O}$, it would produce a trend in $\delta^{18}\text{O}$ from the perovskites rather than two distinct populations. We therefore interpret the group of perovskites with negative $\delta^{18}\text{O}$ to be post-degassing phase perovskites. Degassing is a common phenomenon in a volatile rich kimberlite magma near the surface and degassed CO_2 would make the residual magma depleted in ^{18}O , which would make the $\delta^{18}\text{O}$ of the post degassing perovskites significantly low [10, 12]. Orapa, being a crater facies kimberlite, contains evidence of degassing and vigorous fluidisation whereas Wesselton, being a hypabyssal kimberlite, retains most of its gasses and appears as sills. The

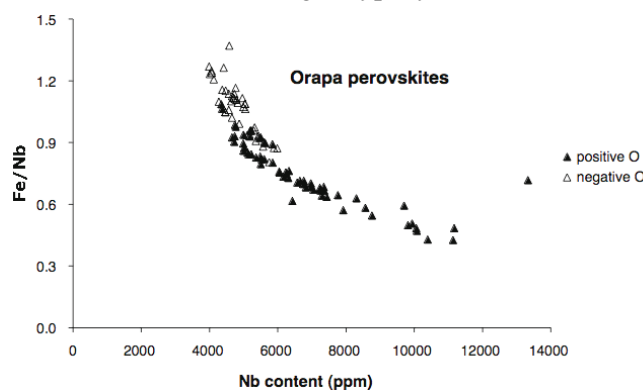


Fig 2: Variation of Nb concentration between two groups of Orapa perovskites with different $\delta^{18}\text{O}$ values.

lack of negative $\delta^{18}\text{O}$ from Wesselton perovskites also supports this interpretation. Degassing, being a rapid event correlates well with the two populations of $\delta^{18}\text{O}$ from Orapa perovskites instead of a trend. There is some textural evidence from Orapa, which suggests late crystallisation of some perovskites near to the surface and possibly after degassing. The low Nb content in the negative O group of perovskites is due to preferential partition of Nb into rutile, which crystallises after the initial mantle like perovskites but predates late stage perovskites with negative $\delta^{18}\text{O}$.

References

- [1] R.H. Mitchell, Kimberlites (1986) Mineralogy, Geochemistry and Petrology, Plenum Press, New York;
- [2] L.M. Heaman (1989) Earth and Planetary Science Letters **92**, 323-334;
- [3] C. Patonet et al. (2009) Lithos **112**, 296-310;
- [4] Y.H. Yang et al. (2009) Chemical Geology **264**, 24-42;
- [5] L. Wilson, J.W. Head III, (2007) Nature **447**, 53-57;
- [6] D. Matthey et al. (1994) Earth Planet. Sci. Lett. **128**, 231-241;
- [7] J.W. Valley et al. (1998) Contributions to Mineralogy and Petrology **133**, 1-11;
- [8] J.W. Valley et al. (1994) Earth Planet. Sci. Lett. **126**, 187-206;
- [9] Y. Zheng et al. (1998) Science in China Series D: Earth Sciences **41**, 95-103;
- [10] Z.F. Zhao, Y.F. Zheng (2002) Chemical Geology **193**, 59-80;
- [11] A.P. Le Roex et al. (2003) Journal of Petrology **44**, 2261-2286;
- [12] I. Appora et al. (2003) Geochimica et Cosmochimica Acta **67**, 459-471

The Role of Volatiles During Historical Eruptions From Kilauea Volcano, Hawai`i: Constraints on Source to Surface Processes Using Melt Inclusions

I.Sides¹, M. Edmonds¹ & J. MacLennan¹

¹Department of Earth Science, University of Cambridge, Downing Street, Cambridge, CB2 3EQ

Objectives

Kilauea Volcano, Hawai`i, is the most active basaltic volcano in the world and one of the most intensely monitored. Eruptions from the volcano span a broad spectrum of styles from effusive to explosive and phreatomagmatic. Continuous study over the past fifty years has revealed much about the plumbing system of the volcano and the geochemistry of its lavas. Melts are transported from ~60 km depth to a shallow reservoir 2 – 4 km beneath the summit caldera. The volcano is known to tap a heterogeneous source region giving rise to changes in the isotopic composition of melts supplied to the summit reservoir, over decades to millennia. However, no previous studies of Kilauea have investigated volatile heterogeneity of the melts entering the magma reservoir, nor whether variations in magmatic volatile concentrations contribute to the often dramatic changes in summit eruption styles. This project explores changes in the volatile concentrations of parental melts with time, melt degassing prior to and during eruptions, and the impact on eruption style.

Approach

We have analysed ~300 olivine hosted melt inclusions for major, trace and volatile elements from tephra samples of 28 historical eruptions at the summit and upper east rift zones of Kilauea Volcano. We use tephra, rather than lava samples to minimise the effects of diffusive loss of H₂O from the melt inclusions. Glasses and inclusions were analysed for ¹H, ¹²C, ⁷Li and ¹¹B by SIMS, on a Cameca IMS-4f ion microprobe at the University of Edinburgh. Subsequent analyses of major and trace elements were performed using a Cameca SX100 electron microprobe and LA-ICPMS at the University of Cambridge. Analyses have concentrated on samples erupted between 1400AD and the 2008-present day summit eruption.

Results

The major element chemistry of the melt inclusions and matrix glasses from Kilauea are dominantly controlled by fractionation of olivine. Inclusion hosting olivines vary from Fo₇₈ – Fo₈₉. Volatile saturation pressures based on CO₂ and H₂O solubility and calculated using VolatileCalc [1] suggest that extensive crystallisation and MI entrapment occurs at shallow depths within the crust (< 1km to 7km depth).

CO₂ and H₂O are both highly incompatible elements during mantle melting, and have been shown to have near constant ratios with Nb and Ce in undersaturated mantle melts [2]. If we use the ratio of CO₂/Nb = 239 +/- 46 and H₂O/Ce = 180 +/- 30 [2], it is possible to estimate predicted pre-degassed volatile concentrations of the melts from each eruption. Parental melts vary between 2800 to 7400 ppm CO₂ and 0.4 to 1.2 wt% H₂O over the 600 year period. Despite large variations in the volatile concentrations of melts supplied over time, there are no obvious correlations with eruption styles. Measured melt inclusion CO₂ and H₂O are strongly decoupled from their corresponding trace elements such that most of the variability in the volatile concentrations produced during mantle melting is lost by extensive degassing of 5-6000ppm CO₂ prior to and during storage at relatively shallow levels within the crust, (fig. 1).

We have divided the 28 eruptions into six categories of eruption style: effusive, spattering (eruption of tephra up to 50m height above the vent), fountains (50 – 300m), high fountains (> 300m), phreatomagmatic and the 2008-11 summit eruption. Analysed melt inclusion volatile concentrations for all historical eruptions vary between < 30 – 1160ppm CO₂ and 0.07 – 0.58 wt% H₂O (fig. 2). We use cumulative histograms to examine populations of inclusions from each eruption style. The data clearly show that all ‘explosive’ groups (spattering, fountains and high fountains) lie at higher volatile concentrations than effusive end members, and that the inclusions from high fountain producing eruptions have significantly higher CO₂ concentrations than any other eruption styles (fig. 3a). Calculated saturation pressures also suggest that melts supplying these high fountain eruptions last-equilibrated at greater depths within the storage region (fig. 3b). The melts likely had much shorter residence time beneath the summit than other Kilauea magmas, or may have bypassed the summit

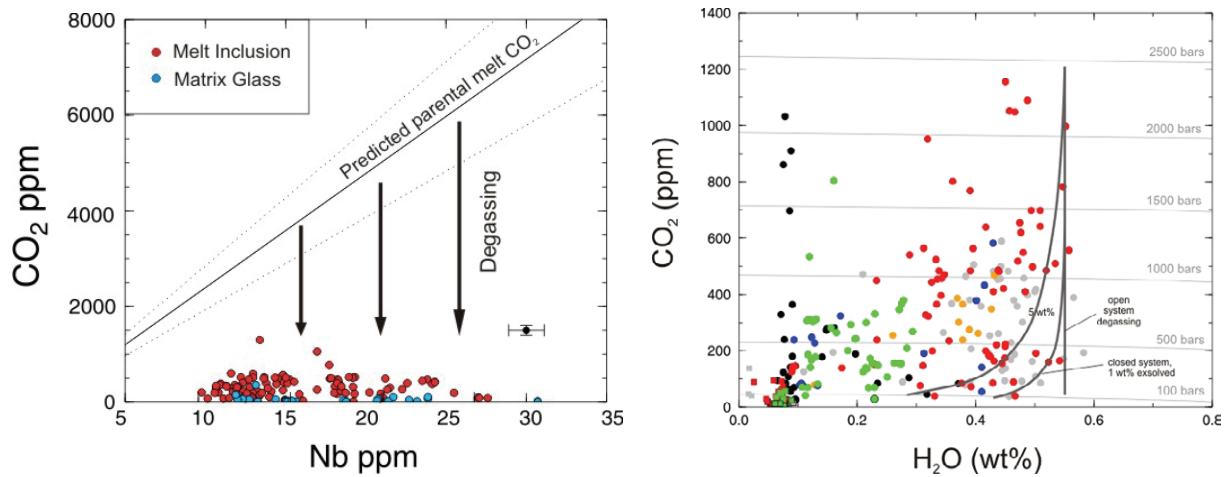


Figure 1 (Left). Measured CO_2 versus Nb in melt inclusions and matrix glasses from all analysed eruptions. Black line represents predicted undegassed CO_2 concentrations of parental melts; dotted lines are error margins for predicted values. **Figure 2** (Right) CO_2 vs H_2O for all MIs. Degassing pathways are shown in dark gray; isobars in pale gray. Both are calculated using VolatileCalc [1]. See Fig. 3 for colour code of symbols.

reservoir entirely *en route* to the surface. This has important implications for existing models of lava fountains at Kilauea, which typically attribute fountains to shallow exsolution of an H_2O rich gas phase [3]. The data implies that CO_2 may play a much more significant role in driving these extremely high fountains, both at the summit and within the east rift zone. This newly acquired data is being used in numerical models of magma degassing and fragmentation to gain a better understanding of the importance of CO_2 during these events.

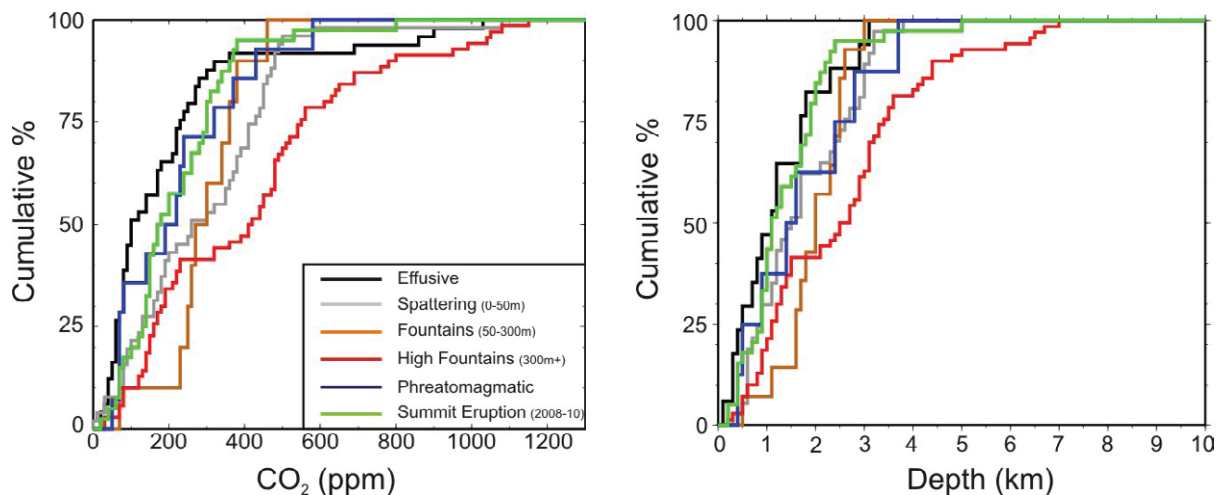


Figure 3: Cumulative histograms for MI populations produced during different eruption styles. The cumulative % refers to the number of inclusions analysed for CO_2 (left) and calculated saturated pressures (right).

During the course of this study we have also been investigating the means to improve the SIMS calibration of the CO_2 analyses on basaltic glasses. We are currently performing FTIR measurements of CO_2 and H_2O in a suite of natural glasses which have been used as secondary standards throughout sessions on the Cameca 4f. We believe this will be extremely beneficial for improving the overall accuracy of low-concentration CO_2 analyses in basaltic glasses. The new calibration may result in an overall reduction of the CO_2 concentrations presented above, but will not affect the results of this study.

References

- [1] S. Newman and J.B. Lowenstern (2002) *Computers and Geosciences* **28**, 597-604.
- [2] A. Saal et al. (2002) *Nature* **419**, 451-455
- [3] E.A. Parfitt (2004) *Journal of Volcanology and Geothermal Research* **134**, 77-107

Monazite saturation in silicate melts at high pressure with implications for subduction zone volcanism

S. Skora & J. Blundy

Department of Earth Sciences, University of Bristol, Bristol BS8 1RJ, UK

Introduction

The presence or absence of the accessory minerals allanite and monazite at sub-arc depth is of great interest to the study of trace-element cycles in subduction zones, as they appear to be the main carrier of light rare earth elements (LREE) and thorium (Th) in subducted basalts and sediments, respectively. Recent work has emphasised that the absolute concentration of Σ LREE(La-Gd) in fluids/melts released in subduction zones is controlled by solubilities of their respective host accessories (e.g. [1]). Because accessory phase solubilities are generally strongly temperature dependent, they are widely used as geothermometers, e.g. Montel's monazite saturation geothermometer suitable for crustal granites [2]. Based on this behaviour, Plank et al. [3] have recently developed an H₂O/Ce geothermometer, aiming to constrain slab-top temperatures beneath arcs. However, some questions remain as to the applicability and accuracy of that thermometer (see [4]). This study investigates the mechanism of monazite dissolution in hydrous melts and related consequences for monazite-based thermometry.

Experiments and results

This study uses both trace element-doped and undoped synthetic sediment starting materials. One experimental sequence uses undoped trace element concentrations at T = 800, 850, 900 and 950°C. Another sequence with variably doped LREE and Th was carried out at 850°C. Pressure and H₂O were held constant at 3 GPa and 6.5 wt%, respectively. As all our experiments were performed at T > 800°C, they are above the wet solidus for metasediments at 3 GPa (e.g. [3]). Analysed melt pools are peraluminous, broadly granitic in composition. Other phases present include garnet + kyanite + monazite + ilmenite + rutile ± phengite ± quartz ± clinopyroxene.

Analytical methods

Melt pools (± garnet) of 12 samples were analyzed using the Cameca IMS-4f at the Edinburgh Ion Microprobe Facilities. Counted selected isotopes were normalised against ³⁰Si as determined by EMPA. Subsurface inclusions and contamination were monitored using the counts per seconds versus time display, indicated by an increase in contaminant characteristic elements (e.g. high Ti: rutile/ilmenite; high Ba: phengite; high HREE: garnets, etc.). Compromised cycles were subsequently excluded from the average calculations. Rare earth element oxide interferences were minimized in our experiments by the careful choice of elements. Remaining molecular interferences were removed by conventional peak stripping. Ion yields were calibrated on NIST SRM 610, using concentrations given in Pearce et al. (1997). In contrast to our previous study ([4]), we have analyzed a large suite of secondary standards (MPI DING glasses: ML3, ATHO, STH5; USGS standards: BCR2, GSD1; LIPARI standard; n=2-3 per standard) throughout the entire session. Calculated Pearson correlation coefficients of thus obtained calibration curves are 0.97 or better (except for Cs and Pb which we will likely not use), suggesting that any analytical offsets from true values are of systematic nature. Calculated correction factors were hence applied to all our data.

Discussion

One basic assumption of monazite solubility is that it dissolves into a liquid until it has reached saturation, and vice versa. It has further been assumed that monazite solubility is governed by a single, low-abundance component that is essential to the mineral structure (essential structural component, or "ESC"), which in the case of monazite is suggested to be Σ LREE. It then follows that the amount of dissolved LREE in fluids or melts equals monazite solubility. It further suggests that any LREE that is present beyond that of monazite saturation should simply lead to its crystallization, keeping LREE concentration in the fluid/melt constant. This has been used in the past to argue that adding ESCs to levels higher than natural will not affect solubility measurements, in general. Furthermore, it was

considered to be of advantage because doping of starting materials eases positive identification of the accessory phase of interest. Note that this concept works for simple accessory phases such as rutile. However, we observe different amounts of Σ LREE at monazite saturation depending on how much Σ LREE was initially added to our starting material (Fig. 1A, 850°C experimental sequence), in contrast to the idea that doping does not affect solubility measurements. In addition, we find that monazite solubility in our undoped starting material is considerably less than what would be predicted by Montel ([2]; Fig. 1A). Figure 1A shows that application of his geothermometer to our data would yield temperature estimates that are about 100°C too low. The offset is remarkably systematic for all experiments, resulting into a slope that runs parallel to the one calculated using Montel [2]. We believe that this is due to the fact that, in high-pressure hydrous melts, monazite dissociates on dissolution ($REEPO_4^{mon} \leftrightarrow REE^{3-melt} + PO_4^{3+melt}$). If this is the case (and not $REEPO_4^{mon} \leftrightarrow REEPO_4^{melt}$ as assumed by Montel [2]), then monazite solubility is an inverse function of phosphorous in the melt (e.g. $P_2O_5 \uparrow = LREE \downarrow$). This will lead to different monazite solubilities for differently doped (with Σ LREE only) starting materials because LREE/P ratios will be different in each case. Indeed, we do find this strong inverse correlation, as predicted, which is shown in Figure 1B. The fact that our undoped experimental sequence has much lower apparent monazite solubilities than predicted by Montel [2] is explained by the fact that in subduction zones, sediments have significantly higher molar P than LREE (e.g. [5]). This arises because LREE are known to subduct as trace elements in fish teeth apatite, with apatite being considerably more soluble than monazite at the same P-T-X conditions. Hence, monazite solubility must be studied in undoped experimental starting materials in order to be applicable to subduction zones.

Summary

Our results shed light on the monazite dissolution mechanism in hydrous melts. It has important consequences as to the applicability of Montel's monazite geothermometer at high-pressure conditions in all cases where $P > LREE$. A prominent example where its application would be seriously hampered is subduction zones. With our results, we plan to update Plank's H_2O/Ce thermometry calibration, aiming to establish a more accurate slab-top geothermometer.

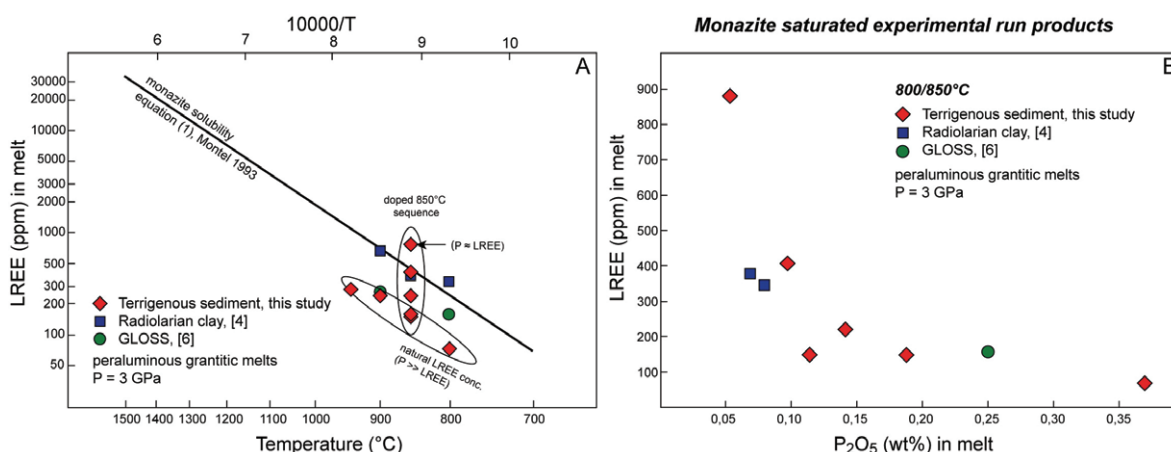


Figure 1A. Undoped experiments have lower apparent monazite solubilities than predicted using Montel [2]. We also find strong very variable monazite solubilities depending on how much Σ LREE was initially added to our starting materials (850°C sequence and other shown experiments). **1B)** Inverse LREE/P correlation suggests that monazite solubility is dependent on P in the melt.

References

- [1] K. Klimm et al. (2008) *Journal of Petrology* **49**, 523-553
- [2] J.-M. Montel (1993) *Chemical Geology* **110**, 127-146
- [3] T. Plank et al. (2009) *Nature Geoscience* **2**, 611- 614
- [4] S. Skora and J.D. Blundy (2010) *Journal of Petrology* **51**, 2211-2243
- [5] T. Plank and C.H. Langmuir (1998) *Chemical Geology* **145**, 325-394
- [6] J. Hermann and D. Rubatto (2009) *Chemical Geology* **265**, 512-526

Long-lived Deep-Crustal Metamorphism in the Eastern Ghats Belt, India

M. Thomas and S.L. Harley

School of GeoSciences, University of Edinburgh, Edinburgh EH9 3JW, UK

Background

Recent geochronological studies on the Eastern Ghats (EGB) of India have proposed a series of high-T events in the time interval 1000-900 Ma. However, as these have not been precisely linked to the structural and metamorphic evolution it has not been possible, as yet, to define the P-T-time history and longevity of high-T conditions in the EGB, which is a prerequisite for evaluating its correlation with other parts of former Rodinia. Two parallel metamorphic-geochronological studies have therefore been developed to achieve this. A companion study to that reported here has demonstrated an age of 1000-980 Ma for UHT metamorphism (at 8-10 kbar, 1000°C) followed by cooling and decompression on a shallow dP/dT retrograde path prior to the emplacement of leucogranites (at 6.6 kbar and 850 C) in the central EGB (Domain II of Rickers et al., 2001). The purpose of the present study is to apply SIMS U-Pb and REE analysis of zircon crystallised in these leucogranites to define their age of emplacement, determine the timing of zircon crystallisation in relation to garnet-bearing mineral assemblages and textures, and thereby constrain the Neoproterozoic P-T-time history of the EGB. Zircons and garnets from a garnet-quartz-feldspar-rutile-ilmenite leucogranite have been analysed following characterisation of accessory mineral microtextures using back-scattered electron and cathodoluminescence imaging. Zircons (100-150 µm diameter) are sector, planar-sector and fir tree-zoned multifaceted grains of 'soccerball' type. These occur in clusters within garnet, quartz and K-feldspar and along grain boundaries between these phases. Lobate garnets form 400-800 µm diameter porphyroblasts (Grt1, Fig. 1) containing cores rich in inclusions of oriented sillimanite and rutile and are overgrown by necklaces of garnet (Grt2) in fine intergrowth with quartz (Fig. 1) in association with recrystallised plagioclase. The textural features indicate that most of the zircon grew prior to or with the outermost garnet rims (Grt2, Fig. 1) and the garnet + quartz intergrowths (Grt2, Fig. 1).

Results

Rare Earth Element (REE) and Ti contents of the zircons and REE in garnet were analysed using the Cameca IMS-4f instrument. The operating conditions used were a primary O⁻ ion beam of 5 nA with a spot size of 20µm, and all other protocols as described in Harley and Kelly (2007). The similarities between the HREE patterns of both the older and younger populations of zircons and garnet rims (i.e. Grt) suggests that the zircons grew relatively late compared with garnet, as detailed in the caption to Fig. 2. Ti contents of zircon lie in the range 20-31 ppm, corresponding to minimum Ti-in-zircon temperatures in the range 806-851°C and yielding an averaged minimum T of 844±18°C based on the calibration by Ferry and Watson (2007).

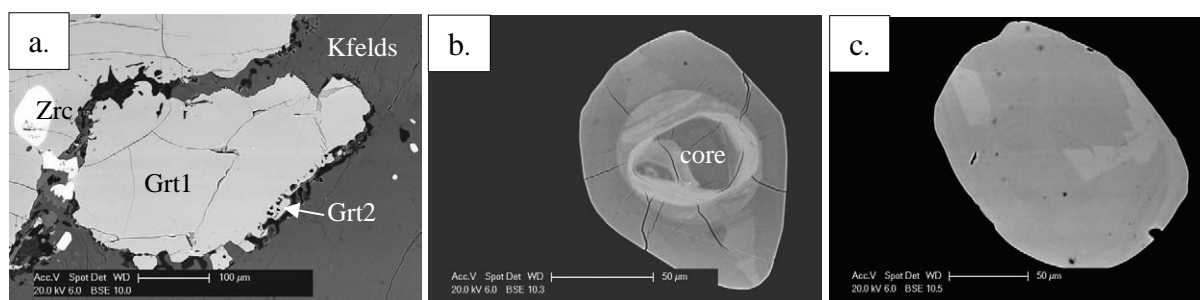


Fig. 1. BSE images of garnet (a) and zircons (b, c) in the EGB leucogranite. Notice the small relict zircon cores seen in b) and the weakly-developed fir tree zoning in c). The zircon shown in c) has a $^{206}\text{Pb}/^{207}\text{Pb}$ age of c. 922 Ma.

U-Pb age determination was carried out in situ on the Cameca 1270 ion probe. Analyses for HfO, ^{204}Pb , ^{206}Pb , ^{207}Pb , ^{208}Pb , Zr^{2}O_2 , ^{238}U , ^{232}ThO , ^{238}UO and $^{238}\text{UO}_2$ were repeated for 20 cycles, the first 5 of which were automatically excluded for isotopic calculations. Unknowns were referenced against the Plešovice standard (U < 465ppm; TIMS age of 337.13 ± 0.37 Ma; Sláma et al., 2008). Low to medium U contents (180-411 ppm) and moderate Th contents (193-277 ppm) in the EGB zircons gave Th/U ratios between 0.13 and 1.50. Of the 29 analyses obtained, 5 with high common Pb were excluded from further calculations. The remaining 24 analyses yield an average $^{207}\text{Pb}/^{206}\text{Pb}$ age of 908 ± 21 Ma.

An elevated MSWD (1.8) for this age indicates that the data involves at least two age populations (Fig. 3), consistent with the detailed microtextural settings of the analysed zircons. Twelve analyses form an older population (Fig. 3) with a $^{207}\text{Pb}/^{206}\text{Pb}$ age of 922 ± 14 Ma (MSWD 0.56). This is interpreted as the age of zircon crystallisation in the anatectic leucogranite. A younger age population at ~ 880 Ma (Fig. 3) is defined by zircons from a single textural domain on the recrystallised rim of a garnet (Grt2).

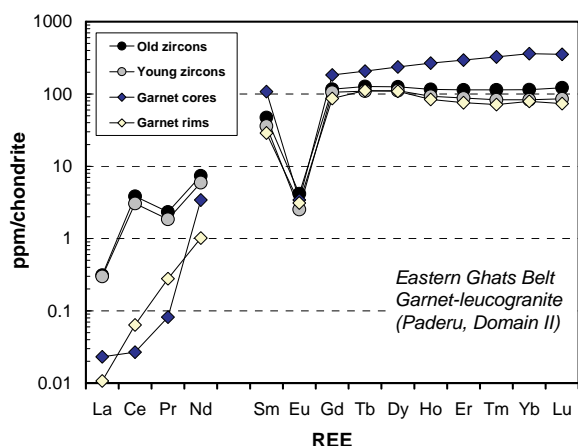
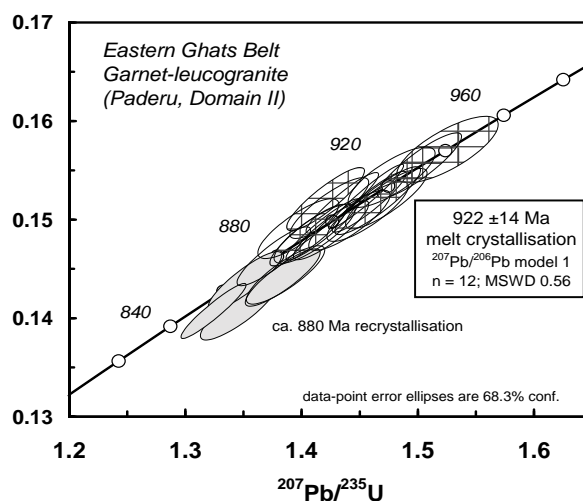


Fig. 3. U-Pb Concordia diagram showing zircon age data for the leucogranite. $^{207}\text{Pb}/^{206}\text{Pb}$ age is given at 2σ confidence level for the population of older, concordant zircon analyses (darker shaded ellipses). The younger group of zircon analyses (lighter shaded ellipse) are all derived from a biotite-bearing microtextural domain in which garnet is locally recrystallised along with plagioclase and quartz. These zircons have the lowest HREE contents (Fig. 2) and are inferred from comparison with recrystallised garnet HREE patterns to be c. 922 Ma anatectic zircons that have equilibrated with newly-grown garnet (Grt2) during an overprinting deformation at c. 880 Ma

Fig. 2. Rare Earth Element patterns for the younger (c. 880 Ma) and older (922 Ma) zircons compared with patterns for texturally early garnet cores (Grt1) and outer garnet rims or recrystallised necklaces (Grt2). Zircons are depleted in HREE compared with garnet cores, which are interpreted to pre-date zircon based on the D_{HREE} criteria of Harley et al. (2007). The 922 Ma (old) zircons are slightly HREE-enriched compared to the outermost garnet rim analyses, which approach HREE equilibrium with the younger (c. 880 Ma) zircons. Application of D_{HREE} criteria suggests that zircon crystallisation at 922 Ma involved substantial but incomplete equilibration with garnet rims during host-leucogranite interaction. Locally-controlled zircon recrystallisation at 880 Ma occurred simultaneously with garnet re-growth and recrystallisation.



Interpretation

Leucogranite in the central EGB crystallised under granulite facies conditions, prior to and at c. 922 Ma, at temperatures of $>844^\circ\text{C}$ and pressures of 6.8 kbar. REE disequilibrium between anatectic zircon and core garnet reflect the prior existence of garnet the assemblage Grt + Sill + Rutile + Qtz. The lack of chemical zoning in and absence of textural evidence for resorption of the early garnet is consistent with continuous high-T granulite conditions from c. 990 Ma, the age for UHT obtained in a companion study, to at least 922 Ma. An episode of new garnet growth at ~ 880 Ma is part of the same overall high-grade evolution. The implied long time span at $T > 800^\circ\text{C}$ (>100 Ma) is consistent with metamorphism in a hot, large-scale accretion-to-collision orogen. The combination of age data provides very strong evidence for correlation of the EGB with the Rayner Complex of Antarctica, where comparable high-T metamorphism occurred from 990-970 Ma (M1) to 940-920 Ma (M2), terminated by later shear-zone controlled deformation at 900-860 Ma.

References

- J.M. Ferry and E.B. Watson (2007) Contributions to Mineralogy and Petrology **154**, 429-437
 S.L. Harley and N.M. Kelly (2007) Chemical Geology **241**, 62-87
 K. Rickers et al. (2001) Precambrian Research **112**, 183-210
 J. Sláma et al. (2008) Chemical Geology **249**, 1-35

Major, trace and volatile chemistry of the March to May 2010 basaltic flank and benmorite summit eruptions at Eyjafjöll volcano, Iceland

T. Thordarson, M.E. Hartley, C. Hayward & J.G. Fitton

School of GeoSciences, University of Edinburgh, Edinburgh EH9 3JW, UK

Background

The 14th April–22 May eruption at Eyjafjallajökull volcano (Iceland) caused significant social and economic disruption in the UK and Europe, because of its ash-rich nature and the state of atmospheric flow. This explosive benmorite summit eruption, together with its predecessor, the 20 March to 12 April alkali (FeTi) basalt flank eruption at Fimmvörðuháls, has provided an opportunity to study and quantify a set of interlinked magmatic and volcanic processes extending from the source to place of deposition of the erupted magma [1,2]. Researchers at the University of Edinburgh, together with colleagues in Iceland, France, Italy, Norway and United Kingdom, have formed an informal multidisciplinary collaborative research alliance. This alliance is engaged in a multifaceted study integrating volcanological, petrochemical, and geophysical aspects of these eruptions. This research is partly funded by the NERC Emergency Grant NE/I00775X/1.

Objectives

The objectives of this one day scoping investigation were to assess the value of the following hypotheses:

- A. The basalt magma produced by the 20 March–12 April Fimmvörðuháls flank event is high density magma that erupted because it was rich in volatiles and thus originated from an enriched source.
- B. Eruption of very fluid basaltic magma via lava fountains and the subsequent formation of highly viscous a'ala lava resulted from very efficient (>70%) degassing of the magma upon venting.
- C. The benmorite magma from the current eruption is enriched in H₂O and its explosivity was principally driven by exsolution of magmatic water.

Results

The data and the results presented here are preliminary because the ionprobe measurement have yet to be synthesised and calibrated robustly with major element concentration obtained on the same groundmass glass and melt inclusions by the electron microprobe. In addition, the samples measured from the summit eruption only cover the first 5 days of activity (i.e. the initial phase of the event) and thus may not be representative for later eruption stages. However, despite these caveats the ionprobe results provide valuable insights into magmatic processes driving the 2010 eruptions at Eyjafjallajökull volcano and allow first order assessment of the hypotheses listed above. In regards to major elements the Cameca 4f SIMS measurements are generally consistent with groundmass glass and melt inclusion data measured on the EMMAC Cameca SX100 electron microprobe (Fig. 1a). Moreover, the composition of the plagioclase-hosted basaltic melt inclusions from the summit eruption tephra are almost identical to that obtained for melt inclusions and groundmass glass in the Fimmvörðuháls flank eruption and hence suggestive of common origin (Figs 1a-c). This implies that these summit eruption plagioclase phenocrysts crystallized from a mafic melt similar to that erupted by the flank eruption and subsequently incorporated into the benmorite magma erupted at by the summit vents. These results are consistent with the evidence that the summit eruption was driven by injection of basaltic magma similar to that erupted by the flank eruption and subsequent mixing with a more light rare earth enriched silicic magma body residing in the shallower parts of the volcano plumbing system [1]. This notion is further corroborated by elevated light to heavy rare earth element ratios ($La/Y_N=13.8-15.2$) and definite grouping of the benmorite compositions compared to the mafic ones ($La/Y_N=10.7-12.5$; Fig. 1b). Strong negative Sr and Ti anomalies in the multi-element pattern of the benmorite glass suggest that the mixing of the two magmas promoted crystallization (and fractionation) of plagioclase and titanomagnetite (Fig. 1c, middle panel).

The H₂O content in plagioclase-hosted melt inclusions from the basaltic Fimmvörðuháls tephra spans the range of 0.20–0.88 wt%, whereas the groundmass cluster tightly between 0.05 – 0.11 wt% H₂O (Fig. 1d). Taking the highest measured inclusion values (0.85–0.88 wt% H₂O) to represent the initial (pre-eruption) water content of the Fimmvörðuháls magma, then the lower inclusions values can be interpreted trapping of melt parcels recording progressive degassing as the magma passed through the shallowest part of the conduit. Also, the estimated total volatile content of 1.5 ± 0.08 wt%, of which 0.87 ± 0.01 wt% is H₂O and 0.29 ± 0.02 wt% is CO₂, which indicates that the Fimmvörðuháls magma originated at a volatile-rich source and thus supporting hypothesis A above. The data implies that 87-95% of the original volatile

cargo was vented into the atmosphere up on eruption, suggesting that the observed lava fountaining and a'a lava formation was driven by degassing rather than discharge (ca. 13 m³/sec on average) and thus providing favourable support for hypotheses B above. Volatile analyses on the summit benmorite tephra show the water content in the basaltic melt inclusions (0.79–2.12 wt% H₂O) is compatible or higher than in the one measured benmorite melt inclusion (1.69 wt% H₂O; Fig. 1d). The corresponding benmorite groundmass glass contains 0.36–0.82 wt% H₂O (average, 0.58±0.17 wt% H₂O). Although further analyses are required, these data indicate that the benmorite magma erupted by the summit eruption was not particularly enriched in water and raises concerns about our last hypothesis (C). But more interestingly, it appears to indicate that the basaltic end-member involved in the magma mixing is the principal source of the volatiles. If this is correct, then the initial volatile content of the basaltic magma and subsequent evolution during ascent as well as mechanisms of volatile exchange during mixing will play an important role in determining the nature of the ensuing eruption.

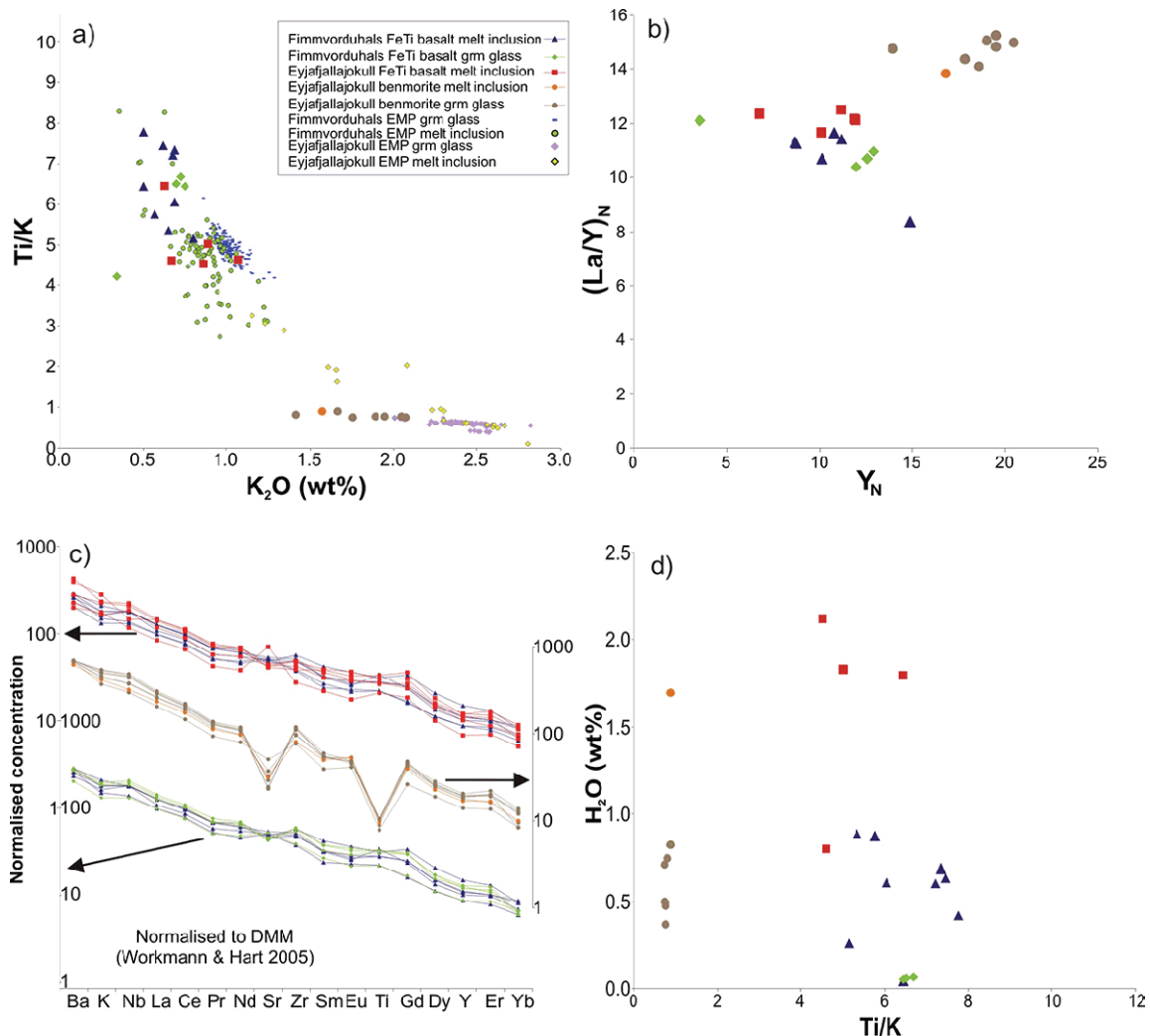


Fig. 1 Major, trace and volatile element concentrations, ratios and patterns in groundmass glass (grm) and plagioclase-hosted melt inclusions as measured by the ion probe in tephra samples from the 20 March to 12 April 2010 Fimmvörðuháls mildly alkalic (FeTi) basalt flank and 14 April to 22 May 2010 benmorite summit eruptions at Eyjafjallajökull volcano (Iceland). See key for further details. (a) TiO₂/K₂O versus K₂O (wt%). The compositional fields of groundmass glass and melt inclusions as determined by electron microprobe (EMP) in samples from both eruptions is shown for comparison. (b) Rare earth element fractionation as illustrated by (La/Y)_N versus Y_N (ppm). (c) Normalized multi-element diagram showing fractionation patterns for (i) basalt groundmass glass and melt inclusions from Fimmvörðuháls flank eruption (lowest panel), (ii) benmorite groundmass glass and melt inclusion from the summit eruption (middle panel), and (iii) plagioclase-hosted basalt melt inclusions from the summit and Fimmvörðuháls events (top panel). Trace element concentrations are normalized to depleted mantle (DMM) values [3]. (d) Water concentrations versus Ti/K in melt inclusions and groundmass glass from both eruptions.

References

- [1] Guðmundsson et al. (2010) AGU Fall Meeting, abstract V53F-01 [2] Sigmarsson et al. (2011) Dynamic magma mixing triggering the 2010 Eyjafjallajökull eruption, submitted to *Geology*. [3] R.K. Workman and S.R. Hart (2005) *Earth and Planetary Science Letters* **231**, 53-72.

Oxygen isotope variation in Icelandic basalts: disentangling mantle and crustal signatures.

B. Winpenny & J. Maclennan

Department of Earth Sciences, University of Cambridge, Downing Street, Cambridge, CB2 3EQ, UK

Introduction

Under mid-ocean ridges, incremental melting of the mantle produces melts with a range of major and trace element compositions. These melts may rise in channels and only fully mix with each other once they reach the lower oceanic crust. The onset of mantle melting under ridges may be associated with the melting of fusible heterogeneities (possibly recycled, subducted crust or sediments). These heterogeneities play a role in controlling trends in isotopic variability (e.g. $^{87}\text{Sr}/^{86}\text{Sr}$, $^{143}\text{Nd}/^{144}\text{Nd}$) observed in Icelandic basalts. However, the cause of the low $\delta^{18}\text{O}$ signature in high-MgO Icelandic basalts (whole rock $\delta^{18}\text{O}$ down to $\sim 3.5\%$, compared to 5.21 to 5.81‰ for mid-ocean ridge basalts) and their crystals has been disputed. Some argue that the signature is a result of hydrothermal processes in the Icelandic crust [1], while others favour a mantle source from recycled material [2]. Establishing the cause of the low $\delta^{18}\text{O}$ values has general implications for both mantle geochemistry and the depth and extent of hydrothermal systems in oceanic crust. We aimed to investigate $\delta^{18}\text{O}$ variation in two Icelandic basalt flows, resolving the ambiguities of previous studies by making fine-scale intra-crystal analyses in crystals hosted by each flow.

Approach

The compositional heterogeneity of mantle melts entering the Icelandic lower crust has previously been observed from trace element analyses of olivine-hosted melt inclusions in the ~ 8 kyr old Borgarhraun flow, north Iceland [2]. Compositional heterogeneity of the mantle melts is destroyed by melt mixing during crystallisation, so early-crystallised products must be investigated when looking for clear mantle signatures. We therefore concentrated on high anorthite (70-90 mol% An) plagioclase and high-Mg# (80-92) clinopyroxene crystals. These exist within polycrystalline nodules from the Borgarhraun flow and the September 1984 flow of the Krafla fissure eruptions. Major element zonation in the crystals was firstly characterised by backscattered electron images and electron microprobe profiles.

The objectives of the ion microprobe analyses were to: **1)** measure concentrations of selected trace elements in the compositional zones of clinopyroxene and plagioclase, using the Cameca IMS-4f; **2)** analyse the same zones in plagioclase for high-precision (0.3‰, 1σ) $^{18}\text{O}/^{16}\text{O}$ ratios on the Cameca 1270. Oxygen isotope ratios in plagioclase crystals were initially measured in late 2009, but repeated in September-October 2010 in order to improve the signal to noise ratio of the measurements and their accuracy.

The coincident nature of trace element and oxygen isotope data points was planned in order provide a full record of compositional variation in melts in equilibrium with the crystals. With this record, trace element and isotopic systematics allow the distinction of a hydrothermal origin for the low $\delta^{18}\text{O}$ signature from a mantle origin. For instance, melts formed in the presence of garnet ($> \sim 80$ km depth in the mantle) should have high La/Yb, Sr/Y and La/Y. Mantle heterogeneities are thought to be fusible, melting in the garnet-field, and so a low $\delta^{18}\text{O}$ signature arising from these heterogeneities should correlate with increasing La/Yb, Sr/Y or La/Y of the melt. An origin for the signature by melting of hydrothermally altered Icelandic crust would instead be recognised by $\delta^{18}\text{O}$ decreasing with constant or decreasing Sr/Y of the melt.

Results

From the trace element analyses (performed in April 2009), variability in key trace element ratios, such as La/Yb, was found to be present within and between the plagioclase and clinopyroxene crystals. The variability in these ratios requires a range of melt compositions during crystallisation. For both plagioclase and clinopyroxene, we carried out further investigation of trace element systematics, with reference to crystal textures and major element variation within the crystals. For the Borgarhraun samples, this investigation showed that the variation in trace element ratios in the crystals (e.g. La/Yb, La/Y and Sr/Y) chiefly arose from corresponding variation in these ratios within primary mantle melts. On the other hand, many crystals from the Krafla flow were crystallised from melts which had

been affected by assimilation of crustal material. Unlike Borgarhraun, the record of mantle melt heterogeneity in the Krafla crystals has thus been largely destroyed by late, crustal processes.

The new dataset of O isotope ratios shows variability in $\delta^{18}\text{O}$ between many of the plagioclase zones. Of particular note, An_{84-90} plagioclase from the Borgarhraun flow display a 1.4‰ range in $\delta^{18}\text{O}$ at high An content (Fig. 1). Since $\delta^{18}\text{O}$ and trace element analyses were made on the same scale (in individual plagioclase compositional zones), it was possible to investigate correlations between these geochemical indices without the ambiguities which have previously arisen when comparisons have been made between datasets analysed at different scales (whole rock, crystal separates) [1,2].

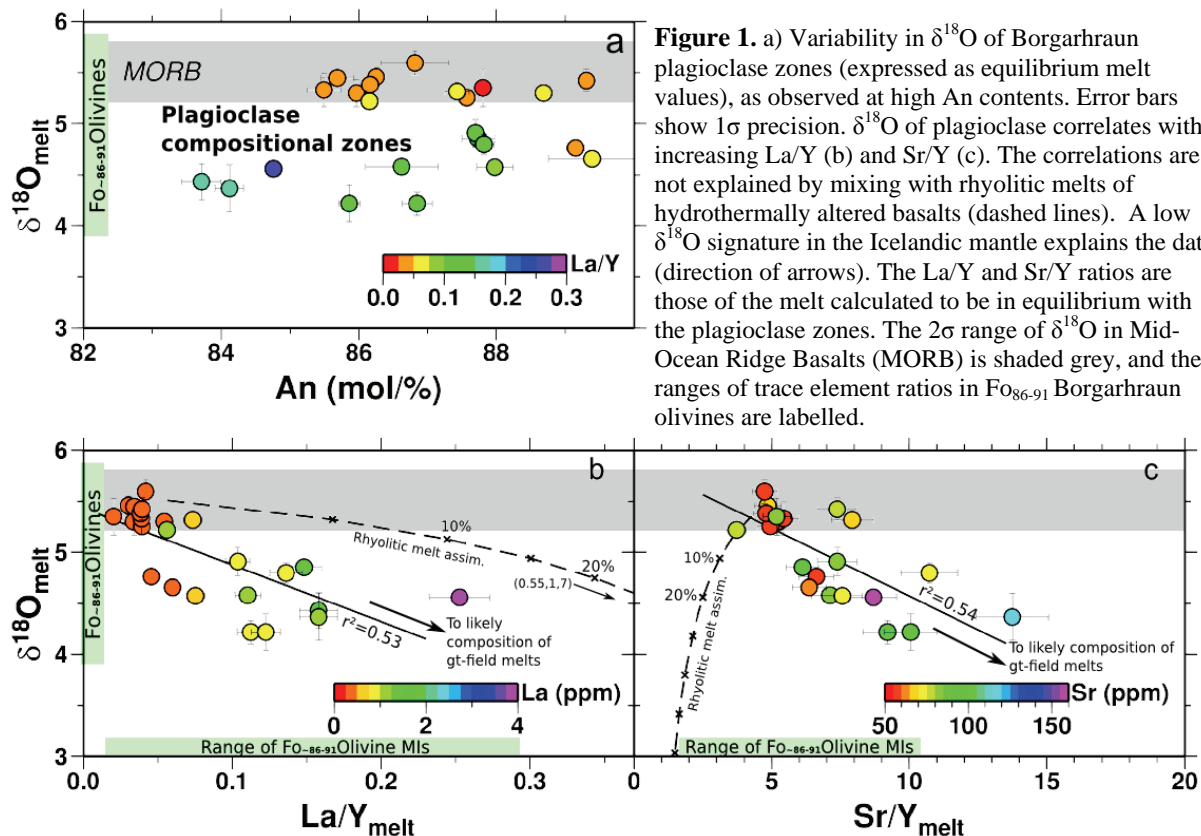


Figure 1. a) Variability in $\delta^{18}\text{O}$ of Borgarhraun plagioclase zones (expressed as equilibrium melt values), as observed at high An contents. Error bars show 1σ precision. $\delta^{18}\text{O}$ of plagioclase correlates with increasing La/Y (b) and Sr/Y (c). The correlations are not explained by mixing with rhyolitic melts of hydrothermally altered basalts (dashed lines). A low $\delta^{18}\text{O}$ signature in the Icelandic mantle explains the data (direction of arrows). The La/Y and Sr/Y ratios are those of the melt calculated to be in equilibrium with the plagioclase zones. The 2σ range of $\delta^{18}\text{O}$ in Mid-Ocean Ridge Basalts (MORB) is shaded grey, and the ranges of trace element ratios in Fo_{86-91} Borgarhraun olivines are labelled.

Crucially, we observe correlations between decreasing $\delta^{18}\text{O}$ and increasing Sr/Y and La/Y in the Borgarhraun plagioclase zones. These correlations are shown in Figure 1, where trace element ratios are expressed as ratios of the melt in equilibrium with the crystal zone (calculated using crystal-melt partition coefficients). Since both Sr/Y and La/Y increase with decreasing $\delta^{18}\text{O}$, the correlations point clearly to a mantle origin for the low $\delta^{18}\text{O}$ signature in these high An plagioclase crystals.

Conclusions

The set of plagioclase and clinopyroxene crystals from the Borgarhraun flow, N. Iceland, preserves a record of the compositionally variable mantle melts entering the Icelandic crust. Correlations of decreasing $\delta^{18}\text{O}$ with increasing Sr/Y and La/Y in Borgarhraun plagioclase zones indicate that the low $\delta^{18}\text{O}$ signature in some high-MgO Icelandic lavas reflects mantle oxygen isotope heterogeneity, rather than the hydrothermal processes in the Icelandic crust. The low $\delta^{18}\text{O}$ signature (down to a melt equivalent value of 4.2‰) in the Icelandic mantle source is associated with melting in the garnet stability field, and likely represents recycled ancient crustal material in the mantle. While this result has been suspected previously, the fine scale measurements in this work have overcome the ambiguities of earlier datasets, which made analyses on a range of scales. While the low $\delta^{18}\text{O}$ signature in Borgarhraun stems from the Icelandic mantle source, hydrothermal processes still play a key role in controlling the oxygen isotope composition of other basalts, including the Krafla flow, for which plagioclase $\delta^{18}\text{O}$ averages $\sim 4\text{‰}$ (melt equivalent).

References

- [1] J. M. Eiler et al. (2000), Earth and Planetary Science Letters **184**, 269-286
- [2] J. Maclennan et al. (2003) Geochemistry Geophysics Geosystems **4** DOI:10.1029/2003GC000558